2018

Two-Way Feedback between Air-Sea Turbulent Fluxes and Oceanic Submesoscale Processes

Xu Chen

FLORIDA STATE UNIVERSITY

COLLEGE OF ARTS AND SCIENCES

TWO-WAY FEEDBACK BETWEEN AIR-SEA TURBULENT FLUXES AND OCEANIC SUBMESOSCALE PROCESSES

By

XU CHEN

A Dissertation submitted to the
Department of Earth, Ocean, and Atmospheric Science
in partial fulfillment of the
requirements for the degree of
Doctor of Philosophy

2018

Xu Chen defended this dissertation on November 7, 2018.
The members of the supervisory committee were:

William K. Dewar
Professor Co-Directing Dissertation

Eric Chassignet
Professor Co-Directing Dissertation

Christopher Tam
University Representative

Mark A. Bourassa
Committee Member

Steve Morey
Committee Member

The Graduate School has verified and approved the above-named committee members, and certifies that the dissertation has been approved in accordance with university requirements.

ACKNOWLEDGMENTS

I am grateful to everyone who supported me during this journey of pursuing knowledge.

My first expression of gratitude goes to my advisor Dr. William Dewar. His patience, encouragements, humor, modesty, and professional advices made my research progress smoothly in a cheerful environment. I would like to thank my co-advisor Dr. Eric Chassignet for encouraging me to present my work and providing me helpful feedback and guidance. I give my special appreciation to my committee members Dr. Mark Bourassa and Dr. Steve Morey for always being a constant source of inspiration. I am grateful to Dr. Christopher Tam for teaching me fluid dynamics and serving as university representative in my committee. I would like to thank Dr. Quentin Jamet, Dr. Nicolas Wiendes and Dr. Panagiotis Velissariou for helping me with running ocean models.

I owe a great deal of gratitude and appreciation to Tracy Ippolito, Tom Kelly, and Sean Buchanan for reviewing my dissertation.

I would like to thank my academic coordinator and beloved friend Michaela Lupiani for her love, support, and help through the journey of graduate school.

I am grateful for my dear friends who have brightened my life. You are like angles to me, giving me the real joy of friendship and keeping me away from loneliness and darkness.

I would like to thank my younger brother Zihong Chen for growing up with me.

To my mom and dad: Thank you for loving and supporting me no matter what happens.

Last but not least, to my dearest Shuying Yang. Thank you for being my wife, supporting me, loving me, and building our own family with me. Although there are many unknown chapters waiting for us in the future, I am sure that we will fill them with love and joy.

TABLE OF CONTENTS

LIST OF FIGURES

ABSTRACT

An accurate representation of air-sea interaction is crucial to the accurate numerical prediction of ocean, weather, and climate. It is known that sea surface temperature (SST) gradients and surface currents in the oceanic mesoscale regime significantly affect air-sea fluxes of momentum and heat, and the mesoscale-modified air-sea fluxes also influence the ocean dynamics on various scales. Previous studies found that resolving the mutual feedbacks between mesoscale processes and the atmosphere improved the accuracy of modeling for ocean, weather, and climate. In the submesoscale regime recently revealed by high-resolution numerical models and observations, the SST gradient and surface currents are found to be much stronger than those in the mesoscale. However, the mutual feedbacks between the submesoscale processes and the atmosphere are not well understood. To quantitatively assess the mutual responses between the air-sea fluxes and the submesoscale processes, a non-hydrostatic ocean model coupled with an atmospheric boundary layer module is implemented making it possible to examine the air-sea interactions over the submesoscale regime. The inclusion of surface currents in air-sea bulk flux parameterization and the atmospheric thermodynamic adjustments to the ocean surface are argued to be significant for modeling accurate wind stress and air-sea turbulent heat fluxes in the submesoscale regime. The results show that the linear relationship between wind stress curl/divergence and crosswind/downwind SST gradient, revealed in the mesoscale regime, do not exist in the submesoscale regime. Additionally, the magnitudes of positive and negative wind stress curl introduced by submesoscale processes are much greater than the magnitude of wind stress curl introduced by mesoscale processes. This study also finds that the evolution of submesoscale processes is closely associated with the potential vorticity (PV) budget. Because different fields of wind stress and turbulent heat fluxes are introduced by the influence of submesoscale surface velocity field and/or temperature field, these wind stress and heat flux fields can interact with submesoscale surface structures and provide different PV injections into the ocean. Therefore, the evolution of submesoscale processes is significantly influenced by the submesoscale-modified air-sea fluxes. This study serves as a starting point in the investigation of the two-way feedback between the atmosphere and oceanic submesoscale processes. It shows that numerically resolving the two-way air-sea coupling in the submesoscale regime significantly changes air-sea flux and the oceanic submesoscale dynamics

CHAPTER 1

INTRODUCTION

Wind stress and sea surface heat fluxes are essential components of air-sea momentum and heat exchanges in atmosphere-ocean communication. The momentum flux at the air-sea interface (wind stress) plays an important role in driving oceanic circulations on various spatial and temporal scales. On global scales, the general ocean circulation is mechanically driven by wind stress and tidal dissipation (Huang, 2010), while ocean currents balance the mass between convergence and divergence of Ekman transport attributed to the non-uniform global distribution of wind stress (Gill, 1982). On the basin scale, Sverdrup transport is significantly sensitive to wind forcing (Townsend et al., 2000), and Atlantic Meridional Overturning Circulation (AMOC) is closely related to the basin-scale wind stress and turbulent heat fluxes (Elipot et al., 2017; Kanzow et al., 2010; Wu et al., 2017).

An accurate and precise representation of wind stress and turbulent heat fluxes in numerical models is necessary to quantify the air-sea exchanges, to better represent the physics in the Marine Atmospheric Boundary Layer (MABL), and to improve forecasts of ocean, weather and climate (Bourassa et al., 2013; Rogers, 1995). However, in numerical models of previous studies, biases in air-sea fluxes causing significant errors in large-scale forecasts have been recognized (Bourassa et al., 2013; Lee et al., 2013; Moore & Renfrew, 2002; Roberts et al., 2012; Zhang et al., 2016). Several missing mechanisms have been considered for the biasing in wind-stress representation of numerical models. The lack of ocean surface currents in the wind stress algorithm is one such problem. The surface current, neglected because it is typically much weaker than the surface wind (Wu, 1975), has been found to have a significant impact on the surface fields of wind stress and turbulent heat fluxes. Satellite observations of wind stress have found a significant dependence on surface current (Chelton et al., 2004). In the broad perspective of energetics, an overestimate by more than a twenty five per cent has been found in net wind power input to the general ocean circulation (Duhaut & Straub, 2006; Scott & Arbic, 2007) when the influence of surface currents on wind stress was ignored. In the regional model studies (Dawe & Thompson, 2006; Zhai & Greatbatch, 2007), reductions of total wind work over Northwest Atlantic Ocean and North Pacific are about 17% and 27%, respectively, when the effect of ocean surface current is considered in the wind stress representation. Not only is this true for the large-

scale circulations, mesoscale eddies and ageostrophic motions are also damped significantly by including the surface current in calculation of air-sea turbulent fluxes (Wu et al., 2017).

Wind stress modification due to coupling between sea surface temperature (SST) and the atmosphere is another mechanism that is ignored in the uncoupled model. It is considered as an important cause for biasing of the wind stress in numerical studies. Previous works provided two hypotheses to explain the impact of SST coupling on wind stress: (I) surface wind acceleration/deceleration attributed to the surface atmospheric pressure gradient across an SST gradient (O'Neill et al., 2010; Small et al., 2008) and (II) wind stress modification due to the stabilization/destabilization of atmospheric boundary layer over cool/warm waters (Spall, 2007; Wallace et al., 1989). Despite that the two hypotheses are physically distinct from each other, they try to recover the mechanism behind the same phenomenon: wind stress over a warmer ocean is greater than the wind stress over a cooler ocean. This phenomenon is confirmed by the positive linear relationship between wind stress curl/divergence and crosswind/downwind SST gradient in satellite scatterometer data (Chelton, 2004). However, in western boundary current regimes where ocean surface current and current shear is enhanced, the effect of SST coupling on wind stress is secondary to the wind stress modification due to surface current. In the regime of a mesoscale eddy, wind stress curl introduced by SST gradients is also secondary with respect to current-induced wind stress curl (Gaube et al., 2015).

Biases of wind stress and heat flux at the air-sea interface are also related to the resolution of ocean models. Improvements of numerical techniques and computational resources enabled ocean models to reveal finer scale processes. Mesoscale processes in the ocean with horizontal length scales of 10-100 km have been studied extensively since originally observed by Swallow (1971). Prevalent in the ocean, mesoscale processes play a significant role in many oceanic processes, such as the oceanic energy cascade and decadal variability of Western boundary currents (Charney, 1971; Kang & Curchitser, 2015; Qiu & Chen, 2010). However, resolving mesoscale processes in a global or basin model has been computationally prohibitive until the last two decades. Comparing to coarser resolution ocean fields, mesoscale-resolving ocean models provide more accurate representation of variability and fronts. Combining these mesoscale oceanic structures with atmospheric boundary elements can provide a more accurate air-sea momentum and turbulent heat flux for models. A recent study of Parfitt et al. (2017) found that refining SST field resolution from $1^o \times 1^o$ to $0.05^o \times 0.05^o$ (mesoscale-resolved)

changed frontal air-sea sensible heat flux and modified the weather and climate significantly. Many other previous studies proved benefits of mesoscale-resolving models on predictions ranging from tropical cyclones, mean precipitation, and coastal upwelling processes (Jochum et al., 2005; Small et al., 2008; Walsh et al., 2015).

Previous research has shown the importance of coupling between the atmosphere and the oceanic mesoscale processes. For example, surface velocity and temperature fields of a mesoscale eddy locally modify the wind stress field; in turn, the modified wind stress field affects the evolution of the mesoscale eddy (Dewar & Flierl, 1987). There are two mechanisms that allow the wind stress field to respond to mesoscale eddy influences: (I) Surface current vorticity generates additional wind stress curl when the surface current is considered in the wind stress algorithm. (II) Extra wind stress curl is introduced when wind blows across an SST gradient. Ekman pumping, which drives many ocean dynamics including coastal upwelling, is closely related to the wind stress curl field; however, when Ekman pumping is introduced by an eddy-adjusted wind stress curl field, the strong surface current vorticity and its gradient can modify the magnitude of Ekman pumping according to non-linear Ekman theory (Gaube et al., 2015). Oerder et al. (2018) compared dynamic ocean responses to wind stress fields with and without consideration of surface current. The comparison showed that a current-modified wind stress field significantly reduced mesoscale activities in the ocean. The surface wind stress curl generated over crosswind SST gradients also provides an important term in the upper ocean vorticity budget, while the surface wind stress divergence can be an indicator of air-sea interaction in regions of strong SST gradients (Chelton et al., 2001). The mesoscale air-sea coupling mechanism and its impact on multi-scale oceanic and atmospheric dynamics are current areas of research (Kang & Curchitser, 2015; Ma et al., 2016; Renault et al., 2017).

Differing from quasi-geostrophic mesoscale (10-100 km) and small dissipation-scale (0.1 - 100 m) processes, submesoscale processes feature an intermediate lateral length scale between 100 m and 10 km. Full appreciation of the abundance of submesoscale phenomena has come only in recent years because of the intermediate length scale, which is either too large for detection by typical shipboard instruments or too small for detection by satellites (McWilliams, 2016). In recent years, resolution improvements in both direct observations and in numerical modeling have revealed a richness of submesoscale processes in the upper ocean.

Length scales ranging between 100 km and 100m have been referred to as submesoscale in previous studies; this shows the ambiguity in defining submesoscale according to spatial extent. On the other hand, the widely accepted definition referring to dynamical numbers, such as Rossby number (Ro) and Richardson number (Ri), can provide explicit dynamical criteria for submesoscale processes (McWilliams, 2016; Thomas et al., 2007). In this study, O(1) Ro and Ri, and a length scale of 100 m -10 km are used as criteria for defining the submesoscale processes in the model results.

Many studies have sought to quantify the roles played by the submesoscale in the vertical fluxes of tracers and energy cascade. While mesoscale processes governed by quasi-geostrophic dynamics are characterized by a inverse energy cascade (Charney, 1971; Scott & Arbic, 2007), submesoscale processes begin to break down the geostrophic balance and lead to secondary ageostrophic circulation, which provide an alternative dissipation route (Capet et al., 2008; D'Asaro et al., 2011; McWilliams, 2003; McWilliams, 2016; McWilliams et al., 2001). Strong vertical velocities have also been associated with submesoscale structures characterized by enhanced vorticity and rates of strain (Thomas et al., 2007). The submesoscale velocity is usually 1 - 2 orders greater than the typical vertical velocity within the mesoscale regime (10^{-4} - 10^{-5} ms^{-1}). Previous studies revealed that the strong submesoscale vertical velocity can redistribute a significant amount of buoyancy and restratify the upper ocean (Boccaletti et al., 2007; Capet et al., 2008; Fox-Kemper et al., 2008; McWilliams, 2016; Thomas et al., 2007). The transport of tracers, such as nutrients and plankton, by vertical pumping in the submesoscale regime can also impact phytoplankton production and biogeochemical cycling (Klein & Lapeyre, 2009; Lévy et al., 2012; Mahadevan, 2016). Therefore, researchers have investigated the role of submesoscale processes in both physical dynamics and in ecosystem evolution within the upper ocean.

Potential vorticity flux at the surface and throughout the mixed layer is an important tracer for connecting the surface, mixed layer and the deep ocean (Marshall & Nurser, 1992). In submesoscale regimes, enhanced PV transport is associated with strong vertical pumping in the mixed layer, and the PV flux at the air-sea interface has been investigated by previous works (Thomas & Ferrari, 2008; Thomas et al., 2007; Wenegrat et al., 2018) to show the association between the upper layer PV budget and air-sea interactions. As additional studies on the roles of the submesoscale in ocean dynamics have been made, submesoscale effects on the air-sea interaction have slowly come into focus.

Although the feedbacks between surface wind stress and mesoscale processes have been extensively investigated, little is known about the feedback between the submesoscale processes and surface wind stress. Previous mesoscale studies concluded that the consideration of SST gradients and surface currents in the wind stress parameterization have improved the modeling of MABL. Submesoscale processes play an important role in upper ocean dynamics, and large magnitudes of surface vorticity and SST gradient within the submesoscale regime are much greater than those of the mesoscale (Capet et al., 2008; Chelton, 2004; Fox-Kemper et al., 2008; McWilliams, 2016; Stamper & Taylor, 2017; Thomas & Ferrari, 2008; Thomas et al., 2007). To investigate the two-way interactions between wind stress and submesoscale features with strong SST gradients and enhanced surface vorticity, this research was conducted to examine (1) how wind stress responds to the sea surface structures (i.e. strong SST gradients and enhanced current vorticity field) of submesoscale processes, and (2) what is the influence of submesoscale-modified wind stress on the evolution of submesoscale processes in the mixed layer.

Questions related to the first issue are:

1) Is the linear relationship between wind stress curl/divergence and crosswind/downwind SST gradient at the mesoscale (Chelton et al., 2004) still valid in the submesoscale regime? If it is not valid, what is the reason for it?

2) What is the effect of the magnitude and direction of wind forcing on the coupling (quantified by a coupling coefficient) between wind stress curl/divergence and crosswind/downwind SST gradient?

3) In the submesoscale regime, how do the surface current coupling and the thermodynamic coupling affect domain-averaged wind stress and heat fluxes?

Throughout this dissertation, the surface current coupling refers to the inclusion of the ocean surface current in the air-sea turbulent flux bulk algorithm, and the thermodynamic coupling is used to refer to the temperature and humidity adjustments between the atmosphere and the ocean surface while the wind field is prescribed.

In terms of the second issue, this work seeks to address the following questions:

1) How do the submesoscale processes evolve under different wind forces?

2) When forced by the same wind, do the surface current coupling and the thermodynamic coupling cause the submesoscale processes to evolve differently?

To simulate oceanic submesoscale processes and their interactions with the atmosphere, this study implements a high-resolution non-hydrostatic ocean model coupled with an atmospheric boundary layer model, in which the ocean surface state appears in the algorithms for air-sea turbulent fluxes and their effects can be switched on and off. The wind field in the atmospheric boundary layer is prescribed to avoid the complications of atmospheric dynamics. While ignoring wind adjustment to SST does limit investigation of wind modification of SST (O'Neill et al., 2010; Small et al., 2008), it enables direct quantification of the wind stress change due purely to the SST-affected atmospheric boundary stratification (Spall, 2007; Wallace et al., 1989).

Information on the model system, detailed description of submesoscale generation and the design of submesoscale-atmosphere experiments are included in the following chapter. General description for the numerical experiment and results are shown in Chapter 3. The fourth chapter presents the finding on wind stress adjustments to submesoscale processes. It includes analyzing the wind stress curl and divergence introduced by SST gradients and surface current vorticity over different submesoscale structures, examining the effect of wind speed magnitude on coupling coefficients, and discussing the turbulent heat flux modification due to the surface current coupling and the thermodynamic coupling in air-sea flux algorithm. Chapter 5 investigates the impact of submesoscale-modified air-sea turbulent fluxes on the evolution of submesoscale processes in the ocean. First, the linking between the evolution of submesoscale processes and PV budget is investigated. Then, the PV fluxes at the ocean surface influenced by different submesoscale-modified air-sea turbulent fluxes are quantitatively assessed. Conclusions are briefly summarized in the final chapter.

CHAPTER 2

METHODS

2.1 Model Description

2.1.1 MITgcm

The Massachusetts Institute of Technology general circulation model (MITgcm) is used to numerically simulate the submesoscale processes and phenomena in this study. Equipped with both hydrostatic and non-hydrostatic configurations, MITgcm is able to simulate phenomena ranging from micro- to planetary scales (Marshall et al., 1997). The non-hydrostatic module is implemented in this study to capture the near surface strong vertical accelerations. Many previous modeling studies have implemented MITgcm to simulate submesoscale processes in the ocean (Bachman et al., 2017; Brannigan et al., 2015, 2017; Hamlington et al., 2014; Rosso et al., 2015).

2.1.2 CheapAML

The Cheap Atmospheric Mixed Layer (CheapAML) model is used to simulate the evolution of atmospheric layer temperature and humidity, as well as momentum and heat exchanges between the atmosphere and ocean (Deremble et al., 2013). Developed based on (Seager et al., 1995), CheapAML incorporates modern flux algorithms such as the COARE3 algorithm (Fairall et al., 2003), which are used in this study. Although the COARE3 algorithm has been used to diagnose turbulent fluxes between atmosphere and ocean (Brunke et al., 2003; Yu, 2007), only recently has it been applied to coupled models (Deremble et al., 2013). In most of the current air-sea coupled systems, the horizontal spatial resolution of atmosphere models are coarser than those of ocean models, which attenuates the atmospheric feedbacks to the ocean surface (Parfitt et al., 2016, 2017). In this work, both the ocean model and the atmospheric mixed layer model have the same horizontal resolution in order to capture atmospheric responses to ocean properties accurately. This approach can also provide a method for evaluating the error of air-sea fluxes introduced by coarse atmospheric resolution.

Because CheapAML is built upon the assumption that atmospheric velocity is the least sensitive to ocean surface structure, wind in the atmospheric mixed layer is prescribed in the

model. Although the complexity of atmospheric dynamics is avoided, the wind modifications due to ocean surface processes as discussed by Small et al. (2008) are ignored. Thus, the coupling of MITgcm and CheapAML in this study merely means that they are thermodynamically coupled, not dynamically coupled. In observation, wind stress over warm water tend to be stronger than the one over cool water. Wallace et al. (1989) and Spall (2007) argued that wind stress can adjust to SST, because SST can modify the near surface atmospheric pressure gradient to impact the efficiency of downward transport of momentum. However, Small et al. (2005) and O'Neill et al. (2010) argued that SST gradient can change the atmospheric pressure to influence the surface wind speed, thus impact the wind stress. Neither of these machanisms are well represented in CheapAML.

Because ocean surface currents are usually much smaller than surface winds, the inclusion of ocean currents in wind stress calculations was not addressed until the 1990s (Kelly et al., 2001; Park et al., 2006; Wu, 1975). Many subsequent studies have revealed that strong surface currents and current shear could exist in the submesoscale regime (McWilliams, 2016; Stamper & Taylor, 2017; Thomas & Lee, 2005). Switching the current effect on and off in the CheapAML turbulent fluxes enables the examination of the ocean surface current influences on air-sea exchange fluxes and the evolution of submesoscale processes.

2.2 Experimental Design

The first goal of the numerical experiments in this study is to simulate submesoscale processes in the ocean. To achieve this goal, submesoscale symmetric instability, baroclinic instability, and mixed modes will be generated. MITgcm is used to generate these submesoscale oceanic processes. The experiment for submesoscale generation is called a preliminary run in this study.

In the second stage of this study, CheapAML is coupled with MITgcm to introduce air-sea interactions to the evolution of submesoscale processes. Air-sea momentum and heat fluxes are calculated using four different schemes to evaluate the influences of air-sea thermodynamic coupling and ocean surface currents on air-sea fluxes. A wide range of wind speeds is also examined to investigate the sensitivity of air-sea fluxes to wind speed magnitude and direction. For simplicity, both longwave radiation and shortwave radiation are switched off in these experiments. The oceanic submesoscale evolution due to variant air-sea fluxes, which are

calculated from different air-sea schemes and prescribed wind speeds and directions, are also studied. Specific details on configurations for both the first and second stage experiments are provided in sections 2.2.1 and 2.2.2.

2.2.1 Preliminary Run

In order to numerically generate submesoscale processes, a high-resolution preliminary simulation is run to allow symmetric instabilities, a transition to baroclinic instabilities, and submesoscale eddies to take place. The horizontal and vertical dimensions are a length and width of 5 km and a depth of 100 m. Fifty vertical layers and 500 south-north and east-west horizontal grids provide a uniform vertical resolution of 2 m and horizontal resolution of 10 m, respectively. Isotropic viscosity of 1 x 10^{-3} m^2s^{-1} and thermal diffusivity of 1 x 10^{-3} m^2s^{-1} are used for the preliminary run. Based on Stamper and Taylor (2017), these small viscosity and diffusivity values are selected to allow for possible small-scale processes to take place. Lateral boundaries on north and south edges are closed and free-slip, while periodic boundaries are set for the west and east edges to make the domain a periodic channel. The initial fields of velocity and temperature for the preliminary run are shown in Fig. 2.1. The initial meridional component of velocity, v, is set to zero over the domain, while the zonal component of velocity, u, is initially geostrophically balanced with a pressure field as indicated in Eq. (1), where f is Coriolis parameter, P is pressure, ρ_o is density, and u represents the zonal component of velocity. The Coriolis parameter f is 8.7745×10^{-5} s^{-1} so the model is invariant to ordinal rotation. A linear equation of state has been implemented in both preliminary and actual experiments, as shown in Eq. (2); α is 1.7×10^{-4} $^oC^{-1}$, T and ρ are temperature and density, while T_o and ρ_o are references for temperature and density, respectively. There is no salinity term in Eq. (2) because salinity is set to a constant value over the whole domain. Substituting Eq. (2) and the hydrostatic equation in Eq. (1) yields Eq. (3). In Fig. 2.1a and c, higher temperature on the north sides of the channel, which correspond to smaller density, lead to a positive temperature gradient along the y direction that balances the negative u gradient in z direction as shown in Fig. 2.1 (d).

$$-fu=\frac{1}{\rho_o}\frac{\partial P}{\partial y} \tag{1}$$

$$\rho=\rho_o\left[1-\alpha\left(T-T_o\right)\right] \tag{2}$$

$$\frac{\partial u}{\partial z} = -\frac{\alpha g}{f \rho_o} \frac{\partial T}{\partial y} \tag{3}$$

The westward flow reaches maximum magnitude at the surface layer. Its balancing pressure field is contributed by zonally uniform sea surface height, which is 0 cm at the south edge and linearly increased to 0.64 cm at the north edge. The Richardson number of the initial condition during the preliminary run, where N is buoyancy gradient and M is the root square of background buoyancy gradient, is 0.25 to enable both symmetric instability and baroclinic instability to take place (Stamper & Taylor, 2017; Stone, 1966).

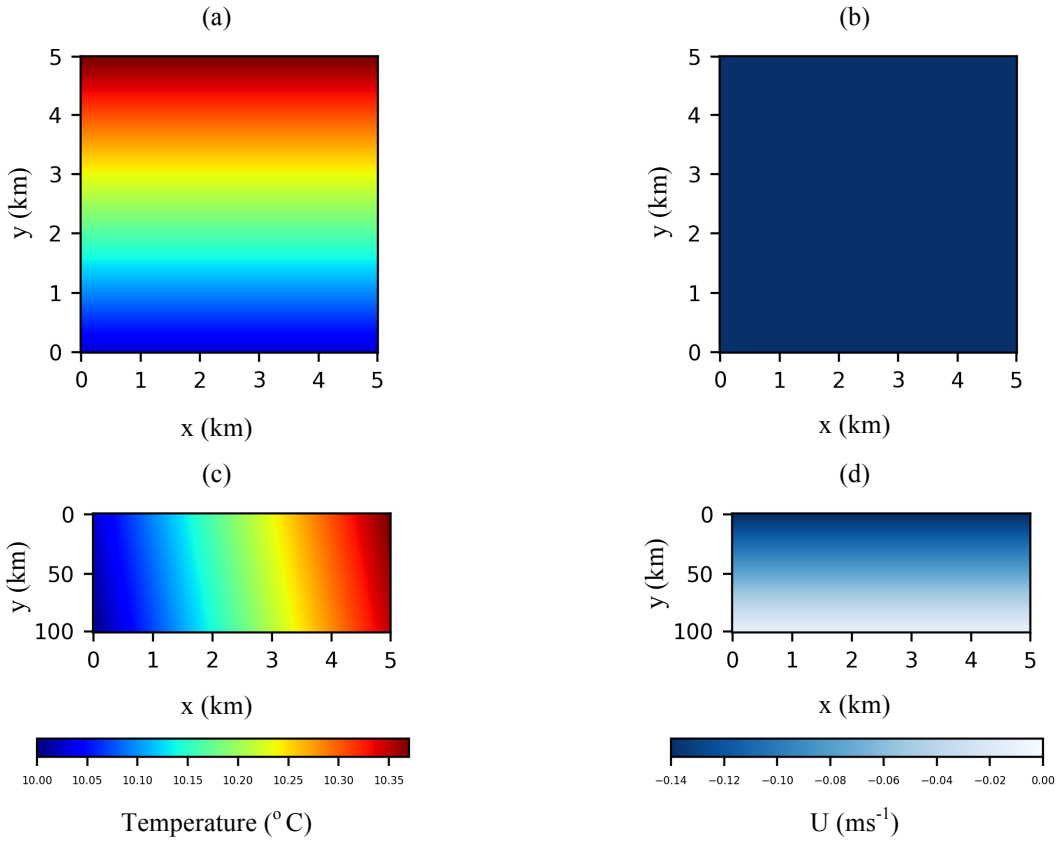

Figure 2.1: Initial temperature (left panels) and u component of current velocity (right panels) of surface layer (upper panels) and of transects of an arbitrary south-north slide (bottom panels).

2.2.2 Wind Forcing Experiments and Control Experiments

The initial condition for the wind forcing experiments is provided by the preliminary run. The preliminary run lasts for more than 25 days and its surface buoyancy evolution is shown in Fig. 3.1. Descriptions and discussions on the results of the preliminary run will be in Chapter 3. The 180th hour result in the preliminary simulation is used to initialize the wind forcing experiments because that is the point at which the submesoscale eddy is formed along with a strong front as shown in Fig. 3.1f.

Because large accelerations could be introduced by wind forcing at the ocean surface grids in the wind forcing experiments, Courant-Friedrichs-Lewy (CFL) conditions of the high-resolution experimental simulations are too demanding to be satisfied with the small values of isotropic viscosity and thermal diffusivity set in the preliminary run. Thus, in the wind forcing experiments, the horizontal viscosity and diffusivity are set to 0.1 m^2s^{-1}, and the vertical viscosity and diffusivity to 0.005 m^2s^{-1} in order to satisfy the CFL conditions referred to in (Thomas & Lee, 2005). Besides the change in viscosity and diffusivity values, all other ocean model parameters in the wind forcing experiments remain the same as in the preliminary run.

The basic equation of CheapAML

$$s_t + \nabla \cdot \left(\vec{u}s\right) = -F_Z + \nabla \cdot \left(K \nabla s\right) - \lambda\left(s - s_{c\lim}\right) \tag{4}$$

where s is the tracer of atmospheric potential temperature or water vapor content, and s_{clim} is the climate value of s, vector $\vec{u}$ is the velocity vector, F_z represents the vertical flux term, κ is the diffusivity, and λ is the timescale inverse of the relaxation term. When λ is a large value, s can be nudged to s_{clim}. But if λ is a small value or close to zero, s will not be significantly nudged to a climate value.

Experiments are run using CheapAML and six wind fields to force the ocean processes: 8 ms-1 westward wind, 4 ms-1 westward wind, 1 ms-1 westward wind, 1 ms-1 eastward wind, 4 ms-1 eastward wind, and 8 ms-1 eastward wind. No meridional wind is prescribed in the experiments. For each wind forcing case, four simulations are conducted with different air-sea schemes: (1) Both surface current coupling and thermodynamic coupling are turned off (Uncoupled, Current Not Considered); (2) surface current coupling is switched on but thermodynamic coupling is turned off (Uncoupled, Current Considered); (3) surface current

coupling is switched off but thermodynamic coupling is turned on (Coupled, Current Not Considered);

Table 1: Name table of control experiments and wind forcing experiments.

Wind Speed (ms^{-1})	Wind Direction	Thermodynamic Coupling	Surface Current Coupling	Experiment Name
0	-	Off	Off	Control-UN
0	-	Off	On	Control-UC
0	-	On	Off	Control-CN
0	-	On	On	Control-CC
1	Westward	Off	Off	Exp1W-UN
1	Westward	Off	On	Exp1W-UC
1	Westward	On	Off	Exp1W-CN
1	Westward	On	On	Exp1W-CC
4	Westward	Off	Off	Exp4W-UN
4	Westward	Off	On	Exp4W-UC
4	Westward	On	Off	Exp4W-CN
4	Westward	On	On	Exp4W-CC
8	Westward	Off	Off	Exp8W-UN
8	Westward	Off	On	Exp8W-UC
8	Westward	On	Off	Exp8W-CN
8	Westward	On	On	Exp8W-CC
1	Eastward	Off	Off	Exp1E-UN
1	Eastward	Off	On	Exp1E-UC
1	Eastward	On	Off	Exp1E-CN
1	Eastward	On	On	Exp1E-CC
4	Eastward	Off	Off	Exp4E-UN
4	Eastward	Off	On	Exp4E-UC
4	Eastward	On	Off	Exp4E-CN
4	Eastward	On	On	Exp4E-CC
8	Eastward	Off	Off	Exp8E-UN
8	Eastward	Off	On	Exp8E-UC
8	Eastward	On	Off	Exp8E-CN
8	Eastward	On	On	Exp8E-CC

Note: The last second letter represents coupled (C, thermodynamic coupling switched on) or uncoupled (U, thermodynamic coupling switched off), and the last letter indicates whether the current effect is considered (C, surface current coupling switched on) or do not consider current effect (N, surface current coupling switched off). The fourth digit represents the wind speed magnitude (unit: ms^{-1}), and the fifth letter represents wind direction (E: eastward; W: westward).

and (4) both surface current coupling and thermodynamic coupling are switched on (Coupled, Current Considered). These wind stress formulations are given by:

$$\tau = \rho C_D\left(T_{climate}, SST, \vec{U}\right)\left(\vec{U}\right)\left|\vec{U}\right| \tag{5}$$

$$\tau = \rho C_D\left(T_{climate}, SST, \vec{U}-\vec{U}_{sfc}\right)\left(\vec{U}-\vec{U}_{sfc}\right)\left|\vec{U}-\vec{U}_{sfc}\right| \tag{6}$$

$$\tau = \rho C_D\left(T_{atm}, SST, \vec{U}\right)\left(\vec{U}\right)\left|\vec{U}\right| \tag{7}$$

$$\tau = \rho C_D\left(T_{atm}, SST, \vec{U}-\vec{U}_{sfc}\right)\left(\vec{U}-\vec{U}_{sfc}\right)\left|\vec{U}-\vec{U}_{sfc}\right| \tag{8}$$

Wind stress is calculated according to Eqs. (5), (6), (7), and (8) in these four cases, respectively. In Eqs. (5-8), τ is wind stress, ρ is density, C_D is drag coefficient, which is also a function of atmospheric potential temperature ($T_{climate}$: prescribed; or T_{atm}: adjustable), SST, and wind velocity (U). Vector U_{sfc} represents ocean current velocity. Note that wind velocity fields are prescribed in all simulations since CheapAML is not able to resolve dynamics in the atmosphere mixed layer. The prescribed atmospheric potential temperature ($T_{climate}$) is the averaged sea surface temperature over the horizontal domain at 180th hour of the preliminary run.

All wind forcing experiments run for 48 hours. The results of these experiments are analyzed and discussed in Chapters 4 and 5. In order to have a reference for comparison, simulations forced by 0 ms^{-1} wind using the four air-sea schemes are also conducted. These 0 ms^{-1} wind forcing simulations are called control experiments in this study. They have the same initial condition and viscosity and diffusivity values as the wind forcing experiments.

Table 1 lists all of these experiments and distinguishes between the control experiments and wind forcing experiments with different wind speeds, wind directions, and air-sea schemes.

CHAPTER 3

GENERAL DESCRIPTION OF NUMERICAL SIMULATIONS

3.1 Submesoscale Generation

In the preliminary run, submesoscale processes including symmetric cells, eddy, front, and small-scale Kelvin-Helmholtz instabilities are generated. These processes could be reflected by surface buoyancy evolution in Fig. 3.1 and velocity fields in Fig. 3.2.

The preliminary run started from a geostrophic flow. The initial surface buoyancy field in Fig. 3.1a corresponds to the initial SST field in Fig. 2.1a. According to linear stability theory (Stamper & Taylor, 2017; Stone, 1966), both symmetric instability and baroclinic instability are expected to take place because the Ri is set to 0.25 for the initial flow. The parallel symmetric instability cells develop faster than the baroclinic instability. This is reflected by the surface buoyancy field away from south and north boundaries at the 39^{th} hour in Fig 3.1b. The dynamics close to boundaries are contaminated by interactions between geostrophic adjustment and closed boundaries. To avoid the boundary effects, only the evolution of the symmetric instability in the central portion of the channel is analyzed, as illustrated in Fig. 3.2. Fig. 3.1c shows mixed modes of symmetric and baroclinic instability, as symmetric instability become saturated and baroclinic instability is well-developed and is revealed from the baroclinic wave pattern.

Baroclinic instability becomes dominant around the 78^{th} hour, as shown in Fig. 3.1d, in which the surface field is filled with developed baroclinic waves. Around 40 hours later, a submesoscale eddy is formed along with a strong front alongside its south side (Fig. 3.1f). At this point, most of the surface is filled with large buoyancy values. This indicates that submesoscale stratification has flattened isopycnals a great deal compared to the initial ones. Figs. 3.1g through 3.1i illustrate further developments of the submesoscale eddy. At the 612^{th} hour, the eddy is isolated from the zonal current; the lighter color around the eddy in Fig. 3.1i is a consequence of both mixing and diffusion.

Both snapshots of meridional and vertical velocity components, V and W, at the 39^{th} hour in Figs 3.2a and 3.2b, reveal a structure of parallel cells. In the parallel convective cells, strong positive and negative vertical velocities are aligned with each other with magnitudes of about 1 cm s^{-1}. This is about two orders of magnitude larger than typical vertical velocity in mesoscale,

which is about O(10^{-4} ms^{-1}) (Thomas et al., 2007). Three hours later, these symmetric instability cells become much stronger. Southward cross-front flow at the surface and northward cross-front flows at the bottom become obvious in Fig. 3.2b. Small-scale secondary Kelvin-Helmholtz instabilities start to break symmetric instability cells around the 45th hour. Comparing that against snapshots at the 42nd hour, stronger cross-front flows and vertical velocities are revealed in Figs 3.2c and 3.2f, respectively.

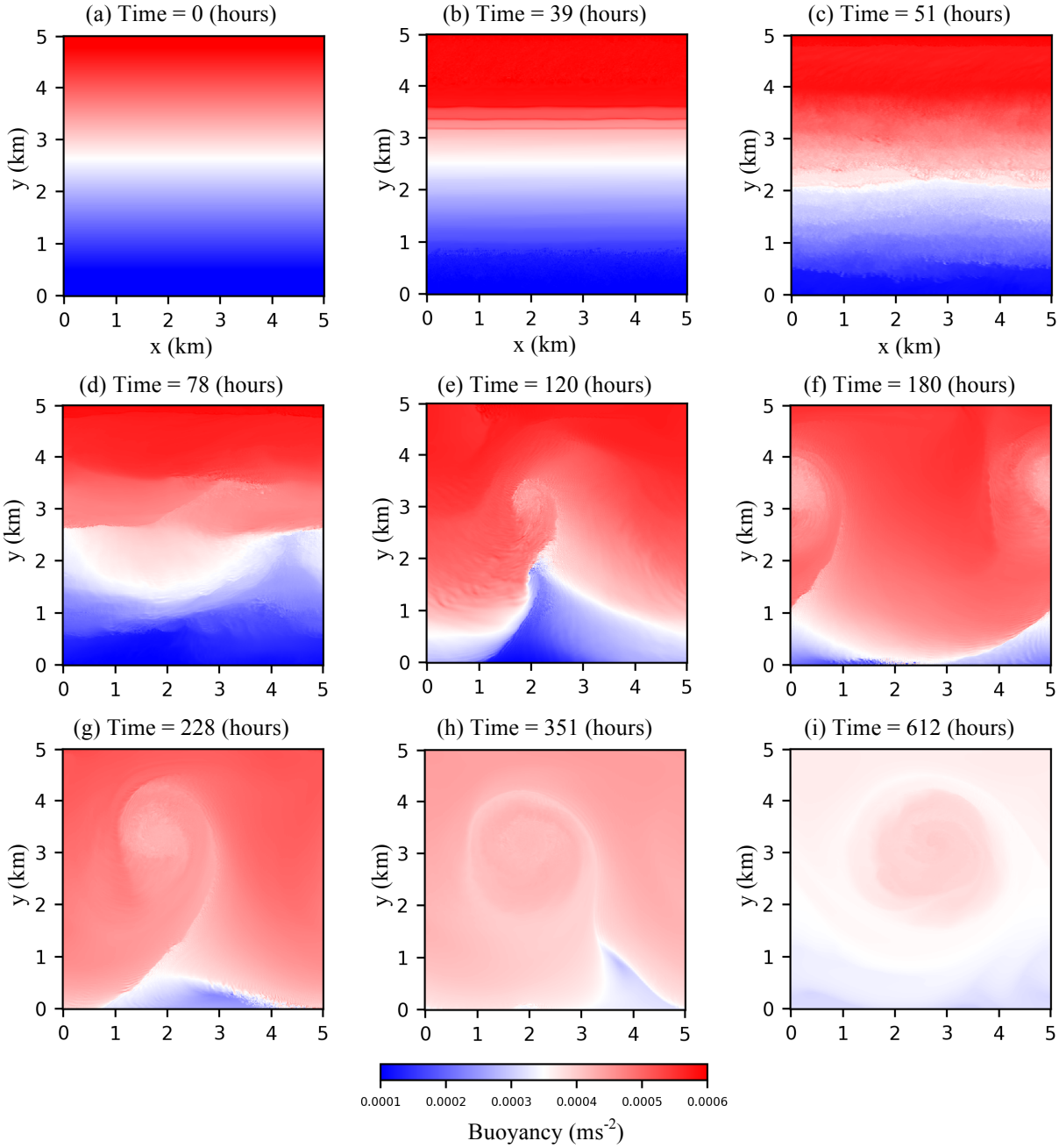

Figure 3.1: The evolution of surface buoyancy for preliminary run.

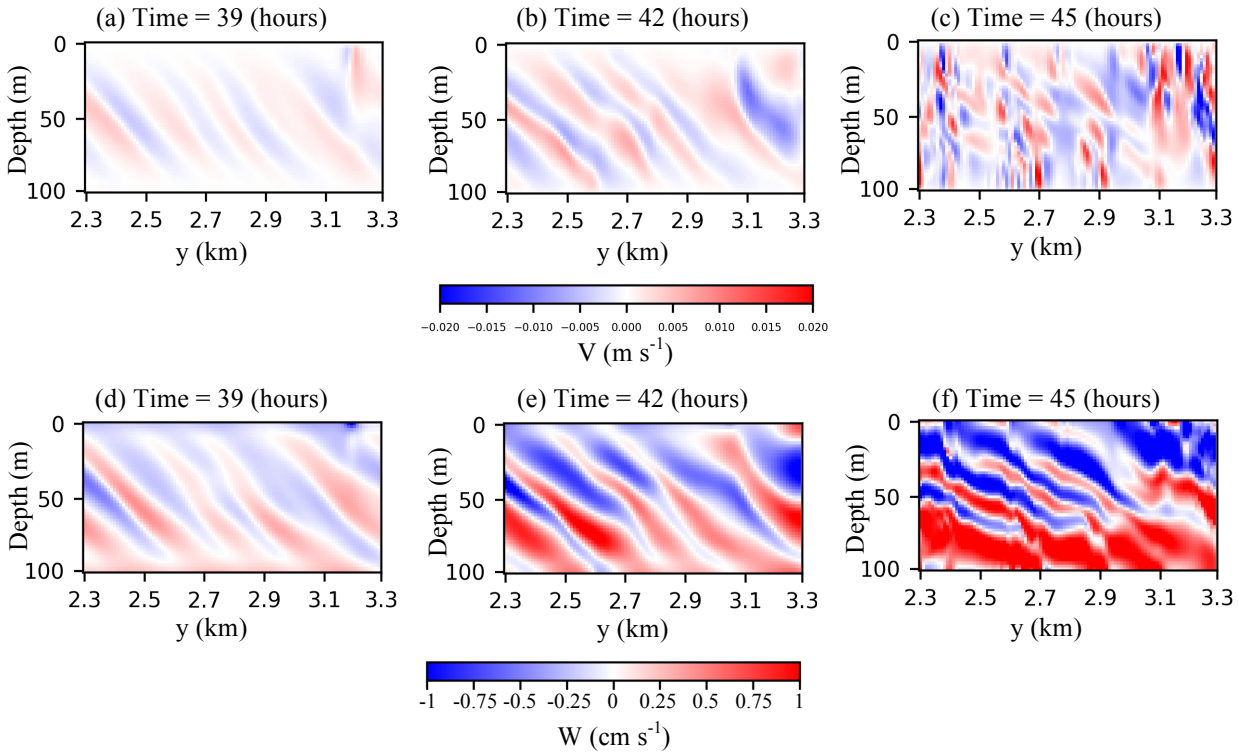

Figure 3.2: The evolution of symmetric instability convection cells, and the development of secondary Kelvin-Helmholtz instability between symmetric cells in cross-front V (a-c) and W (d-f) fields in preliminary run.

Because similar simulations of the symmetric and baroclinic instability have been conducted by Stamper et al., (2017), thus, tautological analysis on them is not conducted here. Instead, air-sea interactions over the submesoscale processes is investigated. As mentioned in section 2.2.2, preliminary simulation at the 180th hour (Fig. 3.1f) is used as the initial condition in the wind forcing experiments. The initial condition is chosen as both the submesoscale eddy and front are formed. Because the symmetric instability damps in a few hours, no wind experiment is conducted over the surface symmetric instability bands that appears in the preliminary run. Contaminations from baroclinic instability and secondary Kevin-Helmholtz instability also impede the investigation on air-sea interaction over pure symmetric instability.

3.2 Control Experiments and Wind Forcing Experiments

3.2.1 Westward Wind Forcing

Westward winds of 1 ms^{-1}, 4 ms^{-1}, and 8 ms^{-1} are added to force the evolution of submesoscale eddy and front formed at the 180th hour in the preliminary run. Because the water

body flows westward, the westward wind is expected to inject negative potential vorticity into the water to further reduce its stability. The interest of this study focus on how the submesoscale processes evolve under these westward wind forces.

3.2.1.1 1 ms^{-1} westward wind forcing. The evolution of surface Rossby number (ζ/f, where ζ is relative vorticity) for simulations with the four air-sea schemes forced by 1 ms^{-1} westward wind are shown in Fig. 3.4. Only results for the last 24 hours are shown and compared because the wind forcing is applied and the parameters of viscosity and diffusivity have been changed from the preliminary run. the first 24 hours is set to allow for the adjustments that took place.

In Fig. 3.4, differences in Rossby number evolution between Exp1W-UN, Exp1W-UC, Exp1W-CN, and Exp1W-CC are not obvious as the magnitude of 1 ms^{-1} wind forcing is small. Comparing Figs. 3.4 (c), (f), (i), and (l), eddies in those experiments activated surface current coupling propagate a little slower than the ones in experiments deactivated surface current coupling. When both wind and water move in the same direction, the $\vec{U}-\vec{U}_{sfc}$ term in Eq. (6) and Eq. (8) yields smaller wind stresses when surface current coupling is switched on. Compared to the control experiments in Fig. 3.3 regardless of which air-sea scheme is used, the eddies forced by 1 ms^{-1} wind move westward faster than those in the control runs. However, no significant difference in the eddy size and the front shape are detected between the Control- and Exp1W- experiments.

3.2.1.2 4 ms^{-1} westward wind forcing. The evolution of the surface Rossby number field for Exp4W- experiments are shown in Fig. 3.5. Significant differences in the front shape and eddy structure are observed among the four experiments.

Fig. 3.5a is the surface Rossby number field of Exp4W-UN at the 24th hour, in which the front tail has left the southern boundary and starts to break. However, in the Exp4W-UC (Fig. 3.5d, there is no indication of front breaking on the tail yet. At the 36th hour in Exp4W-UN (Fig. 3.5b), most of the front breaks into several segments, while the front in Exp4W-UC, (Fig. 3.5e) still maintains half of its integrity. The shapes of the broken fronts in Exp4W-UN and Exp4W-UC, consisting of intermittent segments, show a remarkable discrepancy at the 48th hour. Similar front features can be detected when comparing Exp4W-CN and Exp4W-CC (Figs. 3.5i and 3.5l).

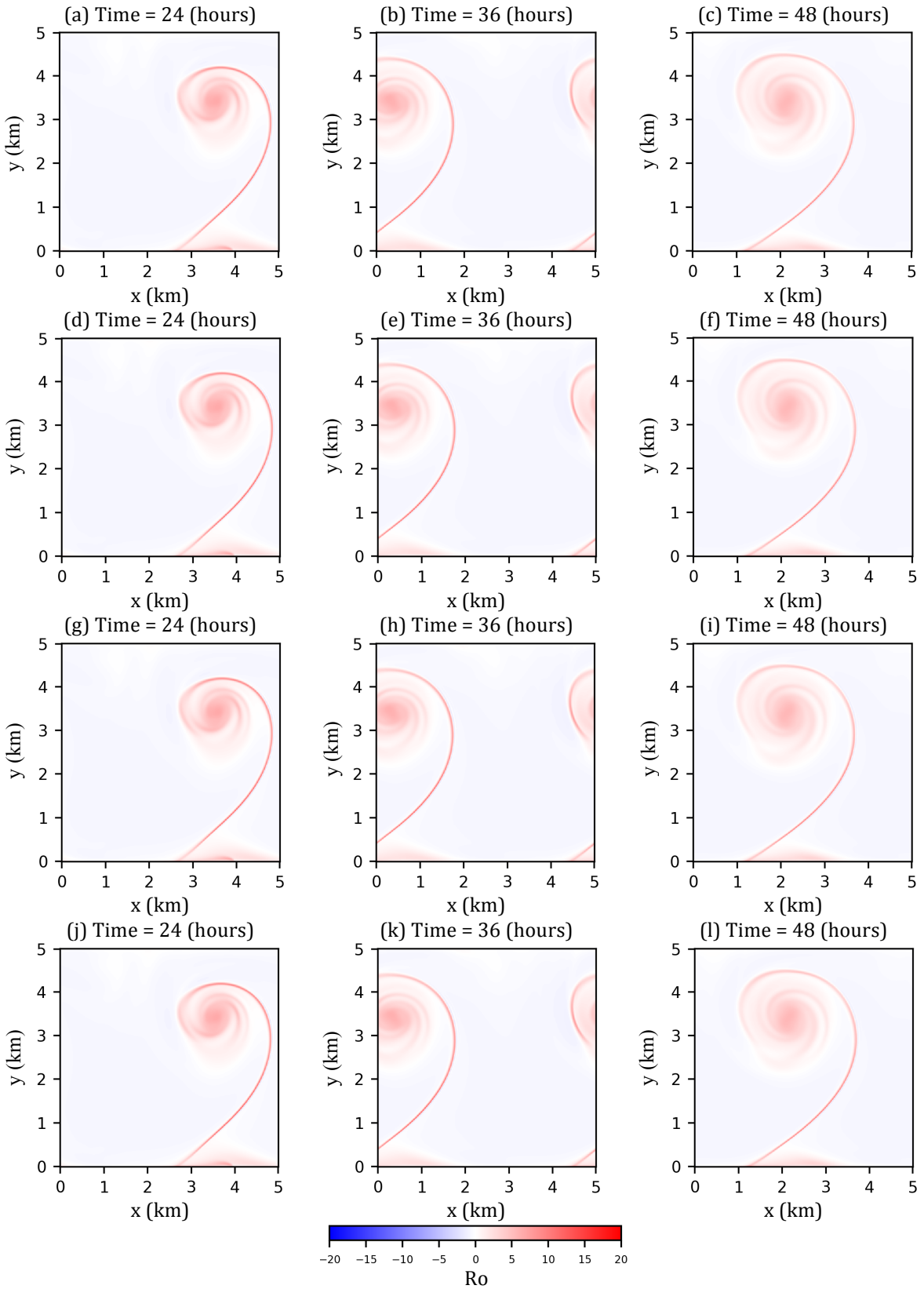

Figure 3.3: Surface Ro fields at the (a) 24th hour, (b) 36th hour, and (c) 48th hour for Control-UN; (d-f) for Control-UC; (g-i) for Control-CN; and (j-l) for Control-CC.

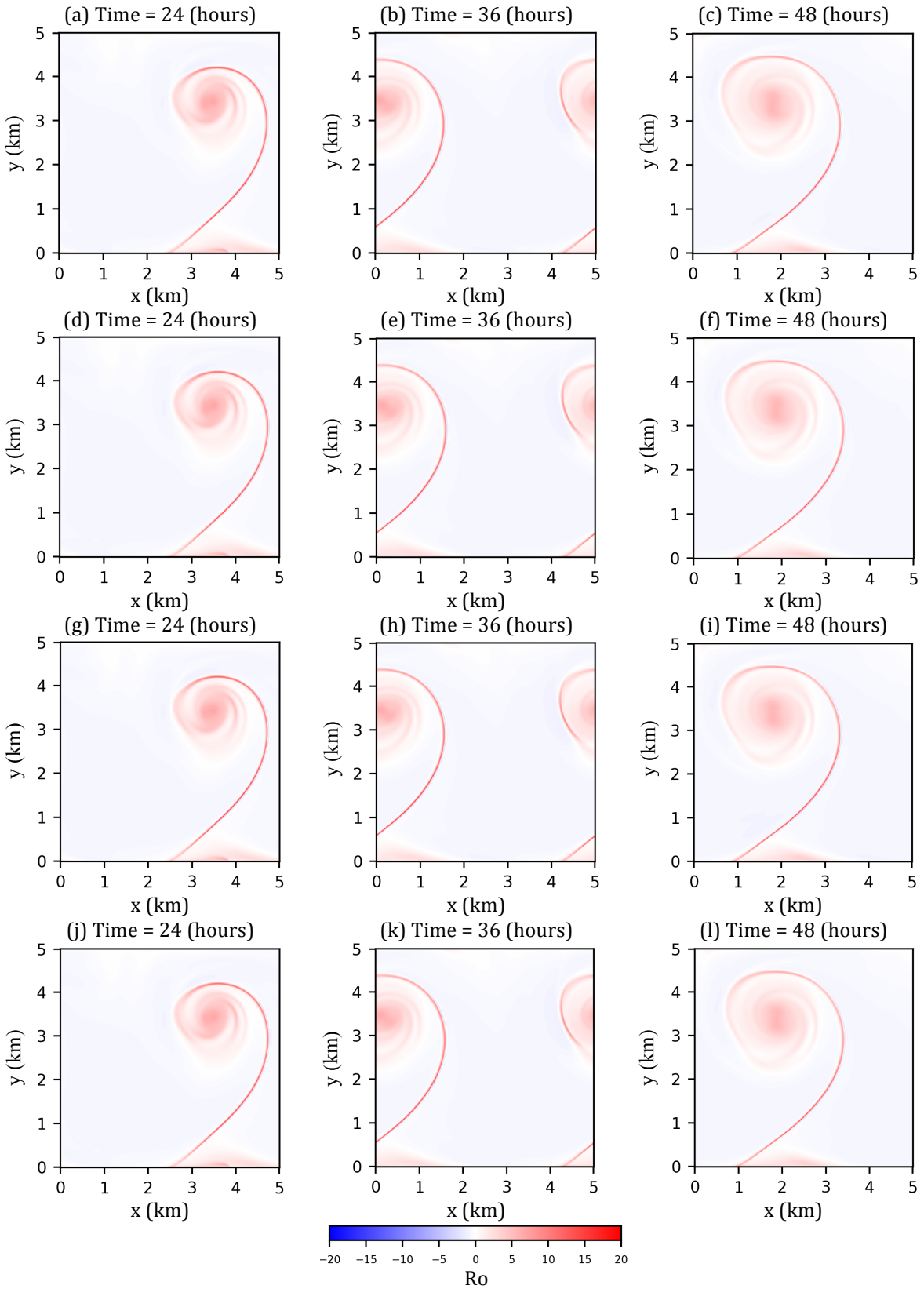

Figure 3.4: Surface Ro fields at the (a) 24th hour, (b) 36th hour, and (c) 48th hour for Exp1W-UN; (d-f) for Exp1W-UC; (g-i) for Exp1W-CN; and (j-l) for Exp1W-CC.

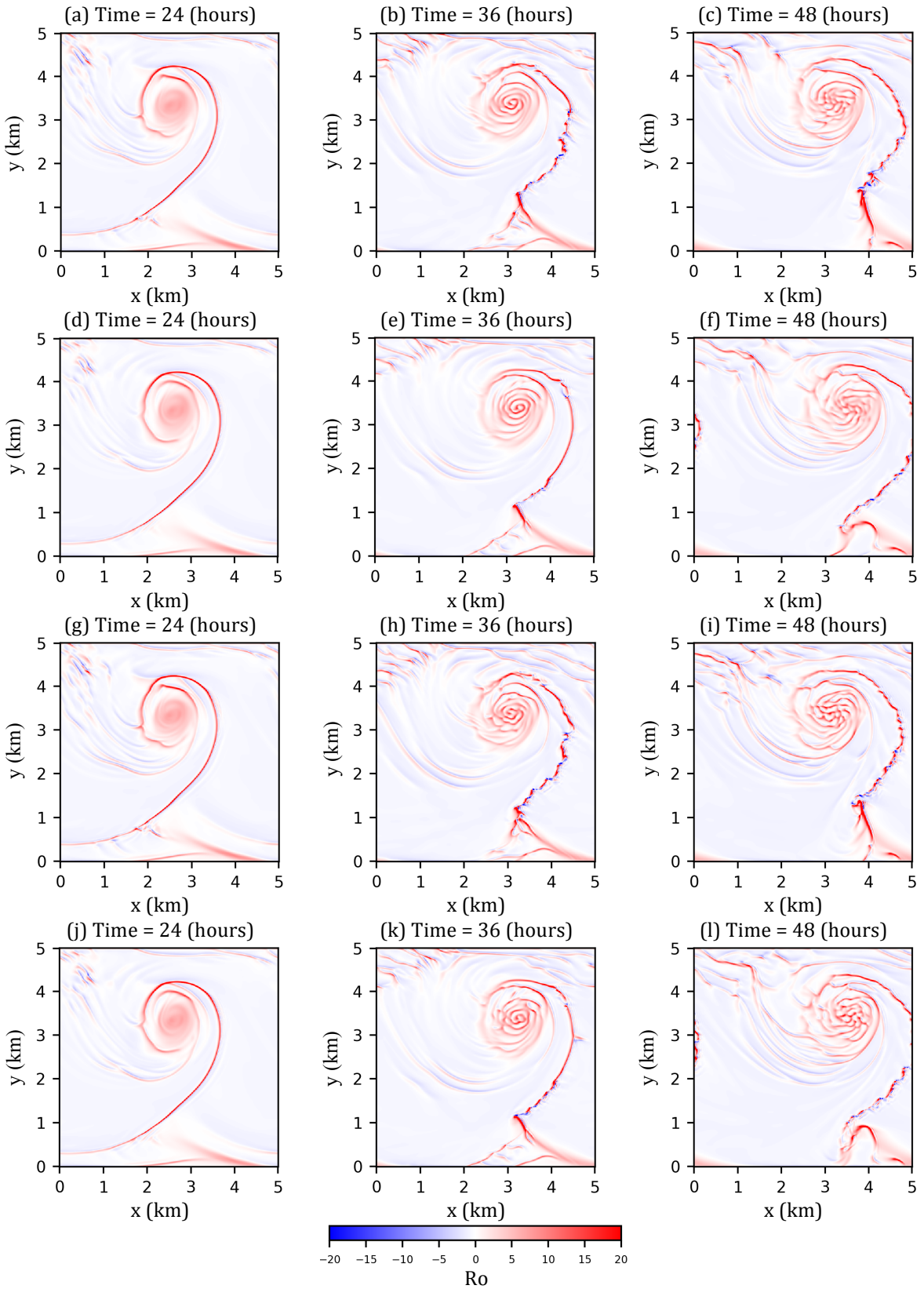

Figure 3.5: Surface Ro fields at the (a) 24th hour, (b) 36th hour, and (c) 48th hour for Exp4W-UN; (d-f) for Exp4W-UC; (g-i) for Exp4W-CN; and (j-l) for Exp4W-CC.

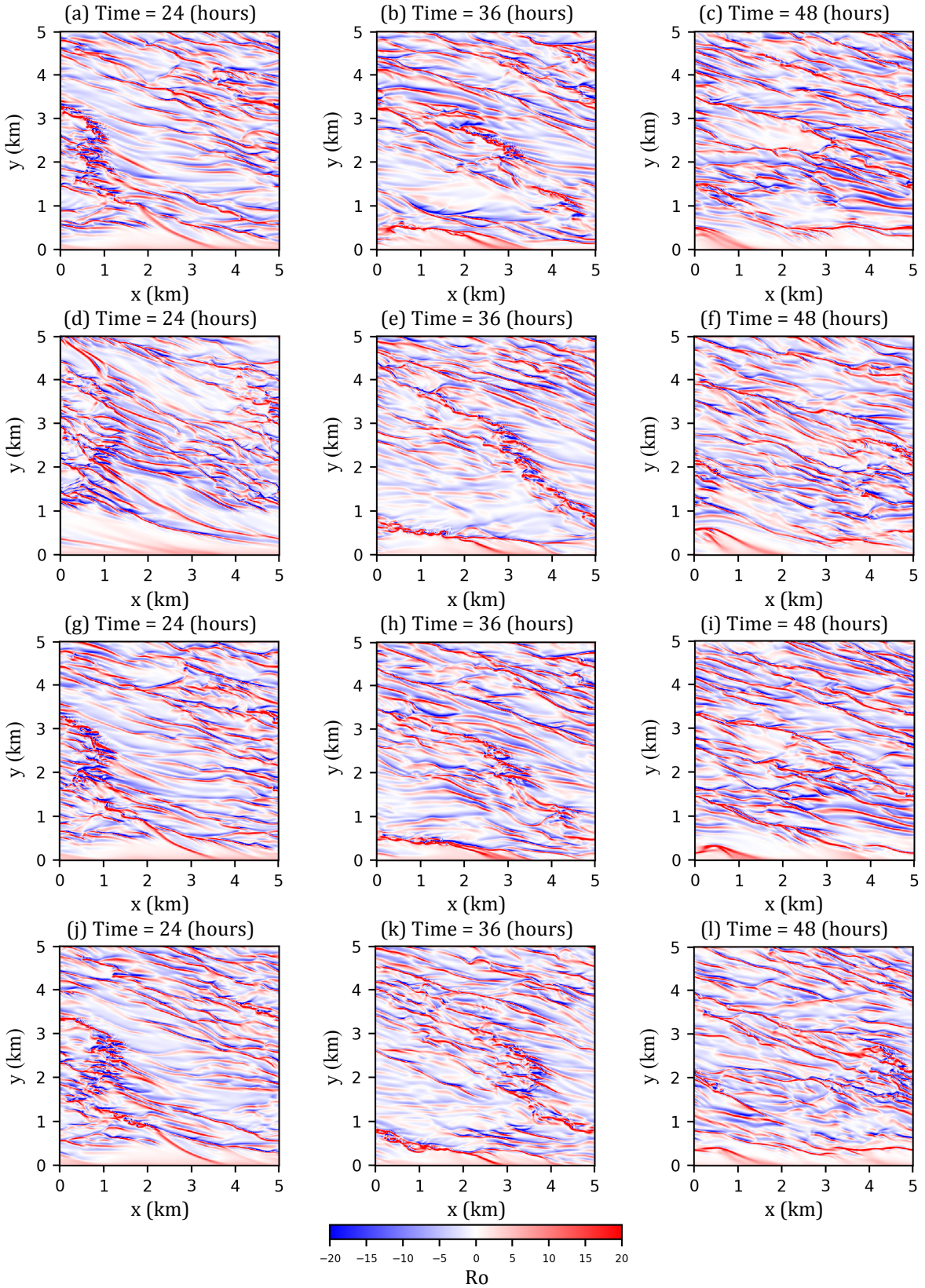

Figure 3.6: Surface Ro fields at the (a) 24th hour, (b) 36th hour, and (c) 48th hour for Exp8W-UN; (d-f) for Exp8W-UC; (g-i) for Exp8W-CN; and (j-l) for Exp8W-CC.

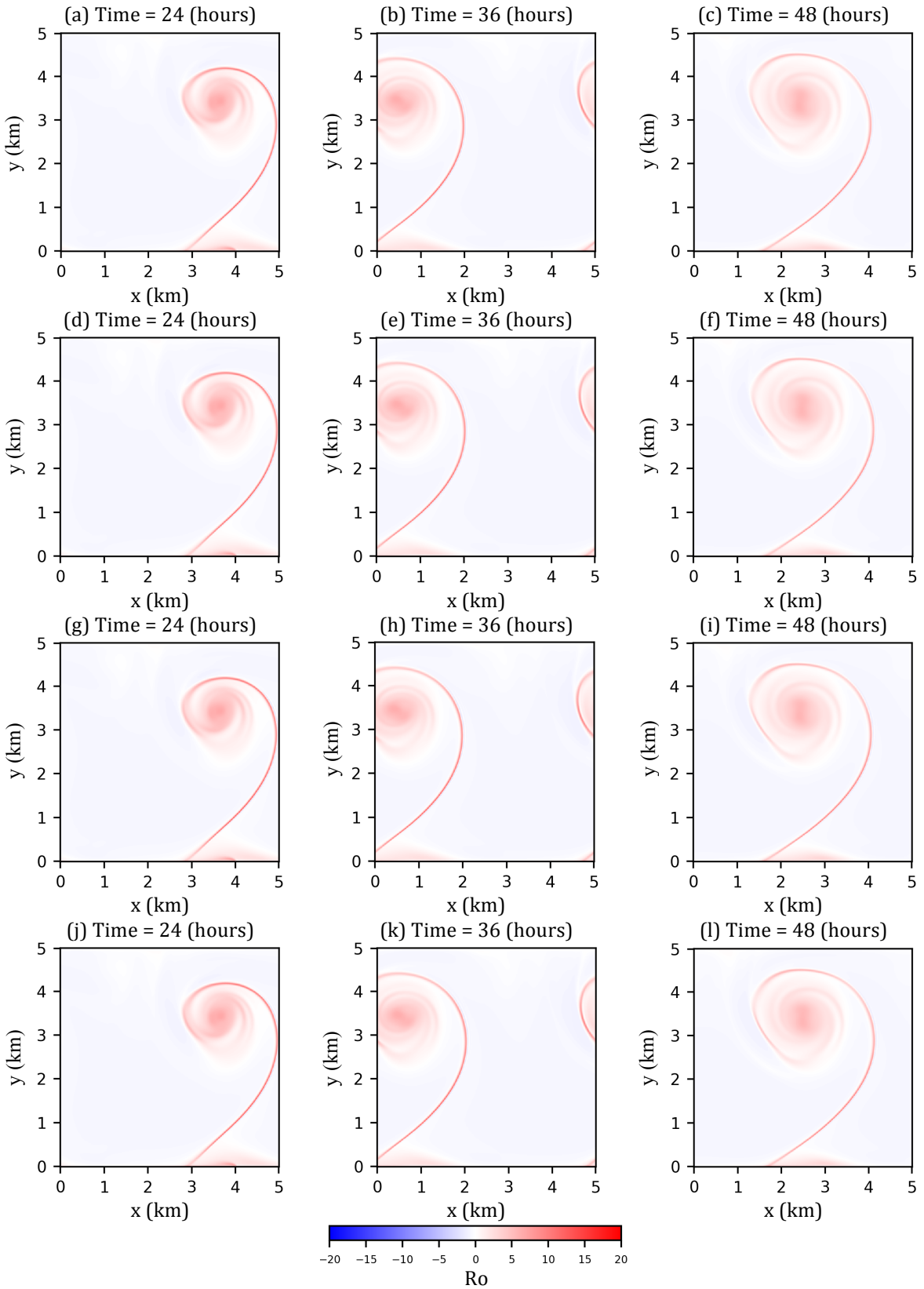

Figure 3.7: Surface Ro fields at the (a) 24th hour, (b) 36th hour, and (c) 48th hour for Exp1E-UN; (d-f) for Exp1E-UC; (g-i) for Exp1E-CN; and (j-l) for Exp1E-CC.

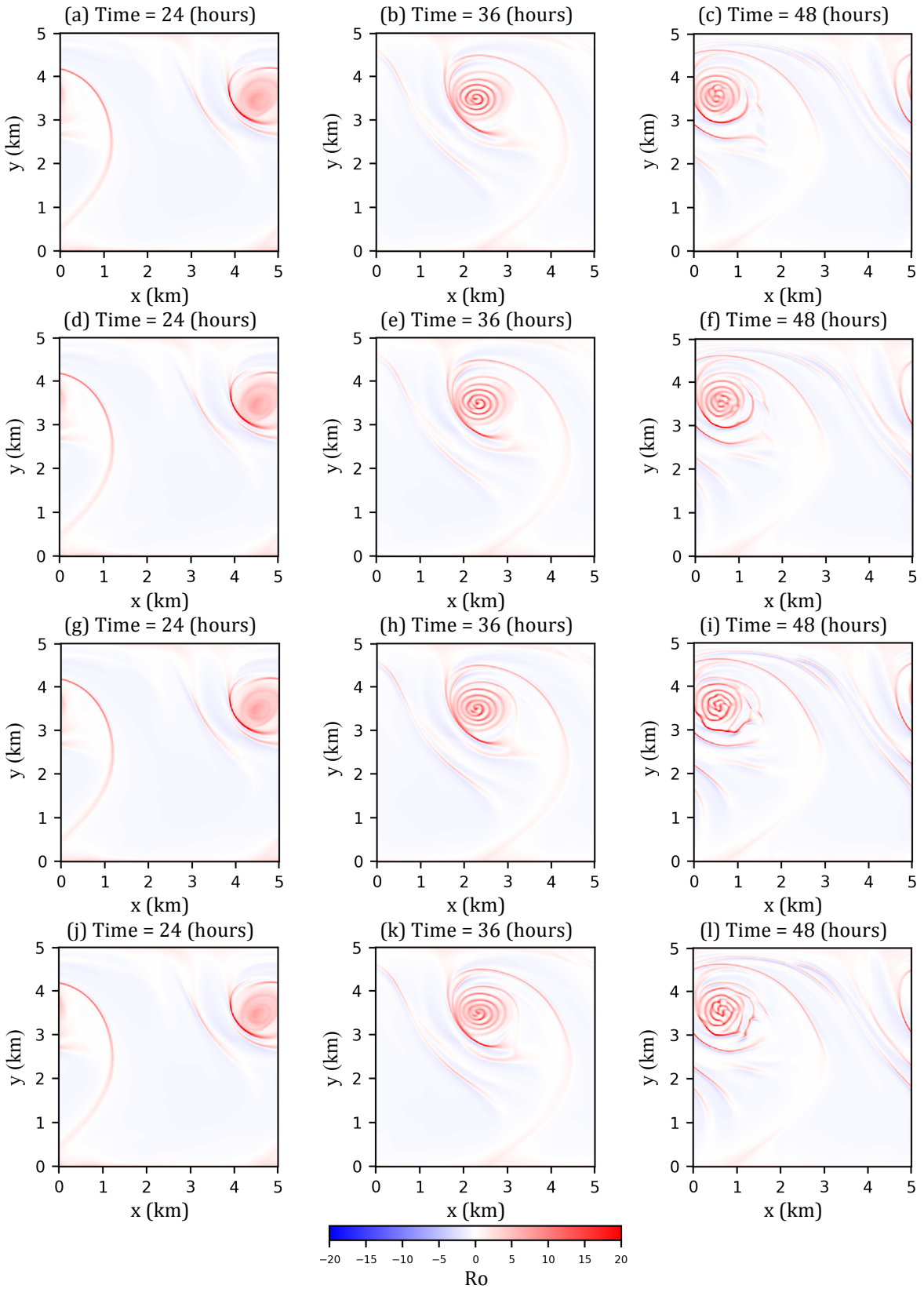

Figure 3.8: Surface Ro fields at the (a) 24th hour, (b) 36th hour, and (c) 48th hour for Exp4E-UN; (d-f) for Exp4E-UC; (g-i) for Exp4E-CN; and (j-l) for Exp4E-CC.

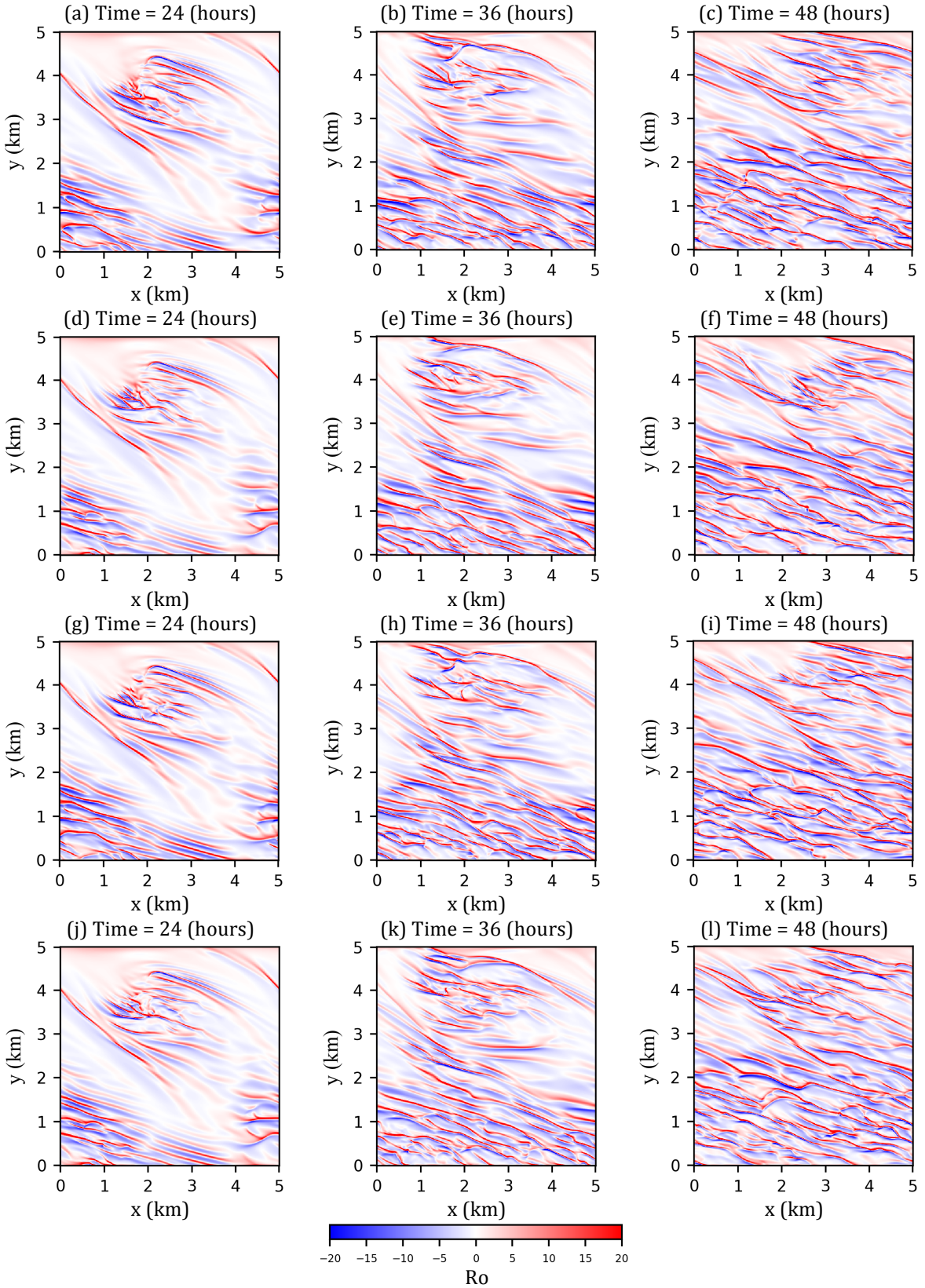

Figure 3.9: Surface Ro fields at the (a) 24th hour, (b) 36th hour, and (c) 48th hour for Exp8E-UN; (d-f) for Exp8E-UC; (g-i) for Exp8E-CN; and (j-l) for Exp8E-CC.

However, no significant difference in Exp4W-UC and Exp4W-CC front developments are found, and the same is true for Exp4W-UN and Exp4W-CN. Thus, It can be concluded that the evolution of submesoscale front is more sensitive to the surface current coupling rather than the thermodynamic coupling.

The evolution of eddies in the Exp4W- experiments are also revealed in Fig. 3.5. The locations of eddies at the 48th hour imply that the eddies in Exp4W-UC and Exp4W-CC propagate slower than those in Exp4W-UN and Exp4W-CN. In all four air-sea-scheme experiments, the relative vorticity field of eddies evolves from a smooth field surrounding the eddy center at the 24th hour into concentric circles consisting of sharp high Ro strips at the 36th hour. Finally, these sharp high Ro strips intertwine with each other and form a crisscross pattern at the 48th hour.

Compared the Control- and Exp1W- experiments, eddies in the Exp4W- experiments propagate faster and the front breaking appears. The uniform relative vorticity field in the Exp4W- experiments evolves into sharp high Ro strips, while the one in Control- and Exp1W- experiments only enlarges its size and stays uniform.

3.2.1.3 8 ms^{-1} westward wind forcing. A strong wind forcing of 8 ms-1 generates symmetric instabilities in the model simulation. Fig. 3.6 shows the surface field of Ro number of the Exp8W- experiments. After 24 hours, no eddy structure is recognizable in the channel after forcing. Instead, sharp strips of large positive and negative Ro numbers are observed in all Exp8W- experiments. All the panels in Fig. 3.6 show the strips of high positive and negative Ro number. Their structures are not identical when they are compared in local details. If these large Ro number structures are associated with air-sea exchange or vertical fluxes, it would be questionable if these non-identical structures would yield to domain-averaged differences in air-sea fluxes or mixed layer processes. These questions will be investigated and discussed in Chapter 4 and Chapter 5.

3.2.2 Eastward Wind Forcing

Eastward winds of 1 ms^{-1}, 4 ms^{-1}, and 8 ms^{-1} are used to force the evolution of submesoscale eddy and front. As the forcing wind direction is opposite the initial flow in the channel, positive potential vorticity is expected to be injected into the water, which will stabilize

it. Similar to the westward wind forcing experiments, how the submesoscale processes evolve under these eastward wind forces is firstly studied.

3.2.2.1 1 ms^{-1} eastward wind forcing. Evolution of surface Rossby number fields for simulations using the four air-sea schemes forced by 1 ms^{-1} eastward wind are shown in Fig. 3.7. The eddy locations at the 24th hour, 36th hour, and 48th hour all reflect a slower propagation speed than is seen in the control experiments. The front tail touches the south boundary through the experiment period. During the last 24 hours, no sharp large Ro strips are formed but the size of the eddy increases. The differences in Ro fields of Exp1E-UN, Exp1E-UC, Exp1E-CN, and Exp1E-CC are not significant.

3.2.2.2 4 ms^{-1} eastward wind forcing. Fig. 3.8 shows the evolution of surface Rossby number fields for simulations using the four air-sea schemes forced by a 4 ms^{-1} eastward wind. The eddy shows a slower propagation speed than is seen in the control experiments. Additionally, the strong front in the control experiments is weakened by the wind forcing with opposite direction to the flow. On the upwind side of the eddy, a strong front appears during the last 24 hours. In contrast to the Exp4W- experiments, no front breaking is detected in the Exp4E- experiments. Sharp strips of large Ro form in the Exp4E- experiments as well, and they are much closer to concentric circles in shape. At the 48th hour, the strips in the central part of the eddy begin to mingle with each other. The differences in the Ro fields of Exp4E-UN, Exp4E-UC, Exp4E-CN, and Exp4E-CC are not remarkable, however, the flow in experiments with surface current coupling turned on moves slower than the flow in experiment with surface current coupling switched off.

3.2.2.3 8 ms^{-1} eastward wind forcing. The evolution of surface Rossby number fields in the Exp8E- experiments are shown in Fig. 3.9. Forced by strong eastward wind of 8 ms^{-1} for 24 hours, no eddy structure is detected. Similar to the Exp8W- experiments, symmetric instability structures of sharp strips of large positive and negative Ro numbers are formed in the channel. However, comparing the Exp8W- and Exp8E- experiments at the 24th hour, the domain of the Exp8E- experiments contain fewer sharp Ro strips. The general patterns the Ro fields of the Exp8E- experiments are similar at the 24th hour. However, at the 48th hour the Ro strips are not

identical when they are compared locally. In Chapter 4 and Chapter 5, whether domain-averaged differences of air-sea fluxes are introduced over the various the non-identical Ro strips is discussed.

CHAPTER 4

WIND STRESS AND HEAT FLUXES IN SUBMESOSCALE REGIME

4.1 Wind Stress Adjustments in Submesoscale Regime

Wind stress adjustments to warm and cool water imply wind stress curl and divergence can be formed over crosswind and downwind SST gradients. Satellite observations have revealed a linear relationship between crosswind/downwind SST gradients and wind stress curl/divergence in mesoscale regimes (Chelton et al., 2004). In submesoscale regimes, much stronger SST gradients have been observed and numerically simulated (D'Asaro et al., 2010; McWilliams, 2016; Stamper & Taylor, 2017). The relationship between wind stress curl/divergence and SST gradients are investigated in this study. As the relative vorticity in mesoscale is usually very small, the effect of current curl on wind stress curl has typically been ignored except in the case of strong eddies and sharp fronts (Dewar & Flierl, 1987; Gaube et al., 2015). Because the submesoscale processes exhibit Ro of O(1), the submesoscale regime is expected to be strongly affected by the current. In this study wind stress curl/divergence over the submesoscale regime is investigated on how it is associated with crosswind/downwind SST gradients and current curl/divergence.

4.1.1 Wind Stress Curl over Submesoscale Structures

Figs. 3.3-3.9 illustrate the abundance of submesoscale processes in numerical experiments. Different submesoscale structures can be introduced by a variety of generation mechanisms. Three prominent submesoscale structures catch attention when they are revealed by surface fields of Ro: submesoscale eddy, and front and surface bands of symmetric instability. The wind stress curl fields of Exp4W-CC and Exp8W-CC at the 24^{th} hour are shown in Figs. 4.1d and 4.1h. The wind stress fields over the ocean field of Exp4W-CC at the 24^{th} hour have been calculated using the other three air-sea schemes and they are shown in Figs. 4.1a-c. In Fig. 4.1a, both the thermodynamic coupling and the surface current coupling are deactivated. In Fig. 4.1b, the thermodynamic coupling is deactivated but the surface current coupling is switched on, and in Fig. 4.1c, the thermodynamic coupling is switched on but the surface current coupling is

turned off. The wind stress fields of Exp4W-UN, Exp4W-UC, Exp4W-CN, and Exp4W-CC are not directly compared, because the ocean fields in them evolve distinctly with different air-sea schemes. For example, in the Exp4W- experiments, the eddy propagates westward slower when the surface current coupling is turn on. Figs. 4.1e-g shows wind stress curl fields over the ocean field of Exp8W-CC calculated using three air-sea schemes used in Fig. 4.1a-c.

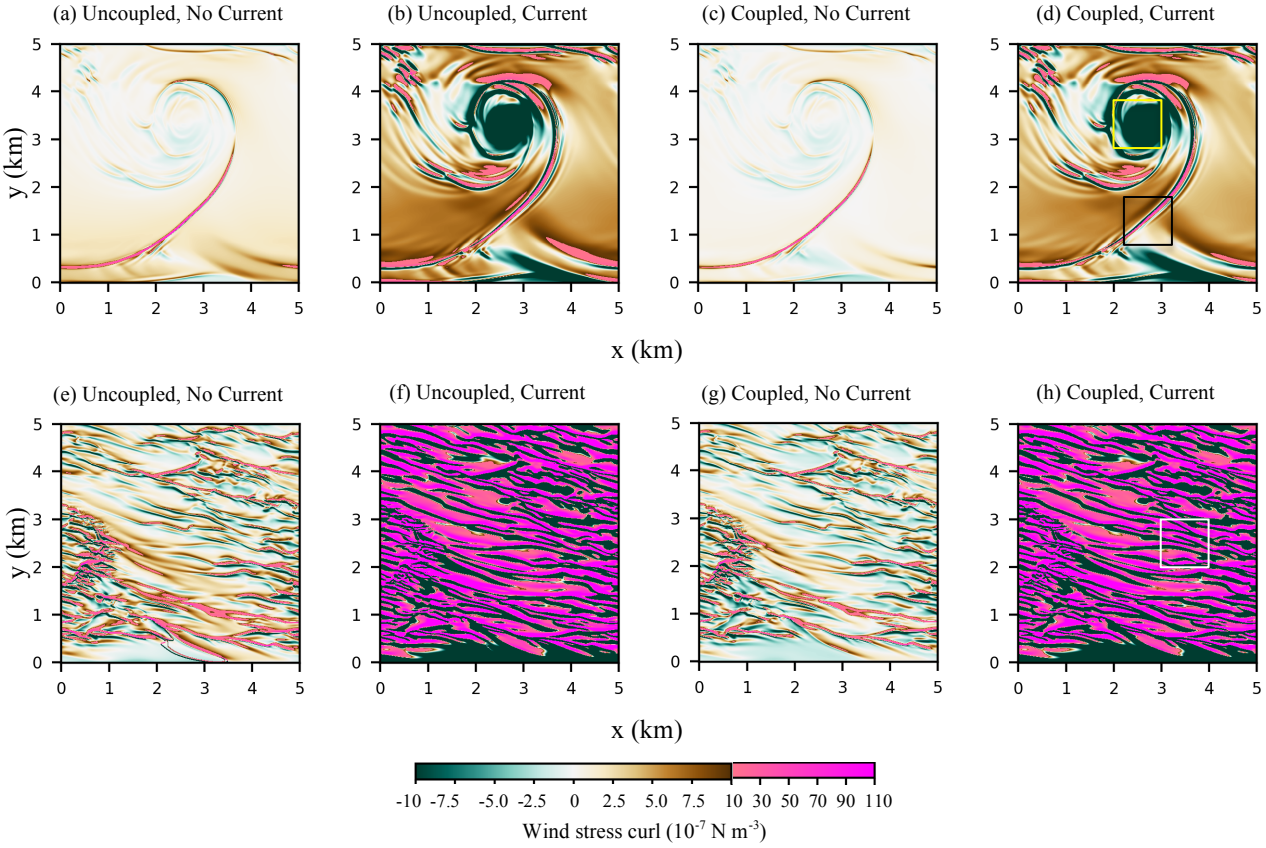

Figure 4.1: Wind stress curl of Exp4W-CC and Exp8W-CC at the 24th hour (d, h). The wind stress are recalculated from air-sea schemes with both thermodynamic coupling and surface current coupling switched off (a, e), thermodynamic coupling switched off but surface current coupling switched on (b, f), and thermodynamic coupling switched on but surface current coupling switched off (c, g). Of those cases with thermodynamic coupling switched off, the atmospheric temperature is prescribed and equals the averaged initial air temperature before the wind forcing applied.

In those cases with surface current coupling switched on (Fig. 4.1), the magnitudes of wind stress curl are much greater than those in the cases with surface current coupling switched off. Therefore, a significant portion of wind stress curl contributed by current effect is expect to be revealed. Comparing Figs. 4.1a and 4.1c, the greater wind stress curl over the most part of the

domain represented by a deeper brown color is revealed in Fig. 4.1a, which implies greater wind stress curl are generated in case with thermodynamic coupling switched off. The same phenomenon can be observed in the comparison of Figs. 4.1e and 4.1g. Greater wind stress curl results from the prescribed potential air temperature fields in the cases with thermodynamic coupling deactivated. However, in cases with thermodynamic coupling activated, the potential air temperature can adjust to the evolving SST field. Therefore, larger difference between air temperature and SST in cases with thermodynamic coupling can introduce greater wind stress and wind stress curl values.

Both Figs 4.1a and 4.1c show a long band of positive wind stress curl. Because the two cases only consider the effect of crosswind SST gradients on wind stress curl, strong crosswind SST gradients are expected to generate the positive wind stress curl band. In Figs 4.1b and 4.1d, where the surface current coupling is switched on, the positive wind stress curl band still exists. To further investigate the wind stress curl in a submesoscale front, a local region that contains only one part of the front is selected and focused on. The local region is shown in the black box in Fig. 4.1d.

Fig. 4.1b and 4.1d reveal a strong negative wind stress curl in the eddy area. However, no such negative wind stress curl is detected over the eddy in Figs. 4.1a and 4.1c. To study the wind stress adjustment over the submesoscale eddy, a local region is chosen, shown in the yellow box in Fig. 4.1d. The length and width of the black and yellow boxes are 1 km. The symmetric instability bands in the Exp8W- experiments exhibit submesoscale structures that are different from both the front and the eddy. Finally, to study wind stress field over the symmetric instability band, a local region shown as the white box in Fig. 4.1h is chosen, which is the same size as the other boxes.

In the following subsections of 4.1.1.1, 4.1.1.2, and 4.1.1.3, wind stress curl fields over a submesoscale front, an eddy, and a symmetric instability band are scrutinized separately, to investigate the wind stress adjustments over different features of these submesoscale processes.

4.1.1.1 Wind stress curl over submesoscale front. The wind stress curl fields calculated using the four air-sea schemes for the subdomain in black box are shown in Fig. 4.2. In all cases, large wind stress curls (in magenta) form over the front. Similar to Fig. 4.1, cases with surface current coupling switched on tend to generate greater wind stress curl than those cases with

surface current coupling switched off, and cases with thermodynamic coupling switched on tend to have smaller wind stress curl than those cases with thermodynamic coupling switched off. The negative wind stress curl appearing on the north side (left side) of the front is primarily contributed by current effect, since it is only observed in Figs. 4.2b and 4.2d.

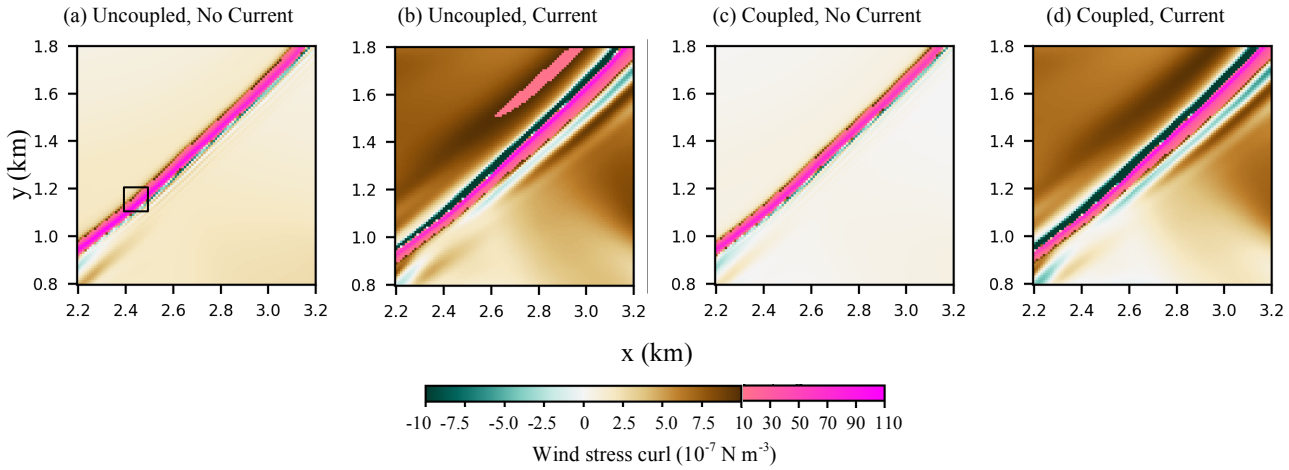

Figure 4.2: Wind stress curl over a subdomain of submesoscale front in Exp4W-CC at the 24th hour. The wind stress are recalculated from model with air-sea schemes with both thermodynamic coupling and surface current coupling switched off (a, e), thermodynamic coupling switched off but surface current coupling switched on (b, f), and thermodynamic coupling switched on but surface current coupling switched off (c, g). The subdomain of the submesoscale front is indicated by the black box in Fig. 4.1d.

Data density and linear regression of wind stress curl in Fig 4.2 as a function of crosswind SST gradient are shown in Figs. 4.3a and 4.3b, and 4.3e and 4.3f respectively. Similar studies have been made using satellite observations and numerical models of mesoscale features (Chelton et al., 2004; Maloney & Chelton, 2006). The coupling coefficient defined by Maloney & Chelton (2006) is used to represent the slope of the linear regression of wind stress curl as a function of crosswind SST gradient. In the results for those cases with surface current coupling switched off (as shown in Figs. 4.3a and 4.3e), a rough linear relationship between wind stress curl and crosswind SST gradient can be recognized. However, the two branches in Figs. 4.3a and 4.3e representing the wind stress curl field are contributed by two categories of crosswind SST gradients with different coupling coefficients. Further diagnosis of the two branches will be discussed in the following paragraphs.

When surface current coupling is switched off, the coupling coefficients for cases with thermodynamic coupling switched on and off are 0.259 and 0.325, respectively. The relatively larger coupling coefficient in the case with thermodynamic coupled switched on is caused by the greater temperature difference between the atmosphere and the ocean surface when the atmospheric temperature is prescribed. Smaller coupling coefficient are detected in this study than were reported by Chelton et al. (2004), which found the coupling coefficients are ranges from 0.57 to 1.17 in Gulf Stream and Southern Ocean. The lack of wind adjustment to the ocean surface in CheapAML could explain its smaller coupling coefficient. In another word, the coupling coefficient in Figs. 4.3b and 4.3f only represent wind stress adjustments to atmosphere temperature and ocean surface temperature. The binned standard deviation represented by the error bars merely represents the differences between the two branches in Figs. 4.3a and 4.3e.

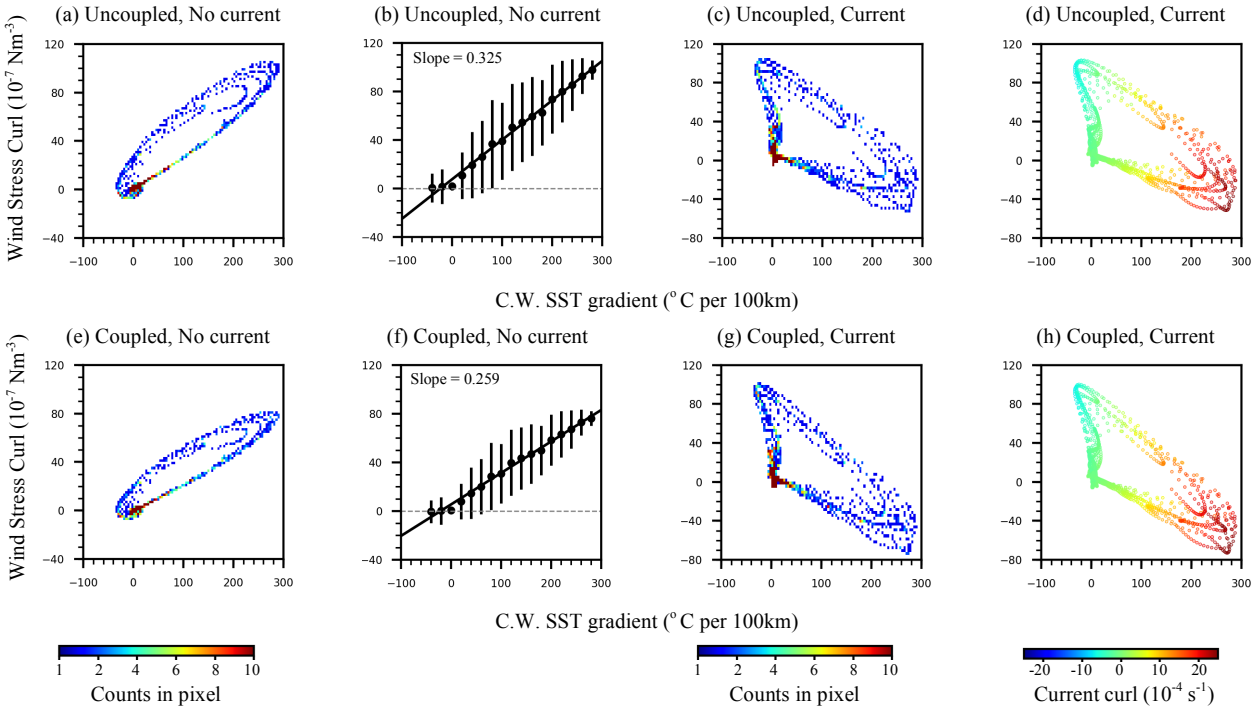

Figure 4.3: Data counts in pixels of wind stress curl and crosswind SST gradient for Fig. 4.2a (a), Fig. 4.2b (c), Fig. 4.2c (e) and Fig. 4.2d (g). Binned mean, binned standard deviation and linear regression of wind stress curl as a function of crosswind SST gradient in (a) and (e) are shown in (b) and (f). Scatter plots of wind stress curl with respect to crosswind SST gradient with color representing surface current curl for Fig. 4.2b (d) and Fig. 4.2d (h).

In those cases with surface current coupling switched on, shown in Figs. 4.3c and 4.3g, the wind stress curl is no longer a positive-slope linear function of crosswind SST gradient. Instead, for the range of large positive crosswind SST gradient of 280^{o} C per 100km, negative wind stress curl values are generated. Switching on the surface current coupling changes the positive correlation between wind stress curl and crosswind SST gradient. Figs. 4.3d and 4.3h plot the wind stress curl as a function of crosswind SST gradient, with the color representing the value of current curl. In both Figs 4.3d and 4.3h, the larger wind stress curl values correspond to colder colors, which implies a negative correlation exists between wind stress curl values and current curl values. Since the wind forcing field is uniform, the current curl will introduce a wind stress curl with an opposite sign when the surface current coupling is switched on.

The positive correlation between crosswind SST gradient and wind stress curl can also be seen in Figs. 4.3d and 4.3h. When wind stress curl equals 40×10^{-7} Nm^{-3}, the data for the left branch are a cool color, which corresponds to a small or negative current curl, while the data for the right branch are a warm color, which represents greater positive current curl. In this study, only crosswind SST gradients and current curls is assumed to be able to generate the wind stress curl. Therefore, the wind stress curl values contributed by positive crosswind SST gradients on the right branch are compensated by negative wind stress curl introduced by the positive current curl. Furthermore, crosswind SST gradients around 280^{o} C per 100km in Fig. 4.3c correspond to negative wind stress curl of smaller magnitude than those in Fig. 4.3g. This may be due to that, in the coupled case with thermodynamic coupling switched off, the negative wind stress curl introduced by current curl has been offset more by the SST gradient effect because the coupling coefficient in case with thermodynamic coupling switched off is greater than the one in case with thermodynamic coupling switched on.

Wind stress curl as a function of current curl in cases with surface current coupling switched are shown in Figs. 4.4a and 4.4c. The color represents the value of the crosswind SST gradient. Clearly, the slope is steeper in the case with thermodynamic coupling switched on. The gentler slope in Fig. 4.4a shows the greater coupling coefficient in the case with thermodynamic coupling deactivated makes the offsetting effect of the crosswind SST gradient on wind stress curl greater. To ascertain the pure relationship between current curl and the wind stress curl contributed by the current curl, and to eliminate the contribution of the crosswind SST gradient, the wind stress curl contributed by the crosswind SST gradient is removed according to the linear

relationship shown in Figs. 4.3b and 4.3f. The data density for current curl and wind stress curl without the contribution of crosswind SST gradients are shown in Figs. 4.4b and 4.4d. The slopes in the two panels are similar, and both show a rough linear relationship between wind stress curl and current curl.

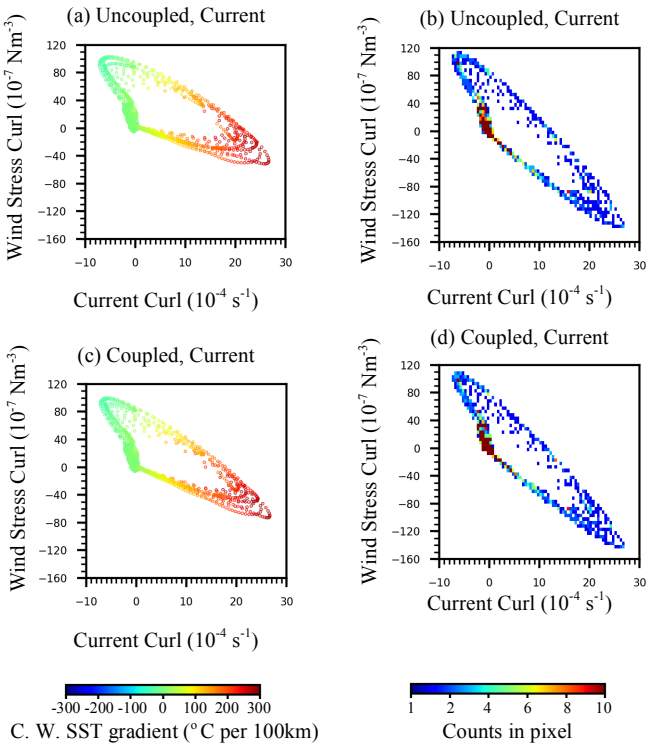

Figure 4.4: Scatter plots of wind stress curl with respect to surface current curl with color representing crosswind SST gradient for Fig. 4.2b (a), and Fig. 4.2d (c). After the deduction of the wind stress curl attributed to crosswind SST gradient according to the regressed linear relationships in Figs. 4.3b and 4.3f, data counts in pixels of wind stress curl and surface current curl for uncoupled, surface current considered case, and coupled, surface current considered case are shown in (c) and (d).

Figs. 4.5a and 4.5b reveal the fields of crosswind SST gradient and current curl for the front subdomain, indicated in the black box in Fig. 4.1d (Data counts in pixels of crosswind SST gradient and current curl are plotted in Fig. 4.5c). Combining the positive correlation between the crosswind SST gradient and wind stress curl shown in Figs. 4.3a and 4.3e, and the negative correlation between current curl and wind stress curl shown in Figs. 4.4b and 4.4d, the positive correlation between crosswind SST gradient and current curl revealed in Fig. 4.5c indicates that the wind stress curl contributed by crosswind SST gradient compensates for the wind stress curl introduced by current curl over the submesoscale front. The negative slopes in Figs. 4.3d and

4.3h, indicate the wind stress curl contributed by current curl are of greater magnitudes than those contributed by crosswind SST gradient.

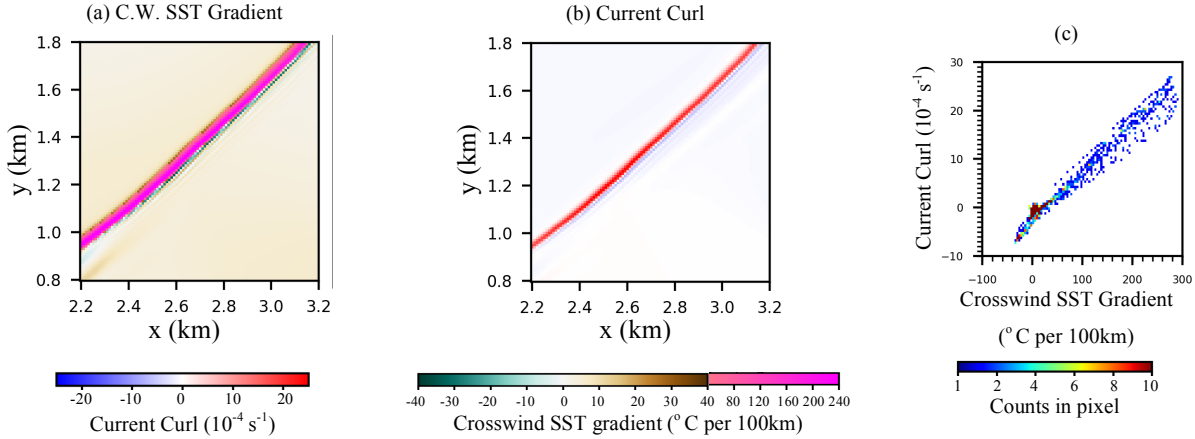

Figure 4.5: Shading contours of crosswind SST gradient and surface current curl over the subdomain of submesoscale front are shown in (a) and (b). Data counts in pixels of them are shown in (c).

In order to determine why two branches of data exist in Figs. 4.3a and 4.3e, a smaller subdomain of the front (Fig. 4.6) is chosen, which is indicated by the black box in Fig. 4.2a. On the right side of the front, there are grids of negative crosswind SST gradient, but it is covered by positive wind stress curl. An example of this phenomenon is shown in the white box in Figs. 4.6a and 4.6b. To ascertain the cause of this phenomenon, the values of SST and zonal wind stress in the three grids shown in the white box are revealed in Figs. 4.6c and 4.6d. As in the case with thermodynamic coupling switched off where the atmospheric potential temperature is prescribed, the cooler SST of the north grid will introduce a larger air-sea temperature difference and yield to a westward (negative) wind stress with greater magnitude than the south grid with warmer SST. The wind stress direction and magnitude are schematically shown as black arrows in Fig. 4.6d. Thus, a positive wind stress curl is formed over a negative crosswind SST gradient. In this local phenomenon, the cooler SST introduces a greater wind stress magnitude as the effect of larger air-sea temperature difference.

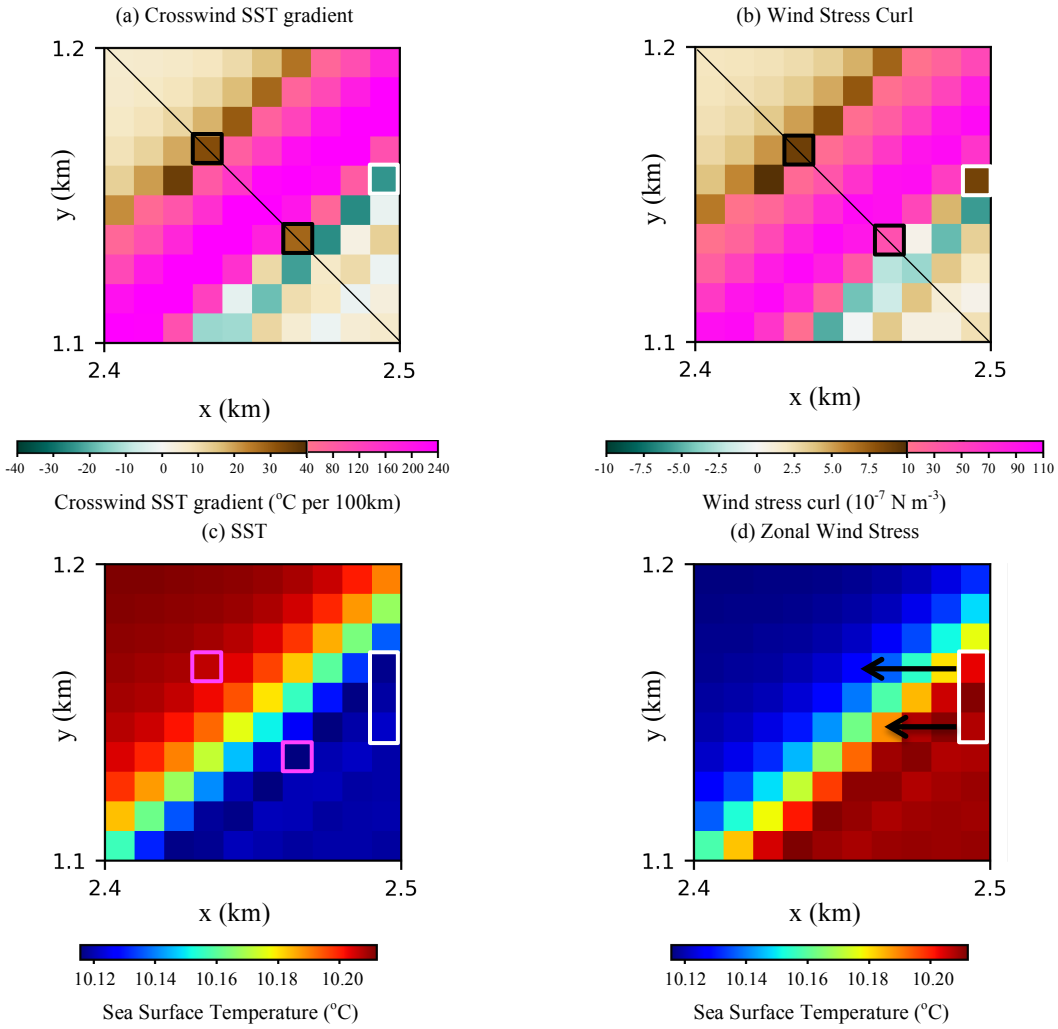

Figure 4.6: Crosswind SST gradient (a), wind stress curl (b), SST (c), and zonal wind stress (d) for the subdomain shown as the black box in Fig. 4.2a.

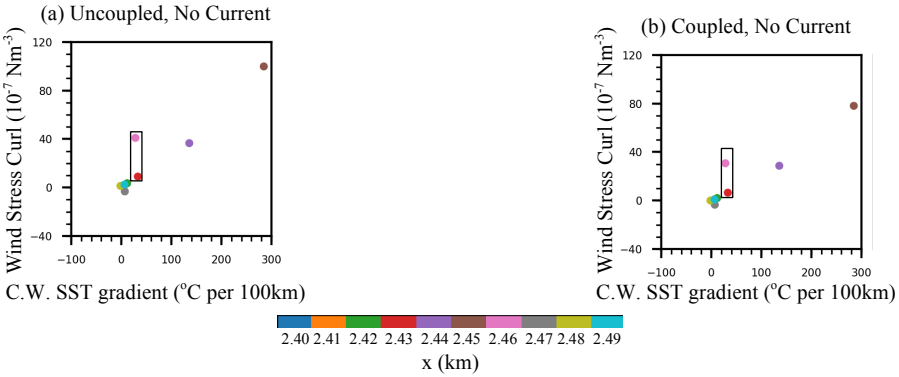

Figure 4.7: Wind stress curl as a function of crosswind SST gradient for data on grids along the black line across the front in Fig. 4.6. Color represents the locations in x-axis. The red point and the magenta point in the black boxes represent data of the grids in the black boxes in Figs. 4.6a and 4.6b. Thermodynamically uncoupled case is represented in the left panel (a), and thermodynamically coupled case is shown in the right panel (b).

However, this local mechanism could not represent the general relationship between SST and wind stress magnitude over the subdomain. Figs. 4.6c and 4.6d show that most of the wind stress of greater magnitudes are over warmer SST areas. This is consistent with the rough positive correlation between crosswind SST gradient and wind stress curl illustrated in Figs 4.3a and 4.3e.

Figs. 4.3a and 4.3e demonstrate that positive wind stress curl can exist over negative crosswind SST. It does not match the positive correlation between crosswind SST gradient and wind stress curl; additionally, the branch separation in the range of positive crosswind SST gradient interrupts the linear relationship between them. To determine how the same crosswind SST gradient can introduce two different wind stress curls, the data of a cross-front line (indicated by a black line in Figs. 4.6a and 4.6b) is analyzed. Fig. 4.7a shows the relationship between wind stress curl and crosswind SST gradient for a case with thermodynamic coupling switched off. The red circle at x = 2.44 and the magenta circle at x = 2.47 show similar crosswind SST gradients, which can be seen in Fig. 4.6a and Fig. 4.7a. However, the magenta circle corresponds to much greater wind stress curl value than the red circle. The SST field in Fig. 4.6c may provide an explanation for the difference in wind stress curl. The smaller wind stress curl (red circle) is located on the warmer side of the front, while the greater wind stress curl (magenta circle) is located on the cooler side of the front. The air-sea temperature difference on the warmer side is smaller than that on the cooler side. Therefore, the greater wind stress curl appears on the cooler side of the front. The same cross-front line is analyzed for the case with thermodynamic coupling switched on and is illustrated in Fig. 4.7b. Similar to the Fig. 4.7a, a greater wind stress curl forms on the cooler side of the front is revealed in Fig. 4.7b. However, the wind stress curl difference between the warmer and cooler sides of the front in Fig. 4.7b is smaller than what is seen in Fig. 4.7a. It is believed that the two-branch structures in Figs. 4.3a and 4.3b may be caused by (i) a large SST variance across the front and (ii) the small-scale sharp crosswind SST gradient adjacent to the cooler side of the front.

To summarize, the wind stress curl over a submesoscale front has a positive correlation with crosswind SST gradients in cases with the surface current coupling switched on. This positive correlation is close to a linear relationship but with two branches caused by SST variance across the front and some small-scale sharp SST gradients adjacent to the front. The coupling coefficient represented by the slope of the linear relationship between wind stress curl

and crosswind SST gradient in the case with thermodynamic coupling switched off is greater than the one in the case with thermodynamic coupling switched on. The smaller air-sea temperature difference in the case with thermodynamic coupling switched on, in which the air temperature can adjust according to the SST, is the reason for its smaller coupling coefficient.

In those cases with surface current coupling switched on, negative correlations between current curl and its production of wind stress curl are revealed. Because there is a positive-slope linear relationship between crosswind SST gradient and current curl in the front domain, the strong negative correlation between current curl and its production of wind stress curl has been compensated by the positive correlation between wind stress curl and crosswind SST gradient. Since the oceanic submesoscale regime is rich in intense current curl, the wind stress curl introduced by current curl is greater than the wind stress curl introduced by the crosswind SST gradient. This is supported by the negative correlations between wind stress curl and crosswind SST gradient seen in Fig. 4.3c and 4.3g. The coupling coefficients between wind stress curl and crosswind SST gradient in cases with thermodynamic coupling switched off is larger than those in cases with thermodynamic coupling switched on.

4.1.1.2 Wind stress curl over submesoscale eddy. To better understand wind stress curl over the submesoscale eddy (in the yellow box in Fig. 4.1d), wind stress curl fields are calculated using the four air-sea schemes in Fig. 4.8. In the two cases with surface current coupling switched on (Figs. 4.8b and 4.8d), the cyclonic eddy introduces a strong negative wind stress curl above it. In the cases with surface current coupling switched off, shown in Figs. 4.8a and 4.8c, wind stress curl fields are much weaker. The consistencies between the wind stress curl fields in Figs. 4.8a and 4.8c and the crosswind SST gradient field in Fig. 4.11a reflect the wind stress curl fields are primarily contributed by the crosswind SST gradient when the surface current coupling is switched off.

Figs. 4.9a and 4.9e show the relationship between wind stress curl and crosswind SST gradient when the surface current coupling is turned off but the thermodynamic coupling is switched off and on, respectively. Good linear relationships are revealed in both cases and a greater coupling coefficient of 0.315 is seen in Fig. 4.9a. The prescribed atmospheric temperature in the case with thermodynamic coupling switched on is higher than the adjustable atmospheric temperature in the coupled case. Therefore, similar to the submesoscale front, the

greater temperature difference between the atmosphere and the ocean surface in the case with thermodynamic coupling switched off makes the coupling coefficient greater than that in the case with thermodynamic coupling switched on. The much smaller standard deviation indicates the better linear relationships between the wind stress curl and the crosswind SST gradient in the submesoscale eddy area. Fig. 4.11a shows no large SST variance in the eddy area. Thus, wind stress curl and crosswind SST gradient are nearly linearly related rather than being separated into two branches, as shown in the submesoscale front area.

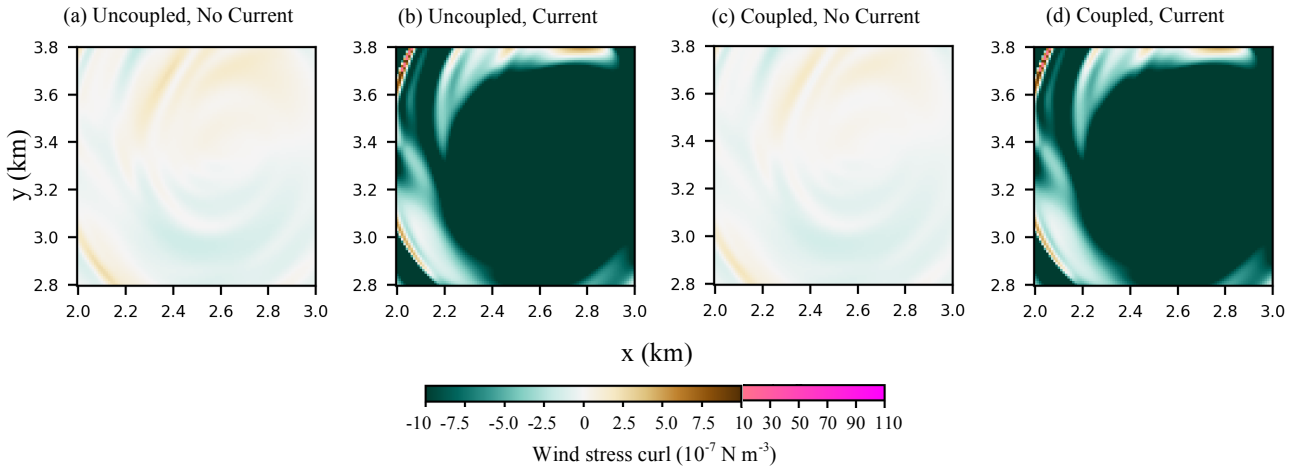

Figure 4.8: Wind stress curl over a subdomain of a submesoscale eddy in Exp4W-CC at the 24th hour. The wind stress are recalculated from model with air-sea schemes with both thermodynamic coupling and surface current coupling switched off (a, e), thermodynamic coupling switched off but surface current coupling switched on (b, f), and thermodynamic coupling switched on but surface current coupling switched off (c, g). The subdomain of the submesoscale eddy is shown as the yellow box in Fig. 4.1d.

When surface current coupling is switched on, the relationships between wind stress curl and crosswind SST gradient are evident (see Figs. 4.9c and 4.9g). Alternatively, no clear correlation between wind stress curl and crosswind SST gradient is evident over the submesoscale eddy. However, in Figs 4.9d and 4.9h, the wind stress curl is positively correlated with the surface current curl. Wind stress curl as a function of surface current curl is plotted for cases with thermodynamic coupling turned off and on in Figs. 4.10a and 4.10c, respectively. Both indicate the wind stress curl is linearly correlated with the surface current curl, and there is no conspicuous difference between the cases with thermodynamic coupling switched on and off. Because the crosswind SST gradients are very weak in the eddy area, the wind stress production

due to crosswind SST gradient is very small (less than $\pm 2\times10^{-7}$ Nm^{-3}) compared to that due to surface current curl (range from 10×10^{-7} Nm^{-3} to -60×10^{-7} Nm^{-3}). When wind stress curl contributed by crosswind SST gradient is removed, no significant difference can be seen when compared to the one prior to deduction (Figs. 4.10b and 4.10d).

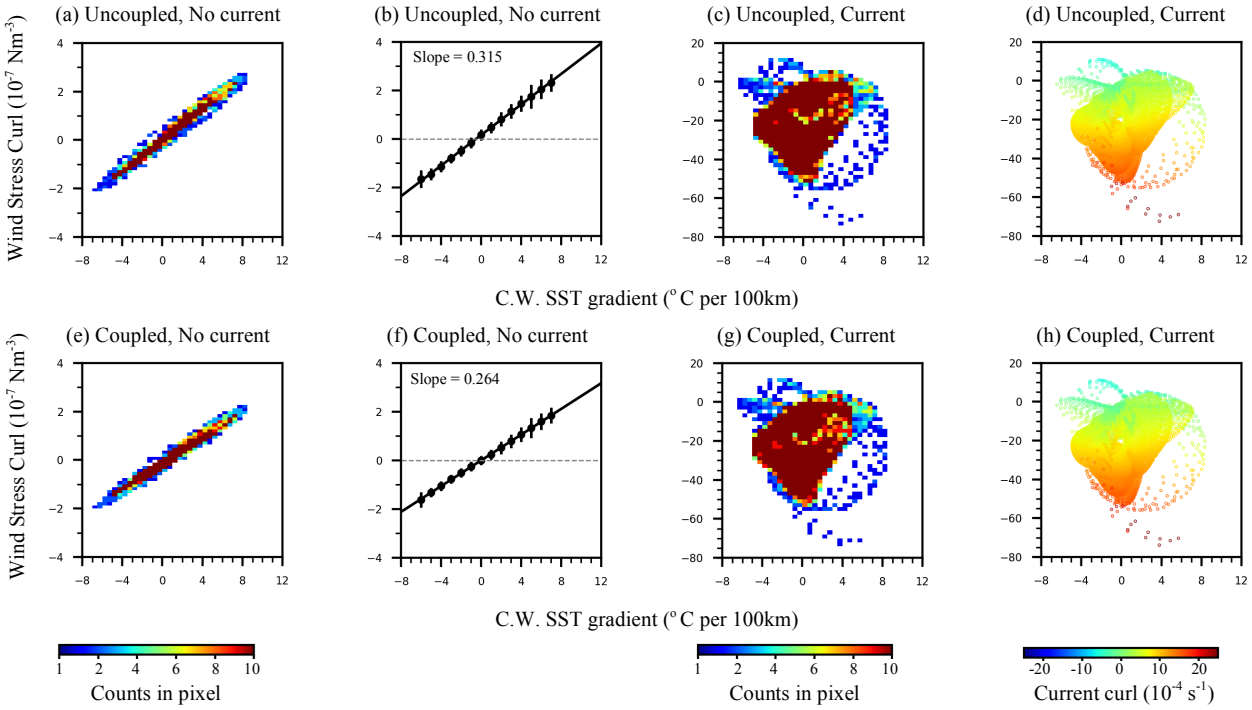

Figure 4.9: Data counts in pixels of wind stress curl and crosswind SST gradient for Fig. 4.8a (a), Fig. 4.8b (c), Fig. 4.8c (e) and Fig. 4.8d (g). Binned mean, binned standard deviation and linear regression of wind stress curl as a function of crosswind SST gradient in (a) and (e) are shown in (b) and (f). Scatter plots of wind stress curl with respect to crosswind SST gradient with color representing surface current curl for Fig. 4.8b (d) and Fig. 4.8d (h).

The crosswind SST gradient and surface current curl fields for the eddy area of interest as well as the data counts in pixels of them are plotted in Fig. 4.11. The positive and negative crosswind SST gradients on the north and south sides of the eddy reveal a cool center of the eddy. Most of the surface current curl field is filled with positive values in the eddy area. Apparently, the current curl field does not match well with the crosswind SST gradient field. This is also seen in Fig. 4.11c, where no linear trend or relationship is recognizable between the current curl and the crosswind SST gradient. This also explains why there is no linear trends or relationships between wind stress curl and crosswind SST gradient in Figs. 4.9c and 4.9g.

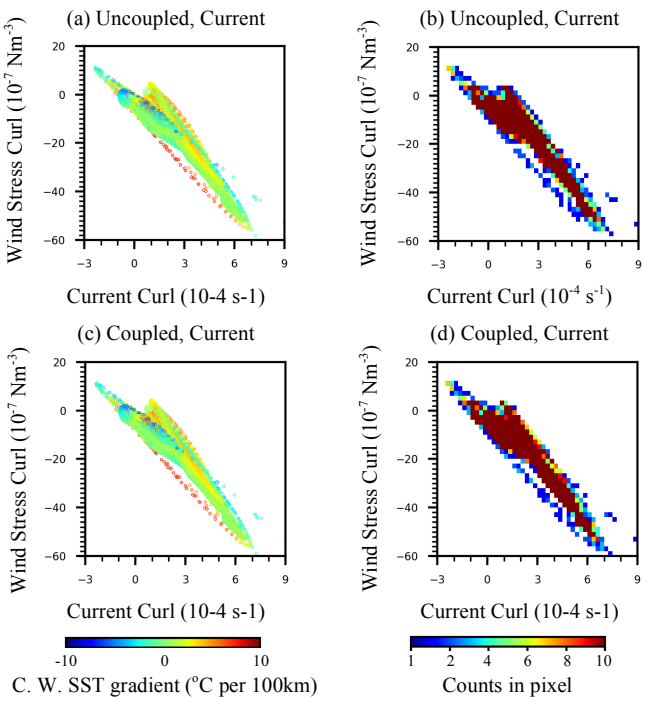

Figure 4.10: Scatter plots of wind stress curl with respect to surface current curl, with color representing crosswind SST gradient for the case with surface current coupling switched on but thermodynamic coupling switched off (a), and the case with both with surface current coupling and thermodynamic coupling switched on(c). After the deduction of the wind stress curl attributed to crosswind SST gradient according to the regressed linear relationships in Figs. 4.9b and 4.9f, data counts in pixels of wind stress curl and surface current curl for the case with surface current coupling switched on but thermodynamic coupling switched off (b), and the case with both with surface current coupling and thermodynamic coupling switched on (d)

Summing the analysis of wind stress curl over submesoscale eddy, the positive linear relationships between wind stress curl and crosswind SST gradient are evident in cases with surface current coupling switched off. However, the magnitudes of crosswind SST gradients are much smaller than those in the submesoscale front discussed in section 4.1.1.1. The greater air-sea temperature difference in the case with thermodynamic coupling switched off makes its coupling coefficient greater than the difference in the case with thermodynamic coupling switched on.

When surface current coupling is active, negative-slope linear relationships between surface current curl and wind stress curl are detected and the wind stress curl over the submesoscale eddy area is mostly introduced by surface current curl. Because the magnitudes of crosswind SST gradients in the eddy are much smaller than those in the submesoscale front, the wind stress curl introduction from crosswind SST gradient is very small compared to the

contribution of surface current curl. Although the positive linear correlation between crosswind SST gradient and its production of wind stress curl still exists in cases with surface current coupling switched on, it cannot compensate nor enhance the negative linear correlation between surface current curl and wind stress curl. This is because the surface current curl is not linearly correlated with crosswind SST gradient in the submesoscale eddy subdomain.

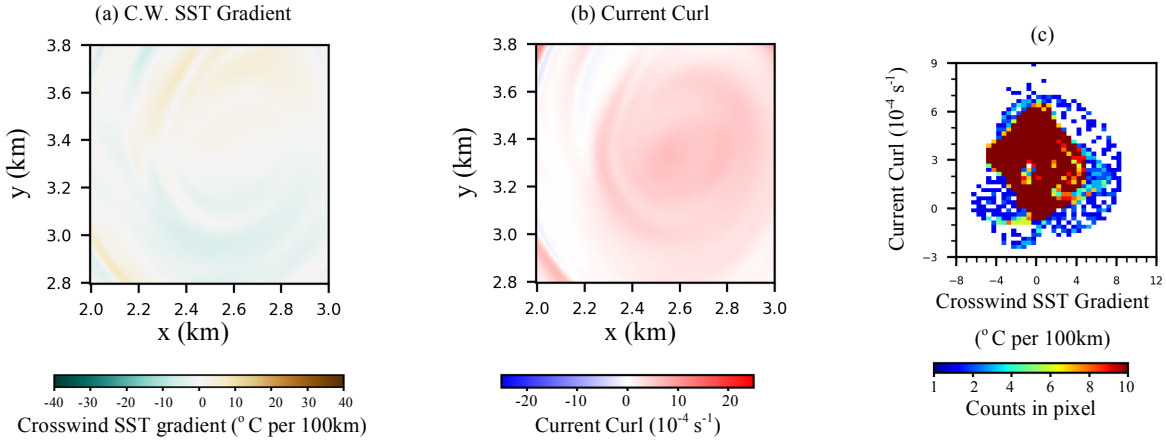

Figure 4.11: Shading contours of crosswind SST gradient and surface current curl over the subdomain of the submesoscale eddy are shown in (a) and (b). Data counts in pixels are shown in (c).

4.1.1.3 Wind stress curl over symmetric instability bands. The previous two sections detail the investigation of wind stress curl fields over a submesoscale front and eddy. The front and eddy are phenomena of baroclinic instability. Symmetric instabilities can take place when the shear of the flow is dominating rather than the stratification (Stamper & Taylor, 2017; Stone, 1966; Thomas et al., 2013; Thomas & Lee, 2005). According to linear theory (Stone, 1966), when the Richardson number is in the range of 0.25 to 0.95, symmetric instability can occur even without external forcing; this is simulated in the preliminary run. Along-current wind forcing can also increase the shear and weaken the stratification through the Ekman transport effect. This could result in a small Richardson number that satisfies the criteria needed to allow for symmetric instability. Leif Thomas (2005) provided a theoretical analysis and a two-dimensional numerical simulation of this. In this study's wind forcing experiments results provided in Chapter 3, symmetric instabilities occur when the along-current wind is 8 ms^{-1} (Fig. 3.6). Under the forcing of 8 ms^{-1} eastward winds, symmetric instabilities can also be seen in Fig. 3.9. At the beginning of the experiments and forced by 8 ms^{-1} eastward winds, the wind is forcing the

surface water to flow eastward. So it takes longer for the symmetric instabilities to fill the whole domain in the eastward wind forcing experiments.

As the wind stress curl fields of Exp8W-CC at the 24th hour show in Fig. 4.1h, the wind stress fields over the ocean field of Exp8W-CC are calculated using the three air-sea schemes used in Figs. 4.1a-c. The results are shown in Figs. 4.1e, 4.1f, and 4.1g, respectively. To maintain the consistency and comparability of the investigations on symmetric instability bands with those on the submesoscale front and eddy, a subdomain with a length and width of 1km is selected to study the wind stress curl over symmetric instability bands. The selected subdomain is shown by the white box in Fig. 4.1h.

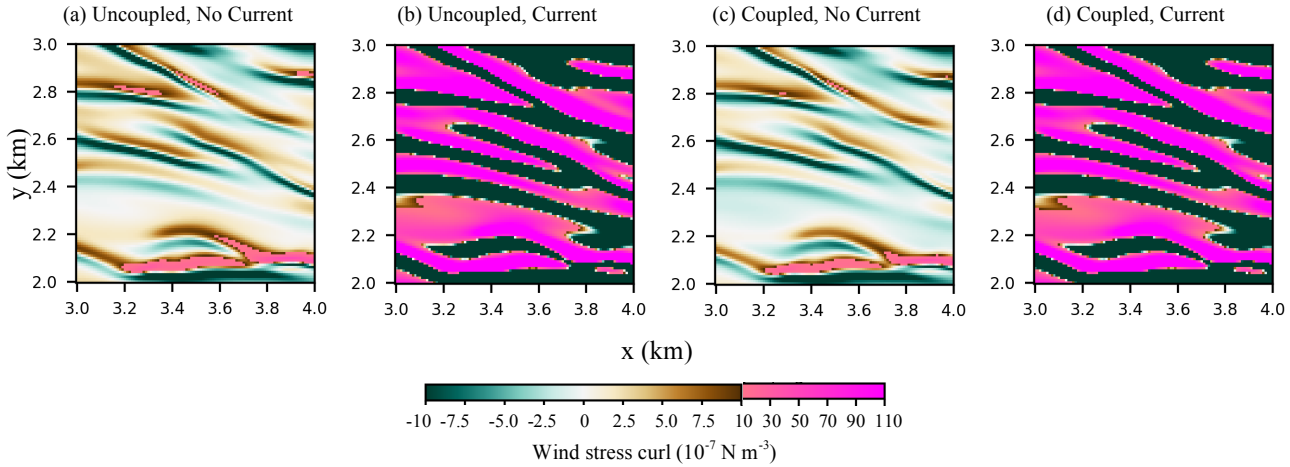

Figure 4.12: Wind stress curl over a subdomain of symmetric instability surface bands in Exp4W-CC at the 24th hour. The wind stress are recalculated from model with air-sea schemes with both thermodynamic coupling and surface current coupling switched off (a, e), thermodynamic coupling switched off but surface current coupling switched on (b, f), and thermodynamic coupling switched on but surface current coupling switched off (c, g). The subdomain filled with submesoscale symmetric instability surface bands is shown as the white box in Fig. 4.1h.

The wind stress curl fields calculated using the four air-sea schemes for the subdomain of symmetric instability bands are shown in Fig. 4.12. Similar to the submesoscale front and eddy, the symmetric instability bands have wind stress curl of greater magnitudes when the surface current coupling is switched on. For the cases with surface current coupling turned off shown in Figs 4.12a and 4.12c, the wind stress curl in the case with thermodynamic coupling switched off is of greater magnitude than those in the case with thermodynamic coupling switched on. Comparing Figs. 4.12a and 4.12b, their patterns of the wind stress fields are consistent with each

other to some degree, as the regions with positive wind stress curl in Fig. 4.12a matches somewhat well with the regions in Fig. 4.12b, having positive but greater wind stress curl. The same consistency can be seen between Figs 4.12c and 4.12d. Slightly bent surface bands of positive and negative wind stress curl appear in all cases.

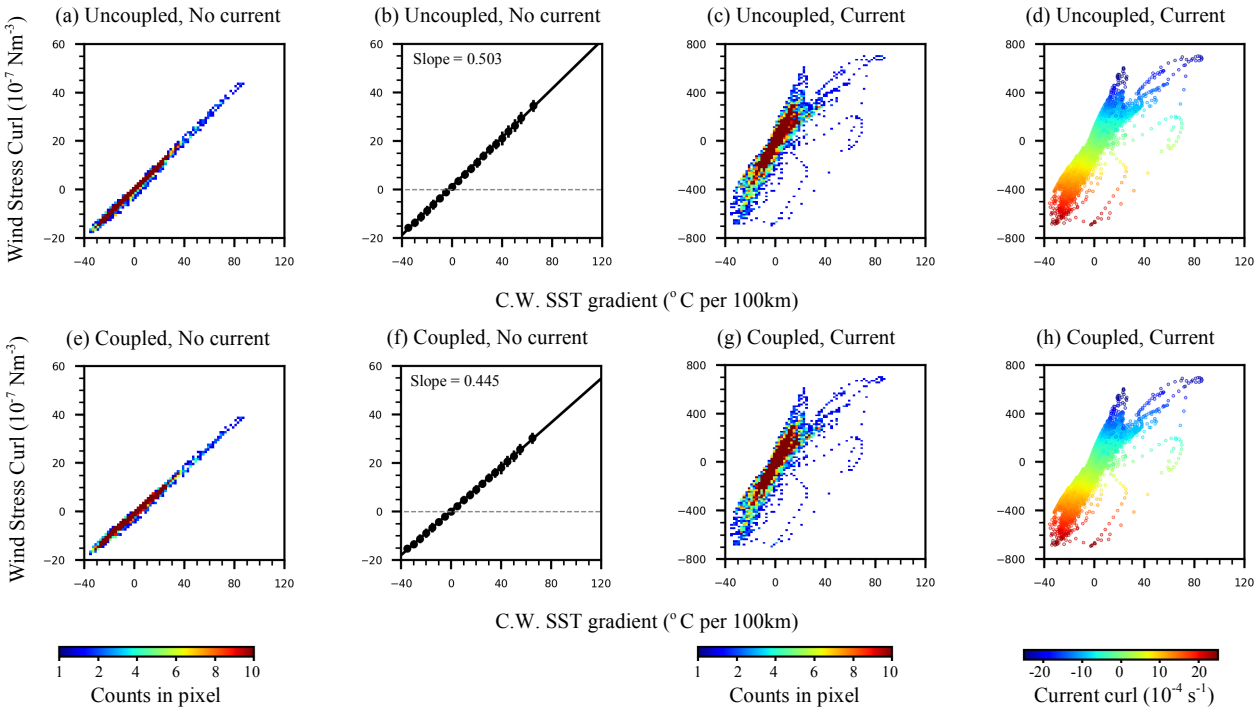

Figure 4.13: Data counts in pixels of wind stress curl and crosswind SST gradient for Fig. 4.2a (a), Fig. 4.12b (c), Fig. 4.12c (e) and Fig. 4.12d (g). Binned mean, binned standard deviation and linear regression of wind stress curl as a function of crosswind SST gradient in (a) and (e) are shown in (b) and (f). Scatter plots of wind stress curl with respect to crosswind SST gradient with color representing surface current curl for Fig. 4.12b (d) and Fig. 4.12d (h).

In Fig. 4.13a, both the thermodynamic coupling and the surface current coupling are switched off, the relationship between wind stress curl and crosswind SST gradient is displayed as a linear function. The slope of 0.503, also known as the coupling coefficients, is slightly greater than in the thermodynamically coupled case, which is 0.445 and shown in Fig. 4.13e. The small standard deviations in Figs. 4.13b and 4.13f show that the wind stress curl is linearly correlated with crosswind SST gradient in cases with surface current coupling is turned off. The magnitude of the crosswind SST gradient in symmetric instability surface bands may be as large as 100^o C per 100 km, which is on the same order as the crosswind SST gradient magnitude in the submesoscale front area. Wind stress curl values ranging from -20×10^{-7} Nm^{-3} to 40×10^{-7} Nm^{-3}

are introduced by crosswind SST gradient in these surface bands; these are much greater than the wind stress curl values introduced in the submesoscale eddy.

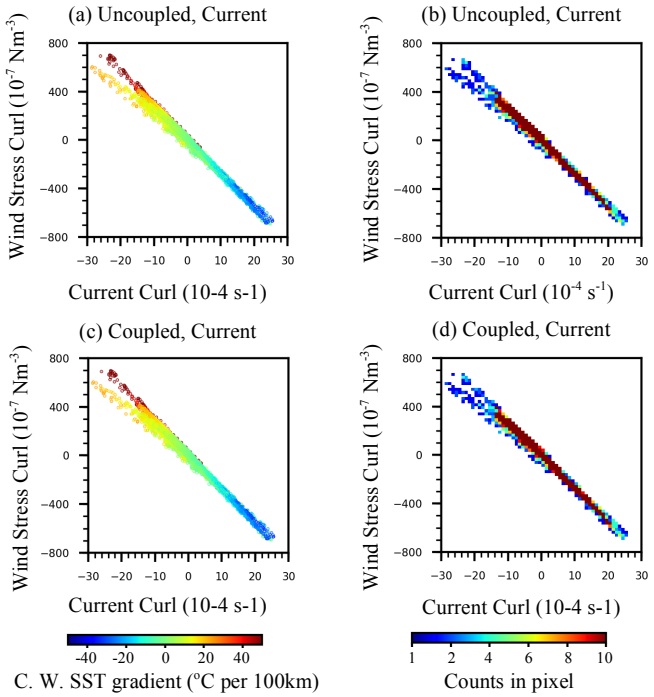

Figure 4.14: Scatter plots of wind stress curl with respect to surface current curl, with color representing crosswind SST gradient for the case with surface current coupling switched on but thermodynamic coupling switched off (a), and the case with both with surface current coupling and thermodynamic coupling switched on(c). After the deduction of the wind stress curl attributed to crosswind SST gradient according to the regressed linear relationships in Figs. 4.13b and 4.13f, data counts in pixels of wind stress curl and surface current curl for the case with surface current coupling switched on but thermodynamic coupling switched off (b), and the case with both with surface current coupling and thermodynamic coupling switched on (d).

For cases with surface current coupling switched on (Figs. 4.13c and 4.13g), the wind stress curl is roughly in a positive linear relationship with the crosswind SST gradient. In Figs. 4.13d and 4.13h, the surface current curl is positively correlated with both crosswind SST gradient and wind stress curl. And the magnitude of wind stress curl can be as large as 700×10^{-7} Nm^{-3}, which is more than 10 times greater than the magnitude of wind stress curl purely introduced by crosswind SST gradient shown in Figs. 4.13a and 4.13e.

A few nonlinear patterns in Figs. 4.13d and 4.13h demonstrate that wind stress curl is not linearly correlated with crosswind SST gradient over some small structures in the area of symmetric instability surface bands.

The relationships between wind stress curl and surface current curl are precisely shown in Figs. 4.14a and 4.14c for cases with thermodynamic coupling switched off and on, respectively. Both reveal that wind stress curl is negatively correlated with surface current curl, and linear relationships are revealed except where the data with surface current curl ranges from -30×10^{-4} s^{-1} to -20×10^{-4} s^{-1}. A branch of data is separated from the linear relationship between wind stress curl and surface current curl, which indicate that over regions of the same negative surface current curl two different groups of wind stress curl are generated. The group with larger crosswind SST gradient corresponds to greater wind stress curl values. When the crosswind SST gradient introduced wind stress curl is removed in Figs. 4.14b and 4.14d, data counts in pixels of wind stress curl and current curl show a linear relationship between them. The two-branch separations shown in Figs. 4.14b and 4.14d are less significant than those shown in Figs. 4.14a and 4.14c. Differences between the thermodynamically uncoupled and coupled cases do not appear to be significant in Fig. 4.14.

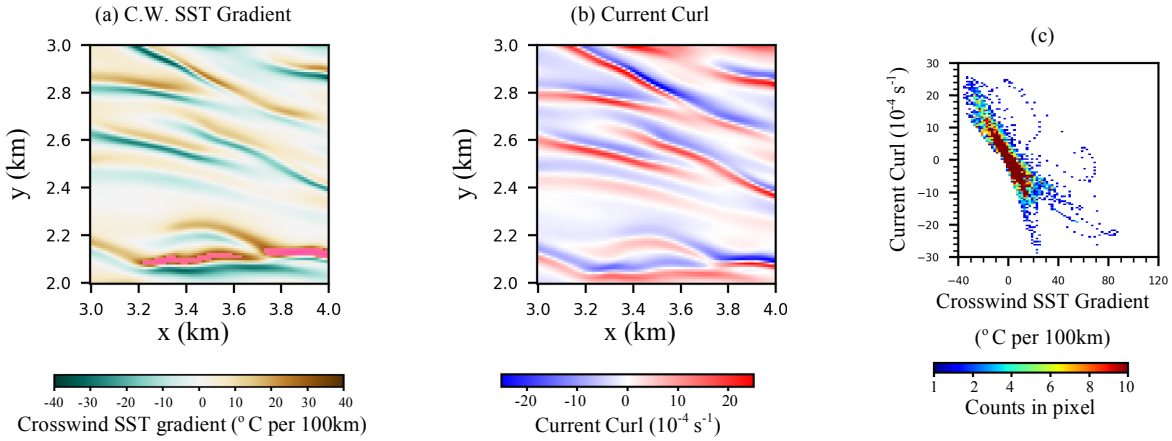

Figure 4.15: Shading contours of crosswind SST gradient and surface current curl over the subdomain of symmetric instability surface bands are shown in (a) and (b). Data counts in pixels are shown in (c).

Fields of crosswind SST gradient and surface current curl in the subdomain of symmetric instability surface bands are shown in Figs. 4.15a and 4.15b. A negative correlation between crosswind SST gradient and surface current curl can be observed, as regions with positive

crosswind SST gradient (brown or magenta regions) in Fig. 4.15a correspond to negative surface current curl (blue regions) in Fig. 4.15b. Surface current curl as a function of crosswind SST gradient is shown in Fig. 4.15c. A rough negative-slope linear relationship is revealed. However, for the data with crosswind SST gradient greater than 40^{o} C per 100km, no linear relationship between crosswind SST gradient and surface current curl is evident. The irregularity between them also explains some of the scatter in Figs. 4.13c and 4.13g. The linear pattern of the deep red pixels in Fig. 4.15c indicates that most of the data with crosswind SST gradient in the range of -20 to 20^{o} C per 100km are in a negative-slope linear relationship with surface current curl.

In conclusion, the wind stress curl over symmetric instability surface bands is positively correlated with crosswind SST gradient when the surface current coupling is switched off. The coupling coefficient in the case with thermodynamic coupling switched off is greater than the one in the thermodynamically coupled case; this is similar to the findings in the studies on front and eddy. However, the magnitude of coupling coefficient for the subdomain of symmetric instability surface bands is significantly greater than those for subdomains of front and eddy. An explanation for this will be discussed in section 4.3, where the relationship of coupling coefficient and wind forcing magnitude is investigated. Since both coupling coefficient and crosswind SST gradients in symmetric instability bands are much greater than those in the submesoscale eddy, stronger wind stress curl fields are generated by crosswind SST gradient over the symmetric instability surface bands.

The strong current curl on the surface of symmetric instability bands primarily produces the wind stress curl when the surface current coupling is switched on. The crosswind SST gradient is positively correlated with wind stress curl, and a negative correlation between surface current curl and wind stress curl becomes valid when surface current coupling is activated. In the subdomain of symmetric instability surface bands, the surface current curl is negatively correlated with the crosswind SST gradient. Therefore, the strong negative correlation between current curl and its production of wind stress curl has been enhanced by the wind stress curl contribution of crosswind SST gradient. This is different from the compensation effect in the subdomain of the submesoscale front discussed in section 4.1.1.1.

4.1.2 Wind Stress Divergence over Submesoscale Structures

To study the wind stress divergence over submesoscale processes, the wind stress fields over the three submesoscale structures of eddy, front, and surface bands of symmetric instability are inverstigated. Figs. 4.16d and 4.16h show the wind stress divergence fields of Exp4W-CC and Exp8W-CC at the 24^{th} hour. Wind stress fields are calculated using the other three air-sea schemes over the ocean field of Exp4W-CC and are shown in Figs. 4.16a, b, and c. The subdomain outlined by the yellow box in Fig. 4.16d is investigated to examine the wind stress divergence over the submesoscale eddy. The black box in Fig. 4.16d represents the subdomain of the submesoscale front, in which the wind stress divergence over the submesoscale front is studied. Figs. 4.16e-g shows wind stress divergence over the ocean field of Exp8W-CC calculated using the three air-sea schemes used in Figs. 4.1a-c. The subdomain designated by the white box in Fig. 4.16h is chosen for the study of wind stress divergence over submesoscale surface bands of symmetric instability.

In Fig. 4.16, when the surface current coupling is switched on, the magnitudes of wind stress divergence are much greater than those in cases with surface current coupling switched off. Thus, the influence of surface current on wind stress divergence in the submesoscale regime should not be neglected. Figs. 4.16b and 4.16d show that small negative wind stress divergence fills most of the domain, with only a few strips of large positive wind stress divergence in the front and the eddy. However, in Figs. 4.16f and 4.16 h, the strips and fingers of larger positive wind stress divergence fills most of the domain. The long bands of large positive wind stress divergence in Figs. 4.16a and 4.16c are merely generated by the downwind SST gradient in the front. When the contributions of surface current coupling are added in Figs. 4.16b and 4.16d, wider strips of positive and negative wind stress divergence of greater magnitudes are generated and adjacent to the front.

To investigate the wind stress divergence fields over different submesoscale structures, the subdomains of the submesoscale front, eddy, and symmetric instability are selected to study how these submesoscale structures influence the wind stress divergence fields.

4.1.2.1 Wind stress divergence over submesoscale front. Fig. 4.17 shows the wind stress divergence fields calculated using the four air-sea schemes for the subdomain of the submesoscale front, as shown in the black box in Fig. 4.16d. The positive wind stress divergence

band (magenta) in cases with surface current coupling switched on is wider than those in cases with surface current coupling turned off. Two narrow bands of negative wind stress divergence form on two sides of the front in those cases with surface current coupling activated. The wind stress divergence difference between cases with thermodynamic coupling switched on and off is much less significant than the difference between cases with surface current coupling switched on and off.

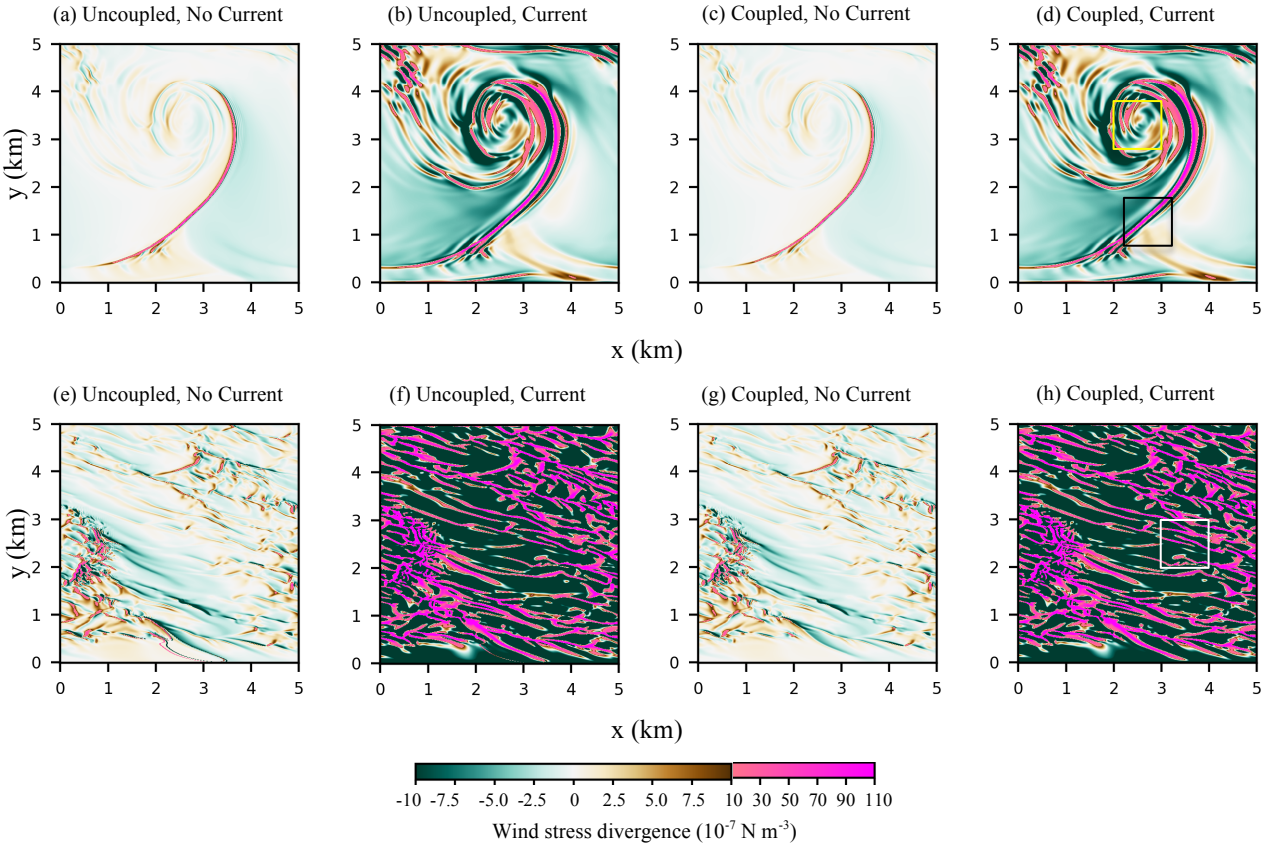

Figure 4.16: Wind stress divergence of Exp4W-CC and Exp8W-CC at the 24th hour (d, h). The wind stress are recalculated from air-sea schemes with both thermodynamic coupling and surface current coupling switched off (a, e), thermodynamic coupling switched off but surface current coupling switched on (b, f), and thermodynamic coupling switched on but surface current coupling switched off (c, g).

When surface current coupling is switched off, data counts in pixels of wind stress divergence and downwind SST gradient for the thermodynamically uncoupled and coupled cases are shown in Figs. 4.18a and 4.18e, and linear regressions are shown in Figs. 4.18b and 4.18f. The coupling coefficients are the same as those illustrated in Figs. 4.3b and 4.3f. When

compared to Figs. 4.3a and 4.3e, similar rough linear relationships are recognized between wind stress divergence and downwind SST gradient in Figs. 4.18a and 4.18e. The large SST variation in the submesoscale front causes the two-branch separation in Figs. 4.18a and 4.18e. The smaller coupling coefficient in Fig. 4.18 results from the smaller air-sea temperature difference due to adjustable atmospheric temperature in the case with thermodynamic coupling switched on.

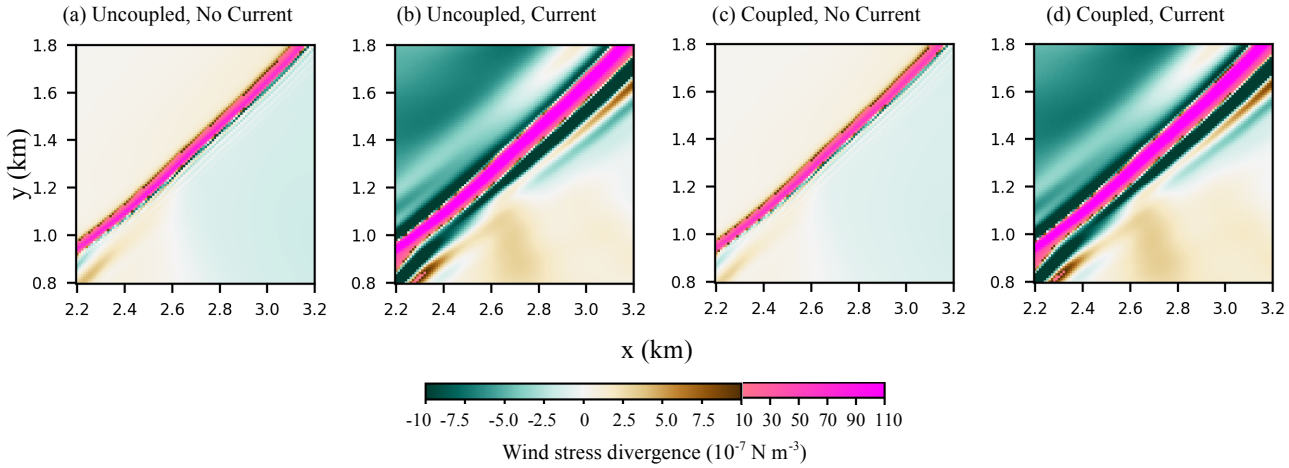

Figure 4.17: Wind stress divergence over a subdomain of the submesoscale front in Exp4W-CC at the 24th hour. The wind stress are recalculated from model with air-sea schemes with both thermodynamic coupling and surface current coupling switched off (a, e), thermodynamic coupling switched off but surface current coupling switched on (b, f), and thermodynamic coupling switched on but surface current coupling switched off (c, g). The subdomain of the submesoscale front is shown in the black box in Fig. 4.16d.

When the surface current coupling is switched on in Figs. 4.18c and 4.18g, the relationship between wind stress divergence and downwind SST gradient are categorized into three patterns. In the range of downwind SST gradients close to zero, the left branch shows wind stress divergence ranging from 0 to 180×10^{-7} Nm^{-3}. The bottom right branch represents a linear relationship between wind stress divergences and downwind SST gradient. The maximum value on the left branch and the one on the right branch are connected by an upper branch. Apparently, activating the surface current coupling changes the relationship between wind stress divergence and downwind SST gradient. In order to determine the influence of surface current, the wind stress divergence as a function of downwind SST gradient are plotted in Figs. 4.18d and 4.18h. Negative correlations between wind stress divergence and surface current divergence are recognizable since greater positive wind stress divergence values are shown in colder colors.

When downwind SST gradient reaches the maximum value, the wind stress divergence in Fig. 4.18d is greater than the in the case with thermodynamic coupling switched on shown in Fig. 4.18h. This may be caused by the greater coupling coefficient between wind stress divergence and downwind SST gradient in the thermodynamically uncoupled case. The relationship between wind stress divergence and surface current divergence in the thermodynamically uncoupled and coupled cases is illustrated in Figs. 4.19a and 4.19c. Significant negative correlations between wind stress divergence and current divergence are recognized for both the thermodynamically uncoupled and coupled cases. Comparing Figs. 4.19a and 4.19c, the wind stress divergences for data with large positive downwind SST gradients (red) in the case with thermodynamic coupling switched off are greater than those in the case with thermodynamic coupling switched on. This indicates that downwind SST divergence could further enhance the negative relationship between wind stress divergence and surface current divergence in thermodynamically uncoupled case.

When the wind stress divergence contributed by downwind SST gradient is removed in Figs. 4.19b and 4.19d, the branch of data with large positive downwind SST gradients is turned to have smaller wind stress divergence values. Thus, the two-branch separation patterns appear in Figs. 4.19b and 4.19d. These patterns might be caused by the simple linear relationships used to remove the effects of downwind SST gradient. It is also supposed that same surface current divergence could introduce different wind stress curl values across a front with a large SST variance. The difference between the cases with thermodynamic coupling switched off and on, shown in Figs. 4.19b and 4.19d respectively, is not remarkable after the remove of wind stress divergence is introduced by downwind SST gradient. Therefore, coupling is not significantly influencing the relationships between wind stress divergence and current divergence in this study.

The downwind SST gradient field in the front subdomain is shown in Fig. 4.20a. Its corresponding field of surface current divergence is shown in Fig. 4.20b. Data counts in pixels of downwind SST gradient and surface current divergence are plotted in Fig. 4.20c to present the relationship between them. In the comparison of Figs. 4.20a and 4.20b, the magenta band of positive downwind SST gradient corresponds to a blue band of negative surface current divergence. This negative correlation is revealed in Fig. 4.20c by the top right branch, showing a negative-slope linear relationship between current divergence and downwind SST gradient. Most

of grids in the domain are of small downwind SST gradient and surface current divergence. They match the deep red pixels close to the origin in Fig. 4.20c. The left branch of the data with current divergence ranging from 0 s^{-1} to -20×10^{-4} s^{-1} is of a small downwind SST gradient. Because the negative linear correlations between wind stress divergence and surface current divergence are revealed in Fig. 4.19, the data pattern in Fig. 4.20c looks like an upside-down version of the patterns seen in Figs. 4.18c and 4.18g.

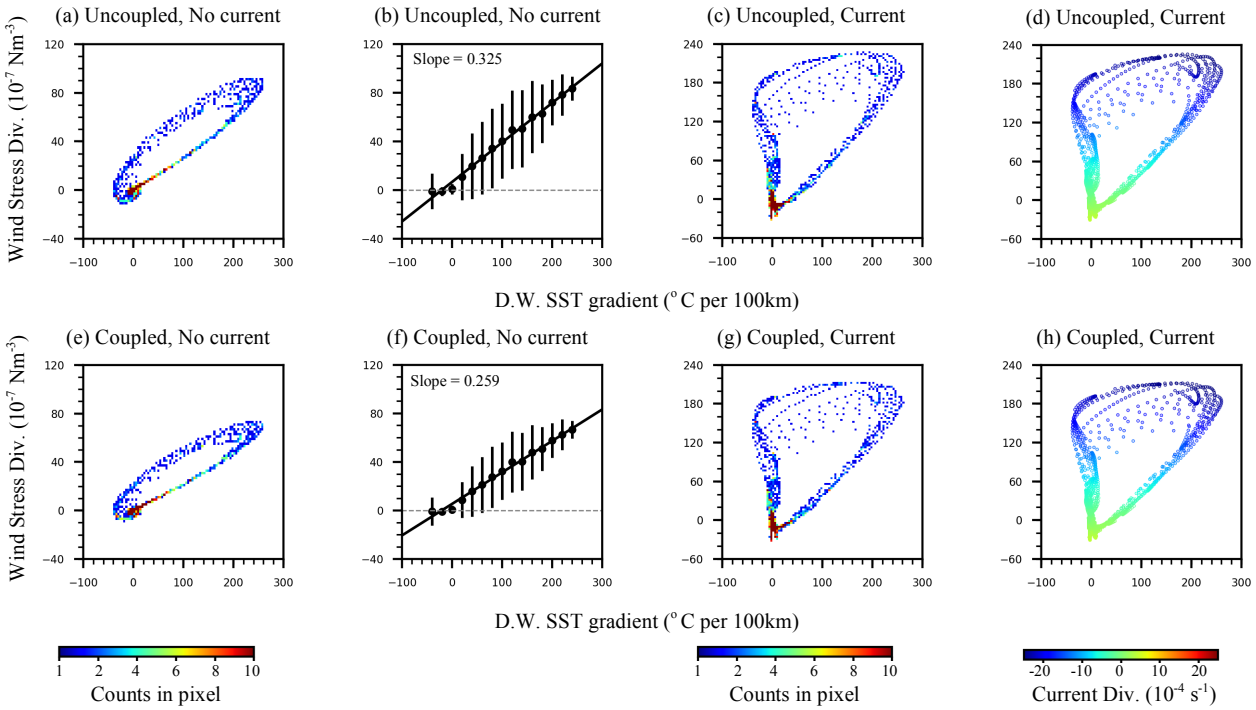

Figure 4.18: Data counts in pixels of wind stress divergence and downwind SST gradient for Fig. 4.17a (a), Fig. 4.17b (c), Fig. 4.17c (e) and Fig. 4.17d (g). Binned mean, binned standard deviation and linear regression of wind stress curl as a function of crosswind SST gradient in (a) and (e) are shown in (b) and (f). Scatter plots of wind stress curl with respect to crosswind SST gradient with color representing surface current curl for Fig. 4.17b (d) and Fig. 4.17d (h). All plots are for the submesoscale front subdomain shown in the black box in Fig. 4.16d.

To determine the locations of the data in these branches in the submesoscale front subdomain, a small domain indicated by the black box in Fig. 4.20a is studied. Downwind SST gradient and surface current divergence for the square domain are shown in Figs. 4.21a and 4.21b. The area of the square domain is 100 m^2 and 100 grids are included, with each grid 10 m in length and 10 m in width.

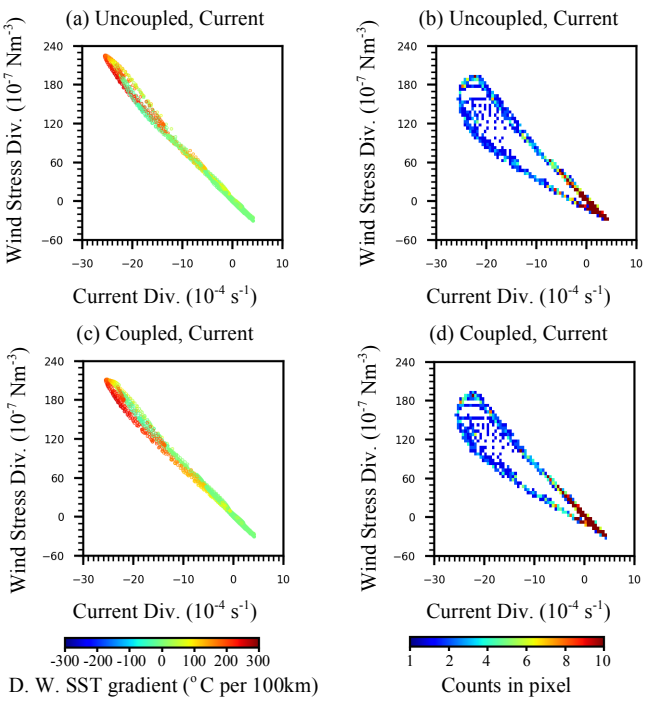

Figure 4.19: Scatter plots of wind stress divergence with respect to surface current divergence, with color representing downwind SST gradient for the case with surface current coupling switched on but thermodynamic coupling switched off (a), and the case with both with surface current coupling and thermodynamic coupling switched on (c). After the deduction of the wind stress divergence attributed to downwind SST gradient according to the regressed linear relationships in Figs. 4.18b and 4.18f, data counts in pixels of wind stress divergence and surface current divergence for the case with surface current coupling switched on but thermodynamic coupling switched off (b), and the case with both with surface current coupling and thermodynamic coupling switched on (d).

A comparison of the fields in Figs. 4.21a and 4.21b reveals the positive downwind SST gradients on the left side of the front correspond to negative surface current divergences. However, on the right side of the front, some grids with negative surface current divergences are of zero or negative downwind SST gradients. Fig. 4.21c shows surface current divergence as a function of downwind SST gradient for ten grids at the diagonal line across the front, indicated by the black line in Fig. 4.21a. Locations on the x-axis are represented by colors. From the top left grid to the bottom right grid, the first six grids have a negative-slope linear relationship between surface current divergence and downwind SST gradient, but the last four grids show an increase of surface current divergence while downwind SST gradient maintains a smaller value close to zero. Data along the diagonal reveal a negative linear correlation between downwind SST gradient and surface current divergence on the left side, or downwind side, of the front. The

vertical branch shown in Figs. 4.20c and 4.21c is expected to locate on the right side, or the upwind side, of the front. The data connecting the minimum values of the two branches is expected to locate at the transition zone between the two sides of the front, where the downwind SST gradients have not yet dropped to close to zero. One example is the grid shown in the black box in Figs. 4.21a and 4.21b, the downwind SST gradient is decreased to smaller than its upper left neighbor, but it still is much greater than zero.

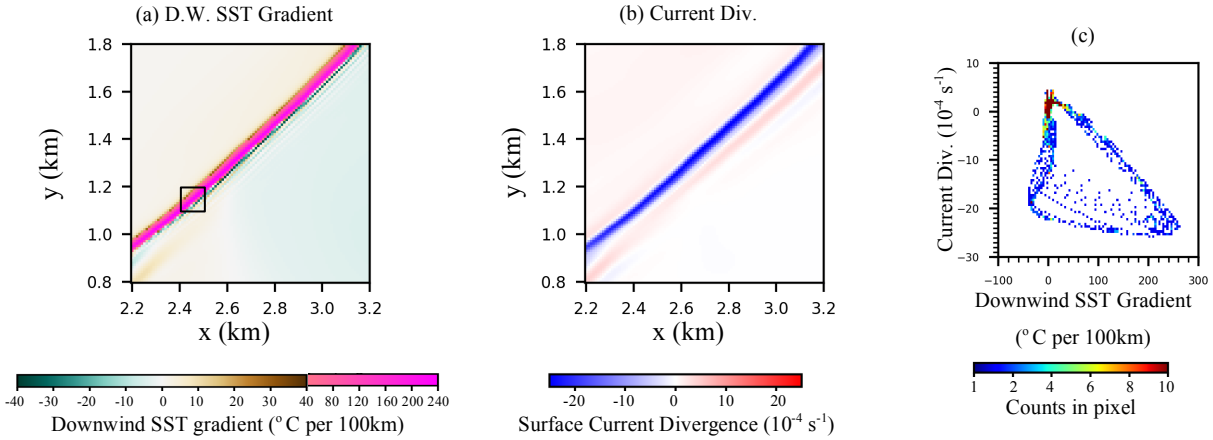

Figure 4.20: Shading contours of downwind SST gradient and surface current divergence over the subdomain of submesoscale front are shown in (a) and (b). Data counts in pixels are shown in (c).

In summary, when the surface current coupling is switched off, there is a positive correlation between wind stress divergence and downwind SST gradient over the submesoscale front. The positive correlation is roughly close to a linear relationship, however the SST variance across the front makes the linear relationship separate into two branches. In both the thermodynamically uncoupled and coupled cases, the slopes of the linear relationships between wind stress divergence and downwind SST gradient are of the same value as those of the linear relationship between wind stress curl and crosswind SST gradient. The gentle slope in the case with thermodynamic coupling switched on is caused by the smaller air-sea temperature difference resulting from the atmospheric temperature adjustment to SST.

When surface current coupling is switched on, wind stress divergence is mainly introduced by surface current divergence. Therefore, the relationship between wind stress divergence and downwind SST gradient is dominated by the relationship between surface current divergence and the downwind SST gradient. In the downwind side of the front, current

divergence has a linear relationship with downwind SST gradient. The negative correlation between wind stress divergence and surface current divergence is enhanced by the downwind SST gradient. However, in the upwind side of the front, downwind SST gradients are close to zero; thus, the negative relationship between surface current divergence and wind stress divergence is not influenced much by the downwind SST gradients.

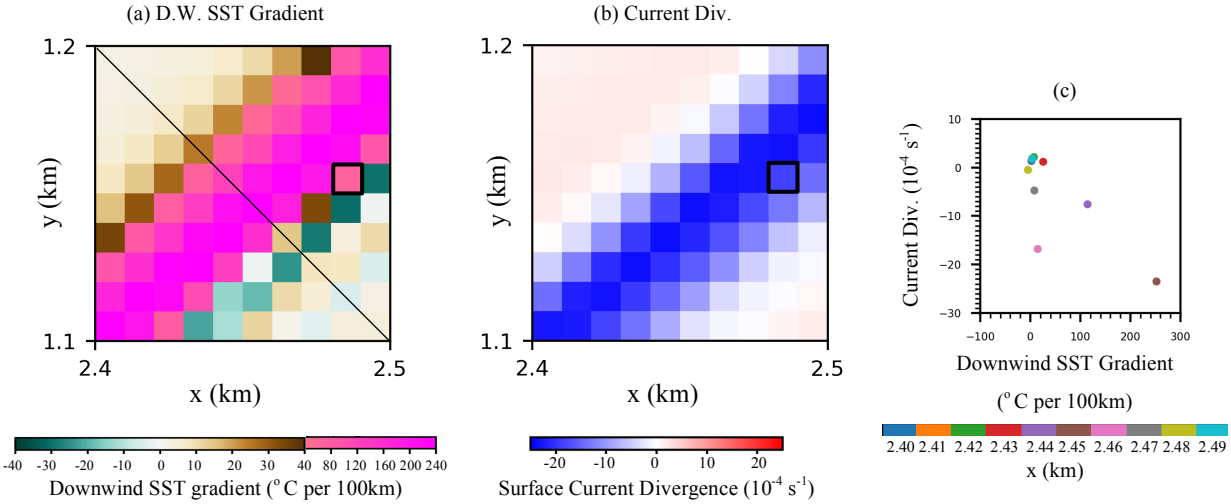

Figure 4.21: Downwind SST gradient (a) and surface current divergence (b) of the subdomain in the black box in Fig. 4.20 (a). In (c), surface current divergence is shown as a function of downwind SST gradient for the data on grids along the black line across the front in (a). Colors represent locations in x-axis.

4.1.2.2 Wind stress divergence over submesoscale eddy. The wind stress divergence fields calculated using the four air-sea schemes for the subdomain of the eddy are shown in Fig. 4.22. Magnitudes of wind stress divergence fields in cases with surface current coupling switched on are greater than those in cases with surface current coupling switched off. Unlike the field of wind stress curl, the wind stress divergence field over the submesoscale eddy contains both positive and negative bands. Magenta bands with large positive values of wind stress divergence can be seen on the downwind side of the eddy.

Figs. 4.23b and 4.23f show the linear regressions of wind stress divergence and downwind SST gradient in the cases with surface current coupling turned off but thermodynamic coupling is switched off and on, respectively. Their data counts in pixels are revealed in Figs. 4.23a and 4.23e. Similar to the relationships between wind stress curl and crosswind SST gradient over the submesoscale eddy, the slope of the linear regression of wind stress divergence

as a function of downwind SST gradient in the thermodynamically uncoupled case is greater than that in the coupled case. The larger air-sea temperature difference in the uncoupled case is considered to be the reason for its greater slope. Comparing Fig. 4.23a and Fig. 4.9a reveals the magnitudes of downwind SST gradients are greater than the magnitudes of crosswind SST gradients. In addition, coupling coefficients in Figs. 4.23b and 4.9b are not much different. Thus, wind stress divergences introduced by downwind SST gradients are greater than the values of wind stress curl introduced by crosswind SST gradients over the submesoscale eddy. Similar results can be concluded by comparing Figs. 4.23e and 4.23f to Figs. 4.9e and 4.9f for the cases with thermodynamic coupling activated, except for the coupling coefficients in them are smaller.

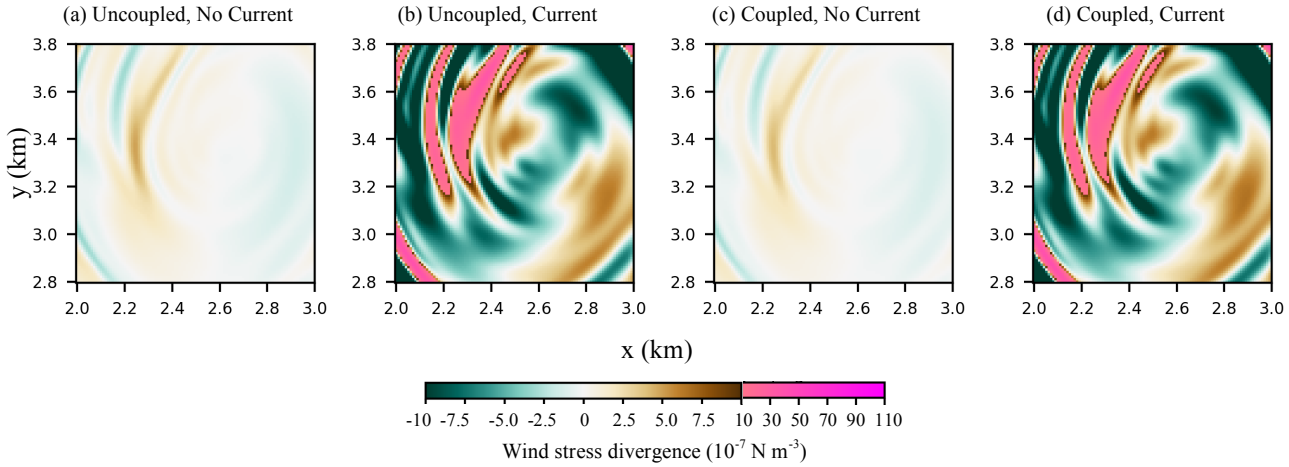

Figure 4.22: Wind stress divergence over a subdomain of submesoscale eddy in Exp4W-CC at the 24th hour. The wind stress are recalculated from model with air-sea schemes with both thermodynamic coupling and surface current coupling switched off (a, e), thermodynamic coupling switched off but surface current coupling switched on (b, f), and thermodynamic coupling switched on but surface current coupling switched off (c, g). The subdomain of the submesoscale front is shown as the yellow box in Fig. 4.16d.

Figs. 4.23c, 4.23d, 4.23g, and 4.23h demonstrate the relationship between wind stress divergence and downwind SST gradient for those cases with surface current coupling switched on. It can be seen that the difference between the thermodynamically uncoupled and coupled cases are not significant and no linear relationship between wind stress divergence and downwind SST gradient is recognized. From the color in Figs. 4.23d and 4.23h, which represents surface current divergence, a negative correlation is also revealed between wind stress divergence and downwind SST gradient. The wind stress divergence magnitudes in cases with

surface current coupling turned on are about 10 times greater than those in cases with surface current coupling switched off. This implies that the current divergence field at the surface primarily introduces the wind stress divergence field.

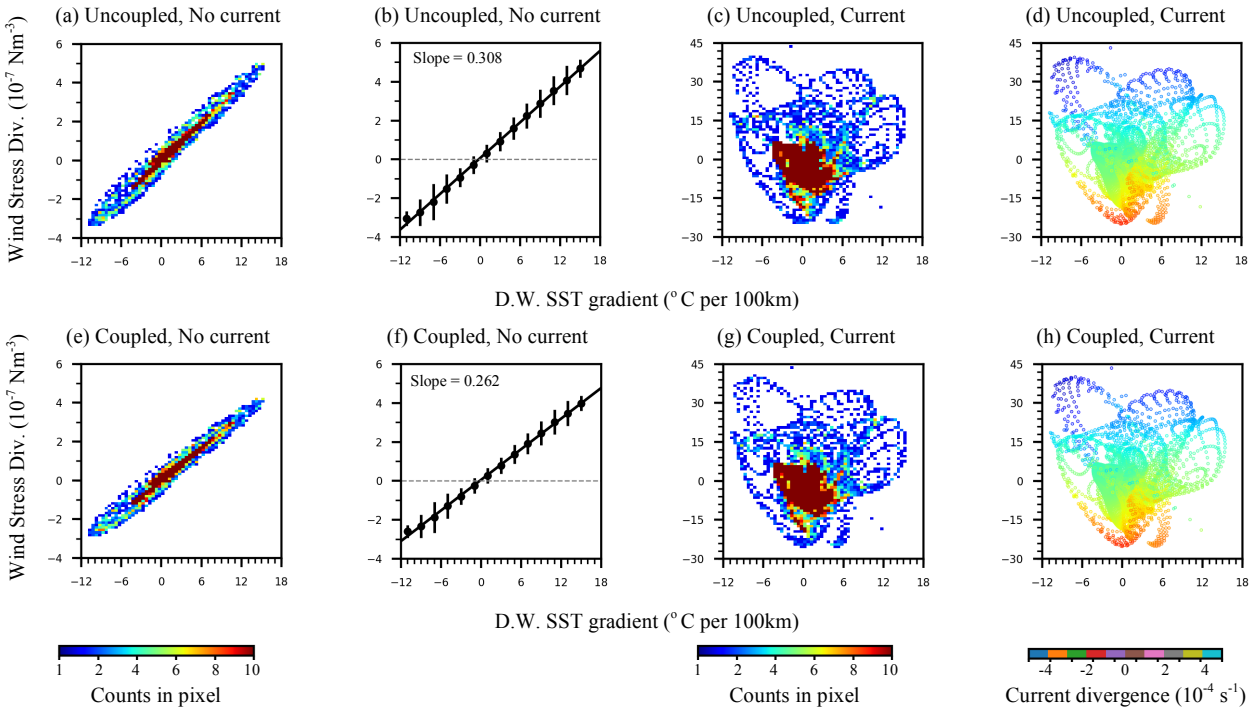

Figure 4.23: Data counts in pixels of wind stress divergence and downwind SST gradient for Fig. 4.22a (a), Fig. 4.22b (c), Fig. 4.22c (e) and Fig. 4.22d (g). Binned mean, binned standard deviation and linear regression of wind stress divergence as a function of downwind SST gradient in (a) and (e) are shown in (b) and (f). Scatter plots of wind stress divergence with respect to downwind SST gradient with color representing surface current divergence for Fig. 4.22b (d) and Fig. 4.22d (h).

Wind stress divergence as a function of current divergence over the submesoscale eddy for cases with thermodynamic coupling switched off and on are shown in Figs. 4.24a and 4.24c respectively. No significant difference between the thermodynamically uncoupled and coupled cases is recognized. Values of wind stress divergence are negatively correlated with surface current divergence values. Colors represent downwind SST gradients. Data with different downwind SST gradients (colors) correspond to different wind stress divergences when surface current divergences are of the same value. However, data with higher values of downwind SST gradient do not always correspond to greater values of wind stress divergence. When the wind stress divergence contributed by downwind SST gradient is removed according to the linear

relationships in Figs. 4.23b and 4.23f, the data counts in pixels of wind stress divergence and surface current divergence for the thermodynamically uncoupled and coupled cases are shown in Figs. 4.24b and 4.24d. Apparently, the relationship between wind stress divergence and surface current divergence for data with large downwind SST gradient magnitudes (red and blue data in Figs. 4.24a and 4.24c) has been adjusted. The imperfect linear relationship with several branches implies that other factors, such as SST and air-sea temperature differences, are also influencing the correlation between wind stress divergence and surface current divergence.

Fields of downwind SST gradient and surface current divergence over the eddy subdomain are plotted in Figs. 4.25a and 4.25b. Comparing Fig. 4.25 and Fig. 4.22, a consistency between downwind SST gradient and wind stress divergence is revealed when the surface current coupling is switched off. In addition, the consistency between surface current divergence and wind stress divergence exists when the surface current coupling is switched. However, the relationship between downwind SST gradient and surface current divergence revealed in Fig. 4.25c, the data counts in pixels of them, is not a linear pattern at all. Thus, when the surface current coupling is activated the eddy subdomain, the wind stress divergence is mainly contributed by surface current divergence field. Although the downwind SST gradient could introduce wind stress divergence, its influence is much smaller and it does not have a clear enhancing or compensating effect on the wind stress divergence produced by surface current.

4.1.2.3 Wind stress divergence over surface bands of symmetric instability. When symmetric instability is generated by the westward wind forcing in Exp8W-CC, wind stress divergence fields for the subdomain indicted by a white box in Fig. 4.1h are calculated using the four air-sea schemes and plotted in Fig. 4.26. Similar to wind stress divergence and curl fields in subdomains of the submesoscale front and eddy, the wind stress divergence in cases with surface current coupling is switched off is of much smaller magnitude than those in the cases with surface current coupling is switched on. Differences between the cases with thermodynamic coupling switched on and off are not significant, as shown in Fig. 4.26.

Figs. 4.27a and 4.27e illustrate data counts in pixels of wind stress divergence and downwind SST gradient in cases with surface current coupling is deactivated but the thermodynamic coupling is switched off and on, respectively. Good linear relationships are revealed in these figures.

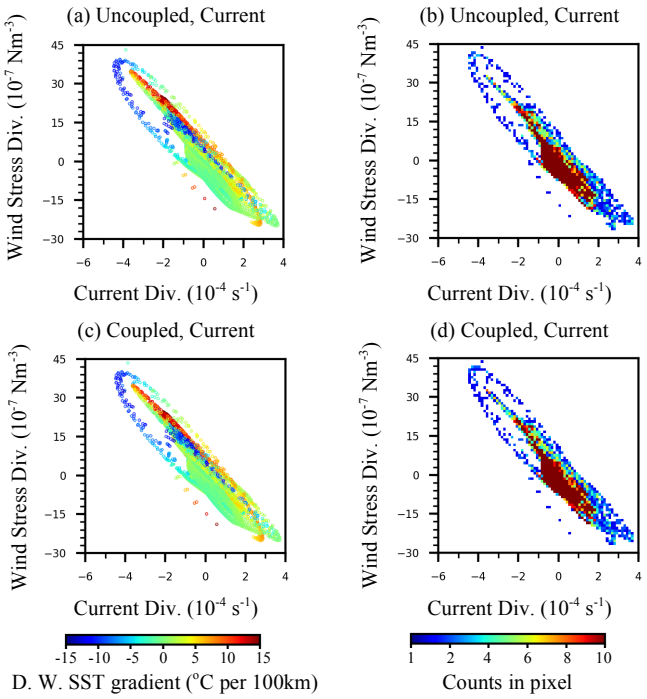

Figure 4.24: Scatter plots of wind stress divergence with respect to surface current divergence, with color representing downwind SST gradient for the case with surface current coupling switched on but thermodynamic coupling switched off (a), and the case with both with surface current coupling and thermodynamic coupling switched on(c). After the deduction of the wind stress divergence attributed to downwind SST gradient according to the regressed linear relationships in Figs. 4.23b and 4.23f, data counts in pixels of wind stress divergence and surface current divergence for the case with surface current coupling switched on but thermodynamic coupling switched off (b), and the case with both with surface current coupling and thermodynamic coupling switched on (d).

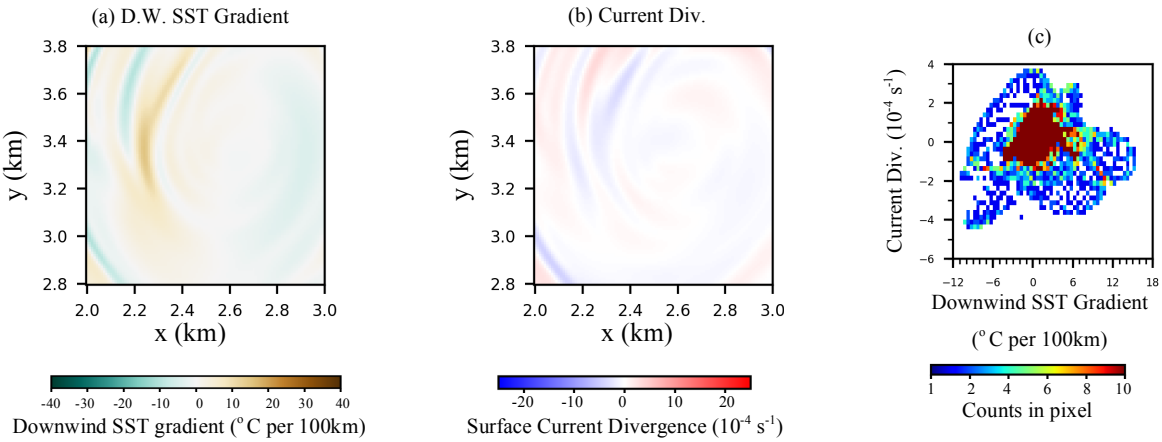

Figure 4.25: Shading contours of downwind SST gradient and surface current divergence over the subdomain of submesoscale eddy are shown in (a) and (b). Data counts in pixels of them are shown in (c).

Linear regressions between wind stress divergence and downwind SST gradient for the thermodynamically uncoupled and coupled cases are shown in Figs. 4.27b and 4.27f, displaying coupling coefficients that are 0.482 and 0.444. These are close to the coupling coefficients shown in Figs. 4.13b and 4.13f for relationships between wind stress curl and crosswind SST gradient. The magnitudes of downwind SST gradient and wind stress divergence are smaller than the magnitudes of crosswind SST gradient and wind stress curl over the subdomain of symmetric instability bands.

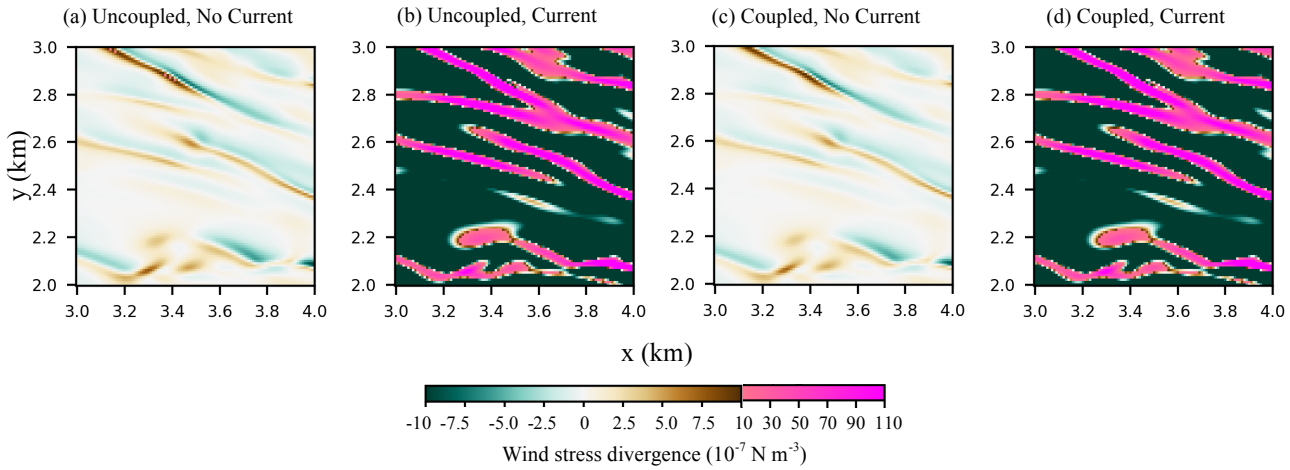

Figure 4.26: Wind stress divergence over a subdomain of symmetric instability surface bands in Exp8W-CC at the 24th hour. The wind stress are recalculated from model with air-sea schemes with both thermodynamic coupling and surface current coupling switched off (a, e), thermodynamic coupling switched off but surface current coupling switched on (b, f), and thermodynamic coupling switched on but surface current coupling switched off (c, g). The subdomain of the symmetric instability surface bands is indicated by the white box in Fig. 4.16h.

When surface current coupling is activated, relationships between wind stress divergence and downwind SST gradient are revealed as seen in Figs. 4.27c, 4.27d, 4.27g, and 4.27h. The magnitudes of wind stress divergence are about 20 times greater than those in cases with surface current coupling switched off. Wind stress divergence as a function of downwind SST gradient for the thermodynamically uncoupled and coupled cases is shown in Figs. 4.27d and 4.27h. Along each vertical line of specific value of downwind SST gradient in Figs. 4.27d and 4.27h, wind stress divergence is negatively correlated with surface current divergence represented by color. However, for data with the same values of surface current divergence, shown as the data with the same color in Figs. 4.27d and 4.27h, wind stress divergence is positively correlated with

downwind SST gradient and the slope of each color band is much greater than the slopes seen in Figs. 4.27b and 4.27f. Large positive slopes of these color bands imply significant positive correlations between wind stress divergence and downwind SST gradient also exist when the surface current coupling is activated.

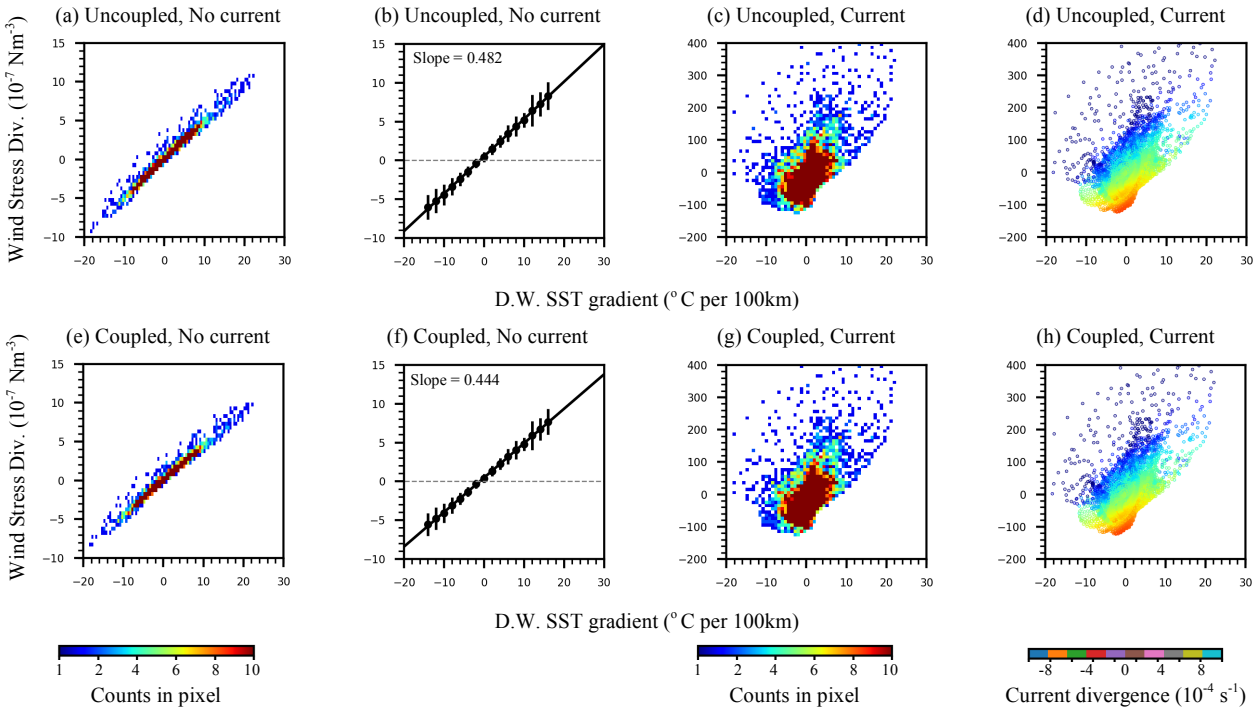

Figure 4.27: Data counts in pixels of wind stress divergence and downwind SST gradient for Fig. 4.26a (a), Fig. 4.26b (c), Fig. 4.26c (e) and Fig. 4.26d (g). Binned mean, binned standard deviation and linear regression of wind stress divergence as a function of downwind SST gradient in (a) and (e) are shown in (b) and (f). Scatter plots of wind stress divergence with respect to downwind SST gradient with color representing surface current divergence for Fig. 4.26b (d) and Fig. 4.26d (h).

Wind stress divergence as a function of surface current divergence, with color representing downwind SST gradient, is plotted in Figs. 4.28a and 4.28c for cases with thermodynamic coupling switched off and on, respectively. Negative correlations between wind stress divergence and surface current divergence can be seen. Furthermore, the large positive downwind SST gradients (indicated in red) tend to have a steeper slope in Figs. 4.28a and 4.28c than the negative downwind SST gradients (indicated in blue). It seems that downwind SST gradients significantly affect the slope of the linear relationship between wind stress divergence and surface current divergence. If wind stress divergence contributions of downwind SST is

simply removed according to the relationships in Figs. 4.27 (b) and (f), the data counts in pixels of wind stress divergence and surface current divergence shown in Figs. 4.28b and 4.28d still show scattered patterns similar to those in Figs. 4.28a and 4.28c.

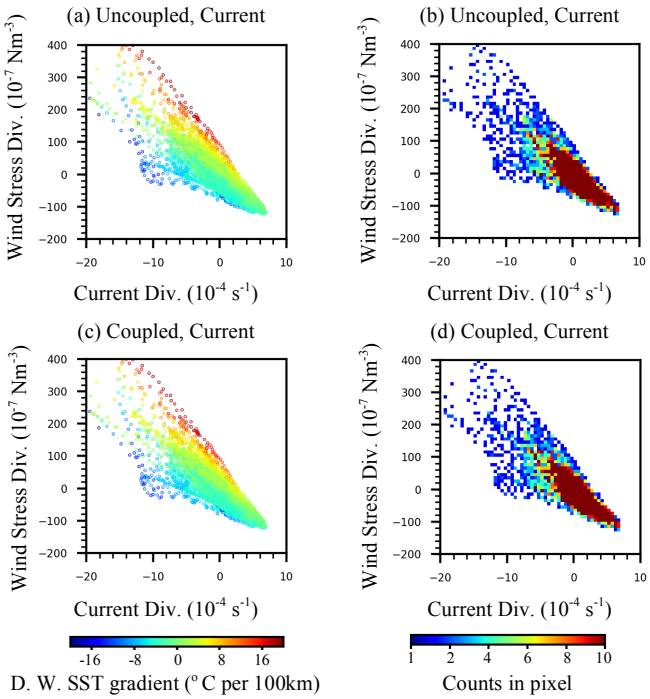

Figure 4.28: Scatter plots of wind stress divergence with respect to surface current divergence, with color representing downwind SST gradient for the case with surface current coupling switched on but thermodynamic coupling switched off (a), and the case with both with surface current coupling and thermodynamic coupling switched on(c). After the deduction of the wind stress divergence attributed to downwind SST gradient according to the regressed linear relationships in Figs. 4.27b and 4.27f, data counts in pixels of wind stress divergence and surface current divergence for the case with surface current coupling switched on but thermodynamic coupling switched off (b), and the case with both with surface current coupling and thermodynamic coupling switched on (d).

Fields of downwind SST gradient and surface current divergence in the subdomain of symmetric instability bands are shown in Figs. 4.29a and 4.29b. Blue bands of negative surface current divergence in Fig. 4.29b correspond to bands consisting of positive and negative downwind SST gradients in Fig. 4.29a. Data count in pixel of surface current divergence and downwind SST gradient is shown in Fig. 4.29c; in which downwind SST gradient spreads widely in the range of negative surface current divergence. Thus, the scattered patterns in Figs. 4.28a and 4.28c are caused by the downwind SST gradient, which are scattered across wide ranges in Fig. 4.29c. Comparing Figs. 4.29c and 4.15c reveals that the relationship between surface current

divergence and downwind SST gradient is not a linear function, while a negative-slope linear relationship exists between surface current curl and crosswind SST gradient.

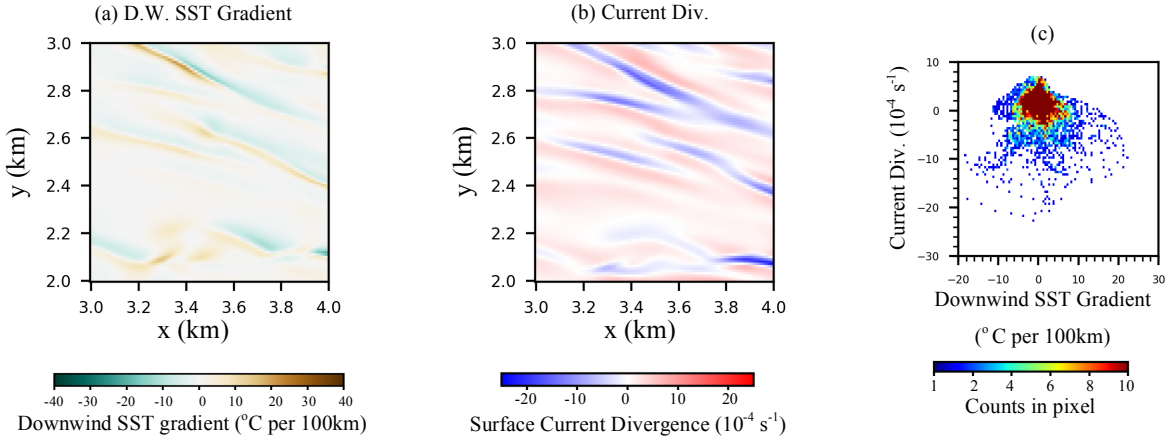

Figure 4.29: Shading contours of downwind SST gradient and surface current divergence over the subdomain of symmetric instability surface bands are shown in (a) and (b). Data counts in pixels of them are shown in (c).

4.1.3 Time Series of Wind Stress Curl and Divergence

In sections 4.1.1 and 4.1.2, wind stress curl and divergence over submesoscale structures including fronts, eddies, and symmetric instability bands are discussed. In the submesoscale regime, wind stress curl and divergence can be introduced by both a strong SST gradient and surface current curl/divergence. When the surface current coupling is switched on, wind stress curl/divergence is primarily contributed by surface current curl/divergence. However, when surface current coupling is deactivated, which is quite common in numerical models because current velocity is usually much smaller than wind speed, wind stress curl/divergence is mainly contributed by crosswind/downwind SST gradient. Coupling coefficient ts in thermodynamically uncoupled cases with prescribed atmospheric temperatures are greater than those in the coupled cases. Therefore, various wind stress fields can be modeled using different air-sea schemes (surface current coupling and/or thermodynamic coupling is switched on or off). These wind fields force the ocean to evolve differently and their sea surface properties are dissimilar in terms of promoting the growth of the differences among the wind stress fields. Thus, wind stress curl and divergence over the channel domain can evolve differently in each of the experiments.

4.1.3.1 Time series of wind stress curl. Fig. 4.30 shows a time series of averaged positive and negative wind stress curl over the channel domain. The left panels in Fig. 4.30 represent cases with surface current coupling switched off. The magnitudes of wind stress curl are smaller than 4×10^{-7} Nm^{-3} even when the forcing wind is 8 ms^{-1} westward, as shown in Fig. 4.30k. However, under the same wind forcing, if the surface current coupling is activated, magnitudes of positive and negative wind stress curl can be greater than 50×10^{-7} Nm^{-3}, as revealed in Fig. 4.30l. At the 48th hour in Fig. 4.30l, negative wind stress curls are about 10×10^{-7} Nm^{-3} greater than positive wind stress curls, which means the net wind stress curl over the domain is about -10×10^{-7} Nm^{-3}. Comparing Fig. 4.30l to the global wind stress curl observations from the QuikSCAT scatterometer (Risien & Chelton, 2008), the net value of averaged wind stress curl over the channel domain is greater than the maximum wind stress curl magnitude observed by the satellite, which is about 3×10^{-7} Nm^{-3}. The length and width of the channel domain is 5 km and the resolution of the QuikSCAT observation is about 25 km. Hence, even with the limitations of CheapAML, the modeled wind stress curl in a finer resolution is more than two times greater than what is observed over larger length scales.

Furthermore, if the net averaged wind stress curl is simply used to represent wind stress curl over the domain in the channel domain itself, positive and negative wind stress curl of much greater magnitudes within the domain will be ignored. According to linear and nonlinear Ekman theories (Gaube et al., 2015), wind stress curl is related to Ekman pumping that can introduce vertical exchanges at the upper ocean. If the channel domain is filled with large positive and negative wind stress curl, strong vertical exchanges can be associated with them. However, if only the net wind stress curl is considered as the wind stress forcing, the net Ekman pumping over the whole domain is the same value but the vertical exchanges within the domain are suppressed to a large extent.

The steep increasing lines in the 5th to 12th hours in both Figs. 4.30k and 4.30l reflect the growth of symmetric instability surface bands during this period. The formation and development of the symmetric instability surface bands will be discussed in Chapter 5. The gentle increasing lines from the 12th to 48th hour in Figs. 4.30m and 4.30 n imply that the growth of symmetric instability surface bands is much slower when it is forced by an 8 ms^{-1} eastward wind.

In Fig. 4.30l, the net wind stress curls for Exp8W-UC and Exp8W-CC are negative. However, in Fig. 4.30k, the net wind stress curls for Exp8W-UN and Exp8W-CN are positive. The difference between the solid line and the dashed line represents the net wind stress curl. Hence, the net wind stress curl in the case with thermodynamic coupling switched off is greater than in the case with thermodynamic coupling switched on, and the net wind stress curl for Exp8W-CN is close to zero after the 40^{th} hour. The comparison of averaged wind stress curl magnitudes in Figs. 4.30k and 4.30l indicates that current curl introduces more than 90% of the wind stress curl when it is forced by an 8 ms^{-1} westward wind. The same conclusion can be drawn from the comparison between Figs. 4.30m and 4.30n.

The negative wind stress curl damping during the first 12 hours in Exp8E-UN and Exp8E-CN (shown in Fig. 4.30m) reveals the attenuation of initial negative crosswind SST gradients. Similar processes also take place in Exp4E-UN and Exp4E-CN, as shown in Fig. 4.30i. Because all of the experiments have the same initial condition, the change of wind direction only switches the sign of crosswind SST gradient. Therefore, the initial positive and negative wind stress curls in Figs. 4.30c, 4.30g, and 4.30k have signs opposite to the ones in Figs. 4.30e, 4.30 i, and 4.30 m, respectively. That said, when the surface current coupling is activated, the initial positive and negative wind stress curl in Figs. 4.30d, 4.30h, and 4.30 l are not only opposite to those in Figs. 4.30f, 4.30j, and 4.30n; their magnitudes also vary when the wind direction is changed. For example, the magnitude of initial negative wind stress curl in Exp1W-CC is 0.7×10^{-7} Nm^{-3}, but the magnitude of initial positive wind stress curl in Exp1E-CC is about 1.0×10^{-7} Nm^{-3}. The reason for this is that the magnitude of relative wind speed depends on the wind direction, and the magnitude of wind stress is approximately a quadratic rather than a linear function of the magnitude of relative wind speed.

For the Exp1W- and Exp1E- experiments, the magnitudes of wind stress curl are smaller than 1.2×10^{-7} Nm^{-3}. Although no strong field of wind stress curl is generated under the weak wind forcing, the differences are significant among these wind stress curl fields modeled by the different air-sea schemes. Even in the Control-UC and Control-CC experiments, the time series of positive and negative wind stress curl shows distinguishable differences (Fig. 4.30b).

4.1.3.2 Time series of wind stress divergence. Time series of averaged positive and negative wind stress divergence over the channel domain for the control run and wind forcing

experiments are showed in Fig. 4.31. The magnitudes of wind stress divergence in cases with surface current coupling switched on are much smaller than those in cases with surface current coupling switched off. This is especially obvious when comparing Figs. 4.31k and 4.31l, which show experiments forced by 8 ms^{-1} westward winds. Magnitudes of averaged wind stress divergences in Exp8W-UN and Exp8W-CN are less than 1.5×10^{-7} Nm^{-3}, while those in Exp8W-UC and Exp8W-CN are greater than 20×10^{-7} Nm^{-3} after the 12^{th} hour. This implies that activating the surface current coupling in the submesoscale regime can introduced wind stress divergence of great magnitudes.

In the left panels of Fig. 4.31, the time series of averaged negative wind stress divergence overlaps with the time series of averaged positive wind stress divergence, which means the net wind stress divergence in each experiment is zero. The zero net wind stress divergence is because: (i) the accumulation of downwind SST gradient over the periodic domain should be equal to zero, and (ii) wind stress divergence is linearly correlated with downwind SST gradient. However, in the right panels, the differences between time series of averaged positive and negative wind stress divergence are distinguishable. Thus, nonzero net wind stress divergence only appears in the experiments with surface current coupling activated.

Comparing Figs. 4.31 and Fig. 4.30 reveals that the magnitudes of positive and negative wind stress divergence are smaller than the magnitudes of positive and negative wind stress curl in each experiment. In addition, the net wind stress divergence in the right panels of Fig. 4.31, represented by the differences between the averaged positive and negative wind stress divergences, are much smaller than the net wind stress curl in the right panels of Fig. 4.30. Even in Exp8W-UC and Exp8W-CC, the magnitudes of net wind stress divergence are less than 1×10^{-7} Nm^{-3} most of the time. And, the maximum value of net wind stress divergence, which is less than 3×10^{-7} Nm^{-3}, appears in Exp8E-CC at the 10^{th} hour. These net wind stress divergences are comparable to the magnitudes of wind stress divergence of QuikSCAT measurements. However, take Fig. 4.31l as an example, even when the net wind stress divergence is small and comparable to observations, the magnitudes of averaged positive and negative wind stress divergences over the channel domain are more than 20 times greater than the magnitudes of observed wind stress divergences. Still, the influences of these positive and negative wind stress divergence on the ocean is not clear and the atmospheric feedbacks to these wind stress divergences are inactivated

by prescribed winds in CheapAML. The effects of the positive and negative wind stress divergence of large magnitudes on air-sea interactions should not be ignored in future works.

In terms of the experiments forced by 8ms-1 westward wind, the sharp rises of wind stress divergence magnitudes in Figs. 4.31k and 4.31l during the first 12 hours are consistent with the steep increases of wind stress curl magnitudes in Figs. 4.30k and 4.30l during the same period. This reflects rapid increases in the crosswind SST gradient, downwind SST gradient, and surface current curl and divergence during the symmetric instability development period (the first 12 hours). For those experiments forced by 8ms-1 eastward winds, wind stress divergence evolution shown in Figs. 4.31m and 4.31n reveale more gradual increases during the remainder of experiment period after the 12th hour.

In Figs. 4.30 and 4.31, magnitudes of both wind stress curl and divergence tend to have larger values when forced by wind with larger magnitudes. Strong westward winds with magnitudes greater than 4 ms^{-1} also tend to generate wind stress curl and divergence of greater magnitudes than those generated by eastward winds. Thus, the effect of wind magnitude and direction on wind stress curl and divergence will be investigated in section 4.2.

4.2 Effect of Wind Speed Magnitude on Coupling Coefficients

Slopes of linear regression of wind stress curl as a function of crosswind SST gradient and linear regression of wind stress divergence with respect to downwind SST gradient are defined as coupling coefficients (Maloney & Chelton, 2006). Magnitudes of the coupling coefficients showed a spatial diversity in work of Chelton et al. (2004). From the discussion in section 4.1, the magnitudes of coupling coefficients are associated with the magnitudes of wind speed. For example, when the forcing wind is 8 ms^{-1} westward, the coupling coefficient in Fig. 4.13b is significantly greater than the coupling coefficients in the subdomains of the front and eddy shown in Fig. 4.3b and Fig. 4.9b, which are of the same air-sea scheme but forced by 4 ms-1 westward winds. Wind stress curl can be generated when wind blows across the crosswind SST gradient because wind stress with different magnitudes due to different SSTs will form over crosswind SST gradient. Previous works concentrated on the relationship between the wind stress curl and crosswind SST gradient (Chelton et al., 2004; Maloney & Chelton, 2006; Risien

& Chelton, 2008). But research into whether the magnitude of the forcing wind could affect the coupling coefficient has not been conducted.

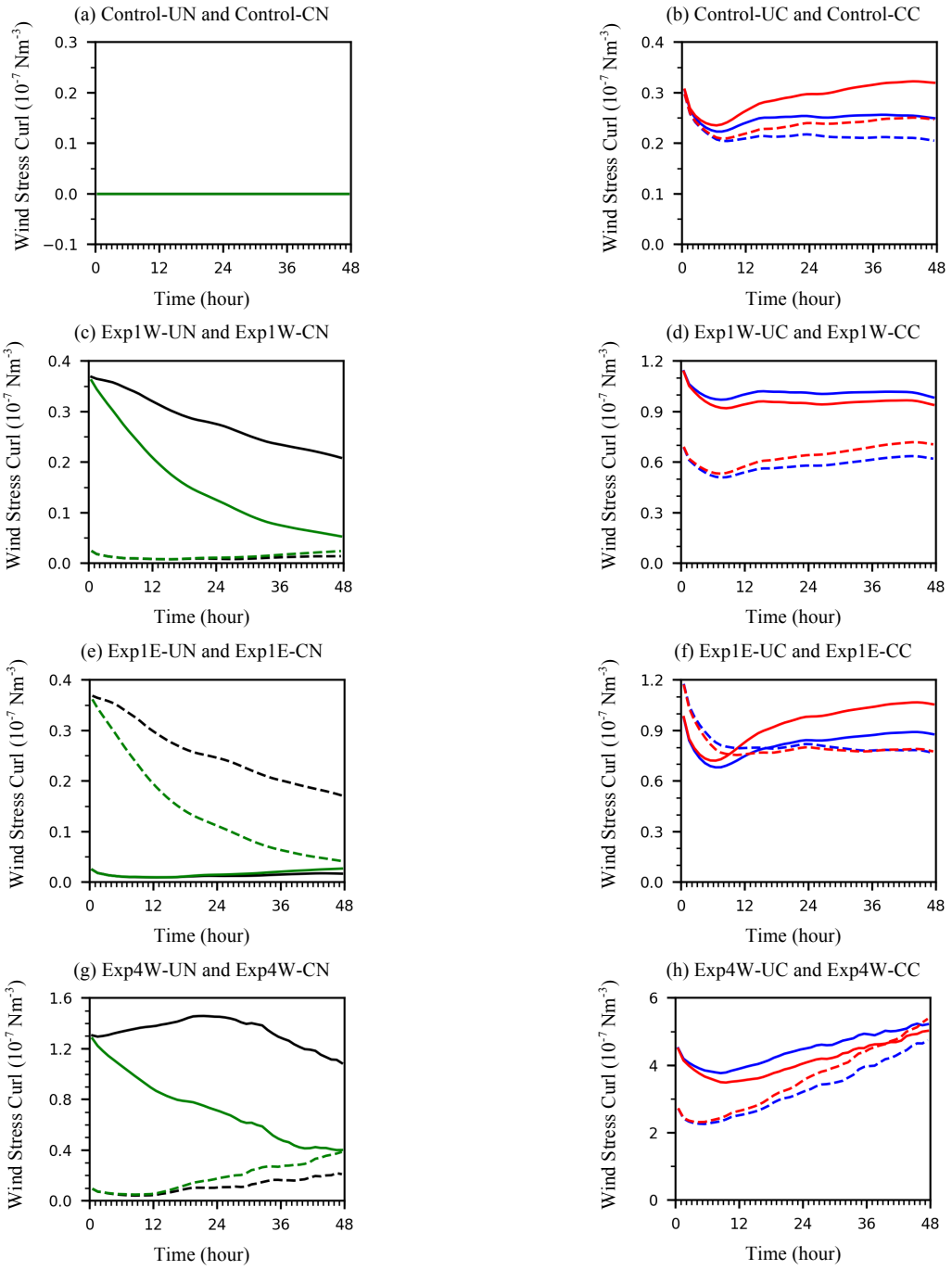

Figure 4.30: Time series of averaged positive (solid line) and negative (dash line) wind stress curl over the channel domain. Black: neither thermodynamic coupling nor surface current coupling is activated; Blue: thermodynamically uncoupled but surface current coupling is switched on; Green: thermodynamically coupled but surface current coupling is switched off; Red: both thermodynamic coupling and surface current coupling are switched on.

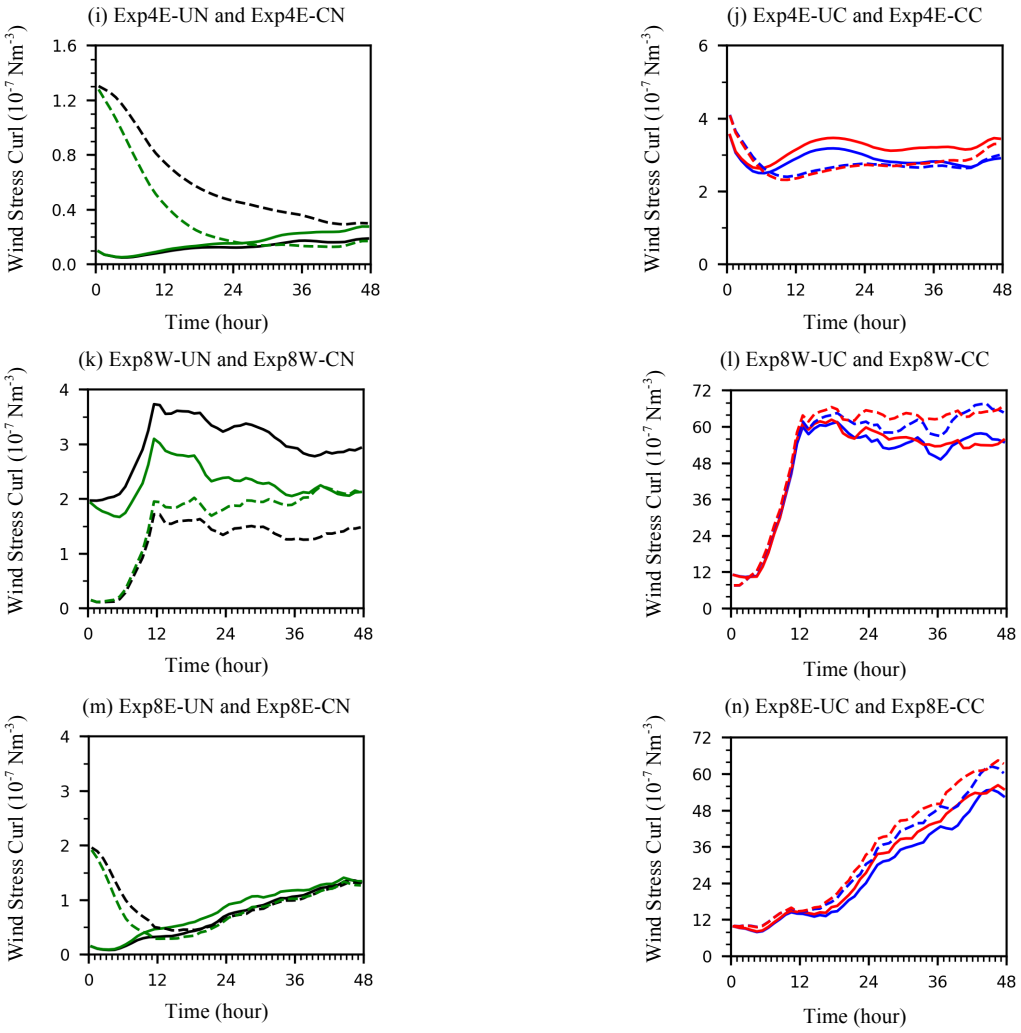

Figure 4.30 - continued

In order to investigate the relationship between forcing winds and coupling coefficients, a series of experiments are conducted under winds of different speeds and directions. The forcing winds range from 16 ms^{-1} westward wind to 16 ms^{-1} eastward wind. Because heat capacity of atmosphere is smaller than the heat capacity of water, the atmospheric temperature is expected to adjust to the SST field. Hence, experiments with thermodynamic coupling switched on are chosen, rather than the thermodynamically uncoupled experiments, to make the experiments more realistic. The experiments with surface current coupling activated allow current curl and divergence to introduce wind stress curl and divergence, while wind stress curl and divergence will be inevitably introduced by SST gradients. To remove the interruptions from the current and focus on the effect of wind forcing magnitude on one mechanism of wind stress curl/divergence genesis, the surface current coupling is switched off in the testing experiments.

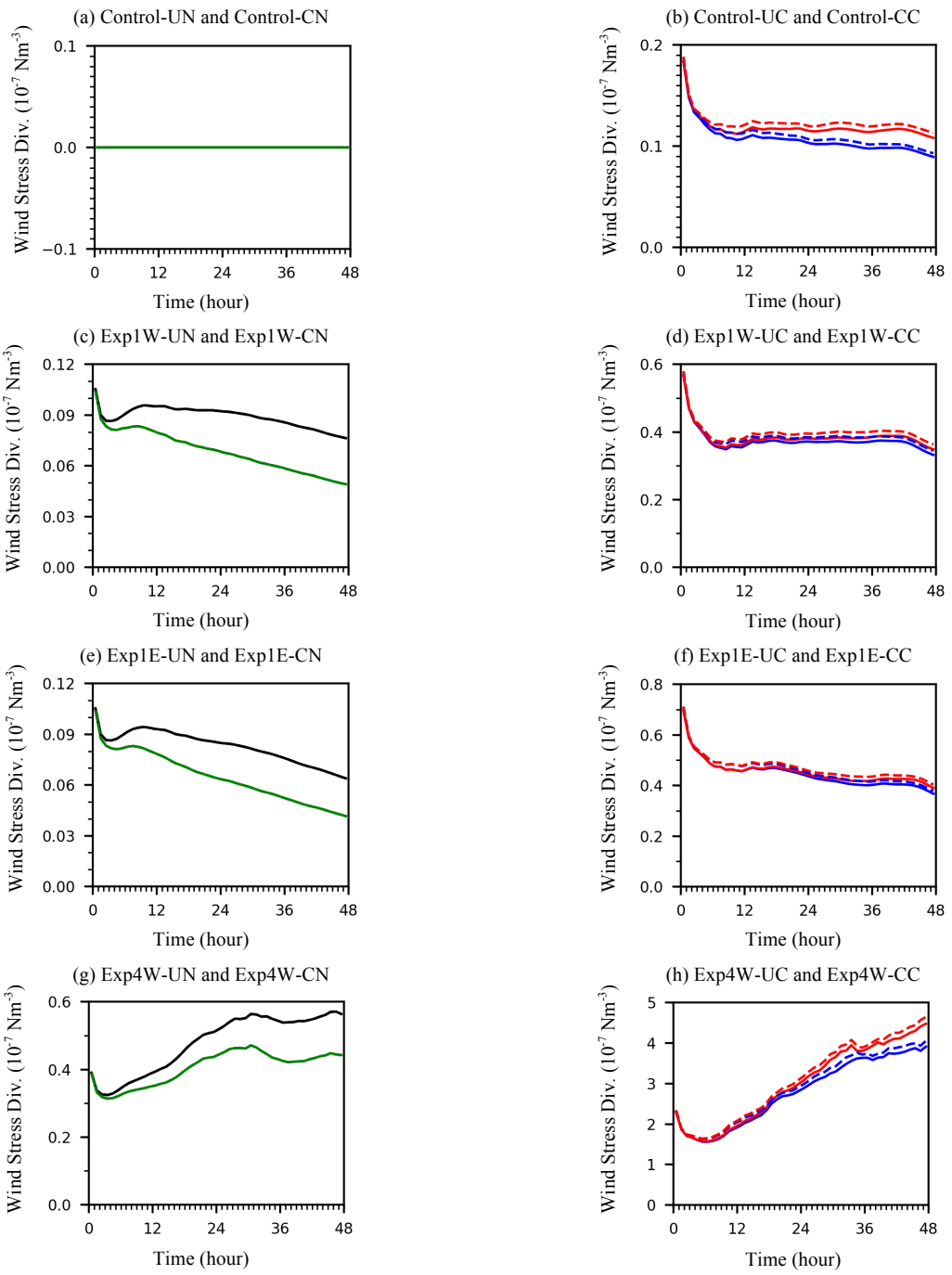

Figure 4.31: Time series of averaged positive (solid line) and negative (dash line) wind stress divergence over the channel domain. Black: neither thermodynamic coupling nor surface current coupling is activated; Blue: thermodynamically uncoupled but surface current coupling is switched on; Green: thermodynamically coupled but surface current coupling is switched off; Red: both thermodynamic coupling and surface current coupling are switched on.

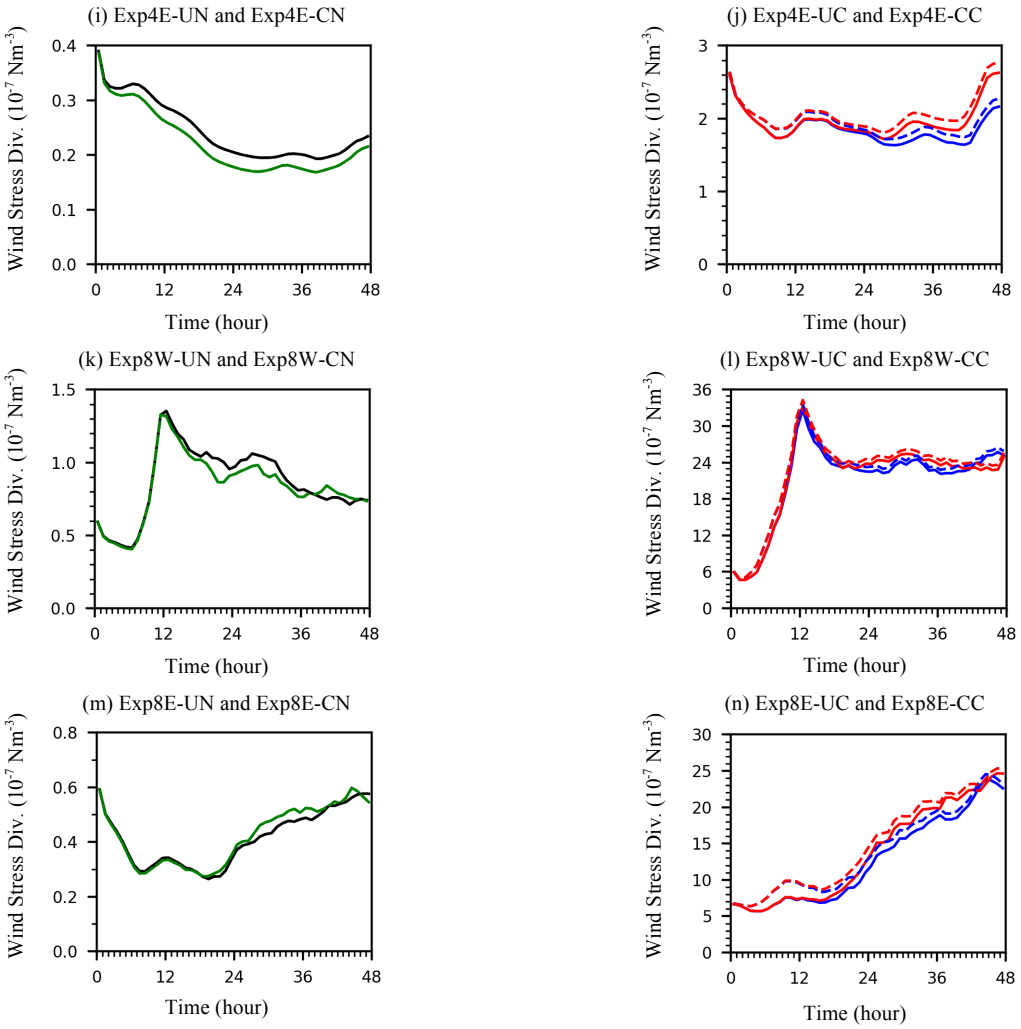

Figure 4.31 - continued

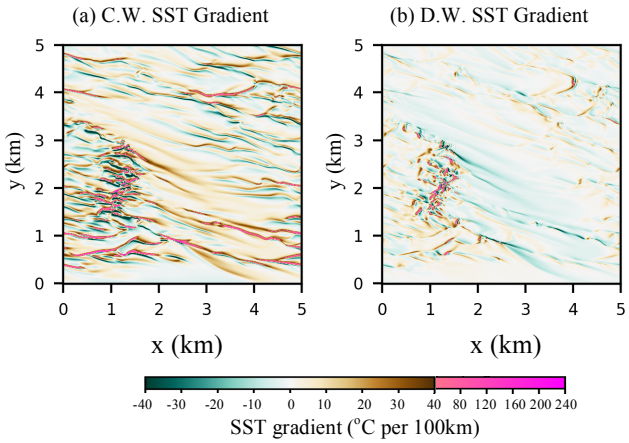

Figure 4.32: Shading contours of crosswind SST gradient (a) and downwind SST gradient (b) at the surface of Exp8W-CN at the 23rd hour.

The crosswind and downwind SST gradient fields, shown in Fig. 4.32, over the symmetric instability surface bands at the 23th hour in Exp8W-CN are used to test the sensitivity of coupling coefficients to wind speed magnitudes and directions. Ocean fields of the front and the eddy are not studied because the SST difference between the two sides of the front is significant, and crosswind and downwind SST gradients over the eddy are too small in value. The subdomain of symmetric instability surface bands are chosen also because the good linear relationships between wind stress curl/divergence and crosswind/downwind SST gradient revealed in Figs. 4.13a and 4.13 e, and Figs. 4.27a and 4.27e.

Comparing the fields of crosswind SST gradient and downwind SST gradient in Fig. 4.32 reveals the domain coverage and magnitudes of crosswind SST gradients are greater than those of downwind SST gradients. Linear regressions of wind stress curl with respect to crosswind SST gradient under different wind forces are shown in Fig. 4.33. Slopes of these linear regression lines in the right bottom area of each panel increase with increasing wind speed. However, the wind direction changing from westward to eastward does not seem to have a significant influence on the coupling coefficients. The lengths of error bars representing binned standard deviations also appear to be larger when the forcing winds are of greater magnitudes.

Linear regressions of wind stress divergence with respect to downwind SST gradient under different wind forces are shown in Fig. 4.34. Compared with results in Fig. 4.33, downwind SST gradient in Fig. 4.34 are of smaller magnitudes, which is consistent with the results in Fig. 4.32. Binned standard deviations represented by the lengths of error bars in Fig. 4.34 are greater than those in Fig. 4.33. While values of coupling coefficients in Fig. 4.34 tend to be smaller than those in Fig. 4.33.

Coupling coefficients in both Fig. 4.33 and Fig. 4.34 with respect to wind speed magnitudes are plotted in Fig. 4.35, in which coupling coefficients are positively correlated with wind speed magnitudes. Magnitudes of coupling coefficients increase quickly with wind speed with wind speed magnitude ranging from 2 ms^{-1} to 6 ms^{-1}. When wind speed magnitudes are greater than 8 ms^{-1}, the increasing rates of coupling coefficient with respect to wind speed magnitude become smaller. The coupling coefficients for relationships between wind stress curl and crosswind SST gradient are greater than those for relationships between wind stress divergence and downwind SST gradient.

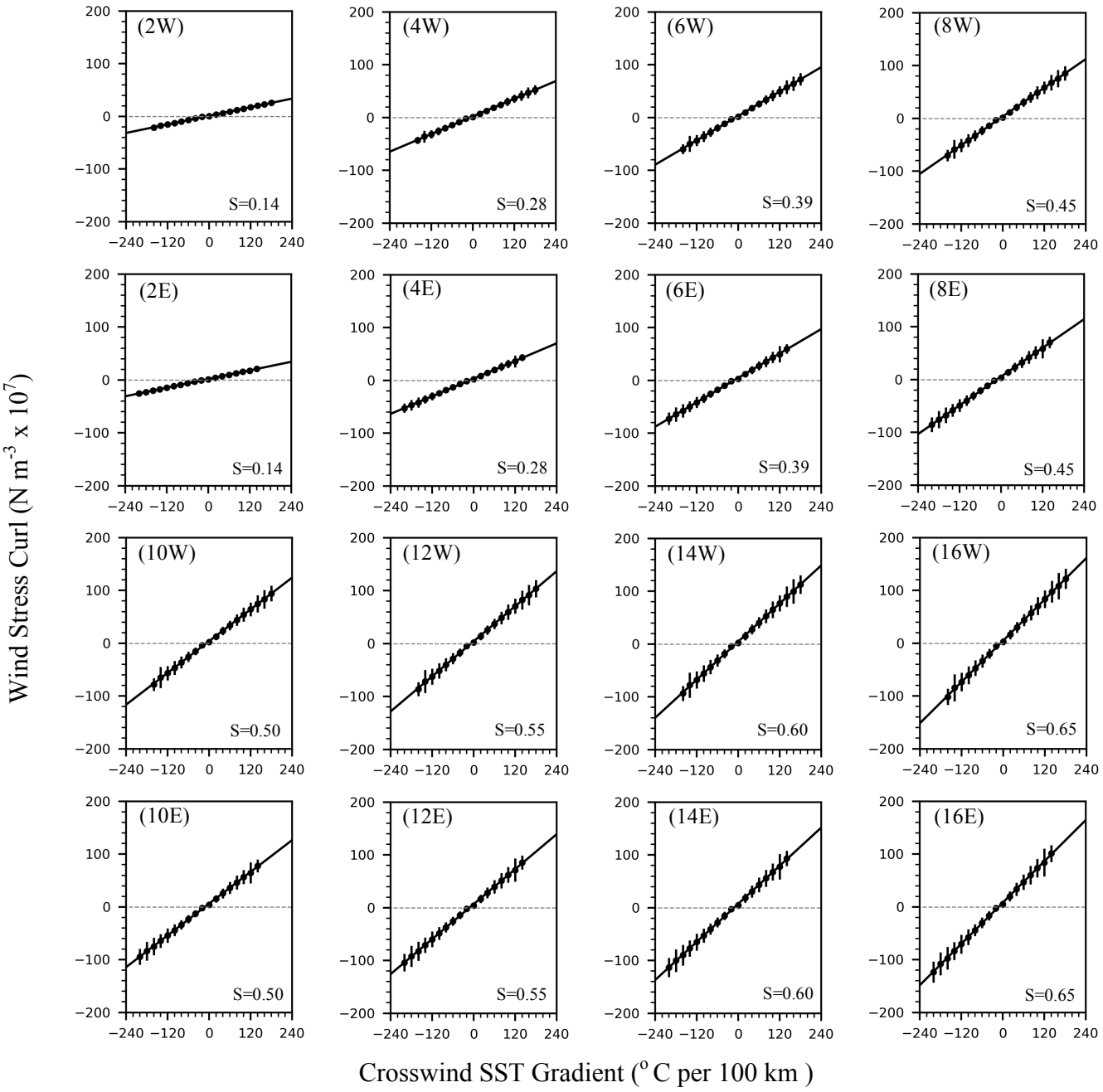

Figure 4.33: Binned means (circle) and ±1 standard deviations (error bars) of wind stress curl with respect to crosswind SST gradient, and linear regressions of wind stress curl as a function of crosswind SST gradient for the surface domain forced by winds range from 16 ms^{-1} westward wind (16W) to 16 ms^{-1} eastward wind (16E). The slope S of the least square error fitting line defined as coupling coefficient are labeled at the right bottom corner in each panel.

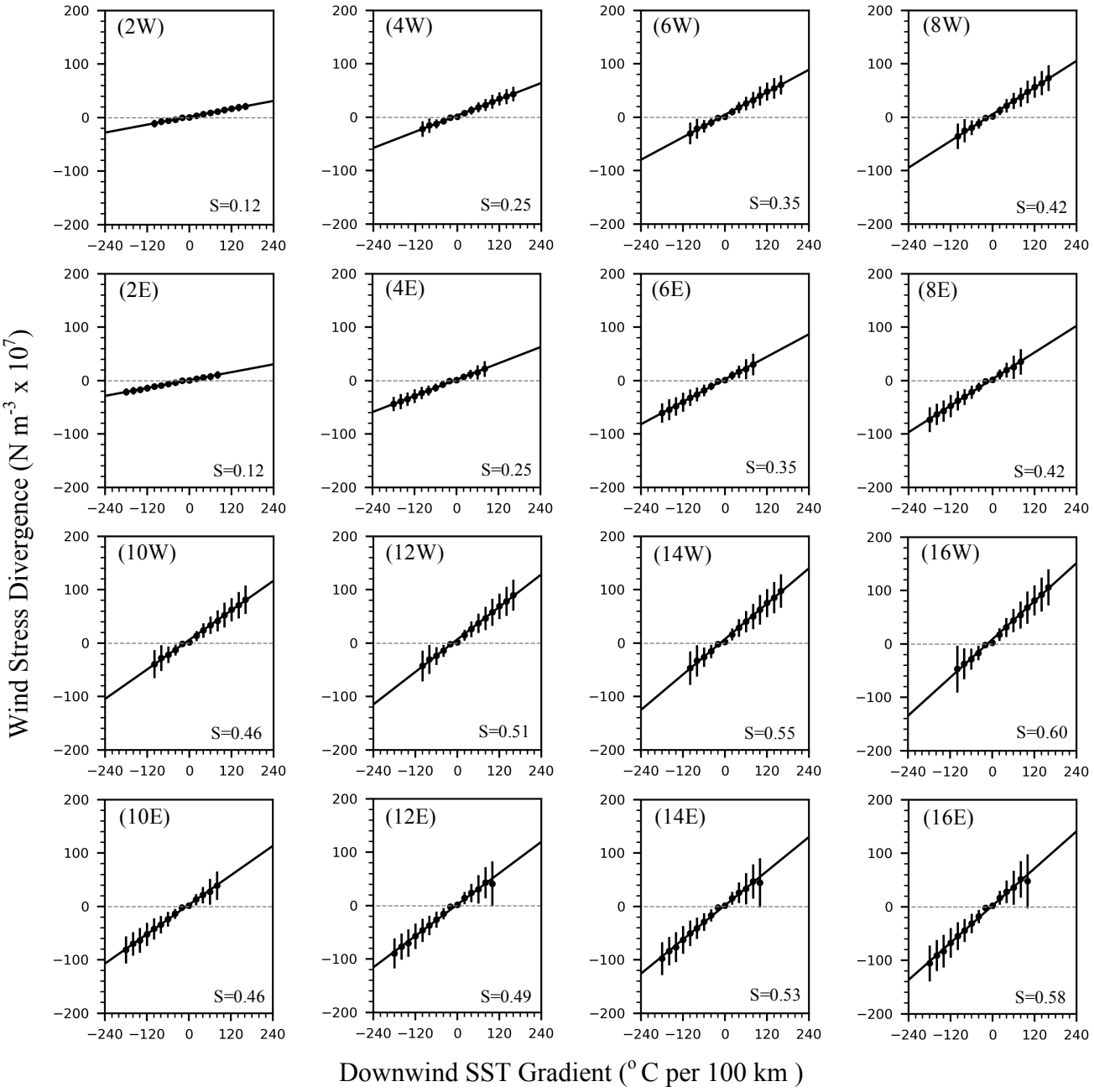

Figure 4.34: Binned means (circle) and ±1 standard deviations (error bars) of wind stress divergence with respect to downwind SST gradient, and linear regressions of wind stress divergence as a function of downwind SST gradient for the surface domain forced by winds range from 16 ms^{-1} westward wind (16W) to 16 ms^{-1} eastward wind (16E). The slope S of the least square error fitting line defined as coupling coefficient are labeled at the right bottom corner in each panel.

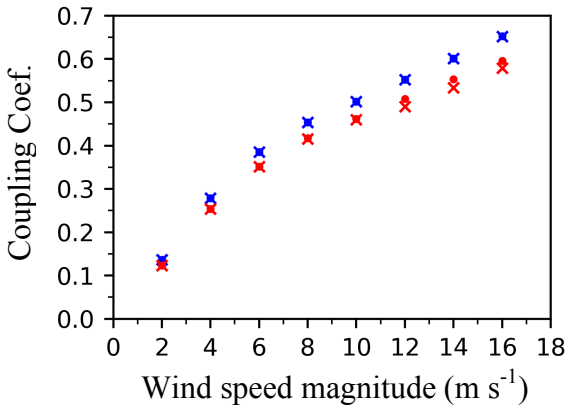

Figure 4.35: Coupling coefficients as a function of wind speed magnitude for relationship between wind stress curl and crosswind SST gradient (blue), and relationship between wind stress divergence and downwind SST gradient (red). Circles indicate westward winds and crosses indicate eastward winds.

This discrepancy could be attributed to the longer response time of the wind stress over the crosswind SST gradients, which are more of an east-west direction (Fig. 4.32a). The downwind SST gradients shown in Fig. 4.32a are more of a north-south direction, which means less time for the wind stress to respond to the downwind SST gradients beneath them. The increasing differences between the blue (wind stress curl versus crosswind SST gradient) and red (wind stress divergence versus downwind SST gradient) coupling coefficients with respect to wind speed magnitudes as shown in Fig. 4.35 reveals that faster wind has less time to respond to downwind SST gradients of a north-south direction. When the crosswind and downwind SST gradients are of a northwest-southeast direction, as shown in Fig. 4.2d and Fig. 4.17d, the response time of wind stress to crosswind and downwind SST gradients should be the same. Therefore, coupling coefficients for wind stress curl and divergence with respect to crosswind and downwind SST gradients are also of the same magnitudes, as shown in Fig. 4.3f and Fig. 4.18f.

4.3 Sensible Heat Flux and Latent Heat Flux in Submesoscale Regime

As longwave and shortwave radiation are set at zero in both the preliminary run and wind forcing experiments in this study, sensible and latent heat flux dominate the heat exchanges at the air-sea interface. Time series of averaged sensible heat flux and latent heat flux over the domain for the wind forcing experiments are plotted in Fig. 4.36 and Fig. 4.37, respectively. The

magnitudes of sensible heat fluxes are much smaller than the magnitudes of latent heat fluxes, which indicates that latent heat flux is dominating the heat exchanges between the sea surface and the atmosphere.

In Fig. 4.36, magnitudes of sensible heat fluxes increase with increasing wind speed magnitude. For cases forced by winds of the same magnitude but different directions, sensible heat flux differences between them are not significant, which implies that wind magnitude rather than wind direction directs the magnitude of sensible heat flux. In each panel of Fig. 4.36, the sensible heat fluxes of cases with thermodynamic coupling switched off (black and blue) are negative, which means that heat is transported from the atmosphere to the ocean. However, in cases with thermodynamic coupling switched on, heat is mainly transported from the ocean to the atmosphere, as the sensible heat fluxes are positive most of time. Switching on the surface current coupling does not seem to have a significant effect on the sensible heat flux over the domain. Nevertheless, a comparison between thermodynamically uncoupled cases forced by 8ms-1 westward and 8ms-1 eastward winds, shown in Figs. 4.36e and 4.36f, reveals that more heat flux is transported from the atmosphere to the ocean when forced by westward wind. This reflects more intensive instabilities in cases forced by wind along surface current direction (westward) pump more dense and cold water from bottom to the surface.

Magnitudes of latent heat fluxes are more than 40 times greater than those of sensible heat fluxes. Wind speed magnitudes also positively correlated with the magnitudes of latent heat fluxes. Similar to sensible heat fluxes, latent heat fluxes in cases with thermodynamic coupling switched on are mathematically greater than those of cases with thermodynamic coupling switched off under each wind force. Latent heat fluxes are of positive values as phase changes from water to water vapor only consume heat (they do not release heat). If surface current coupling is activated, the magnitude of relative wind speed is anticipated to be smaller than the magnitude of absolute wind speed when wind blows along current flow. Therefore, in Fig. 4.37a, latent heat fluxes in cases with surface current coupling switched on (red and blue) are smaller than those in cases with surface current coupling switched off (black and green).

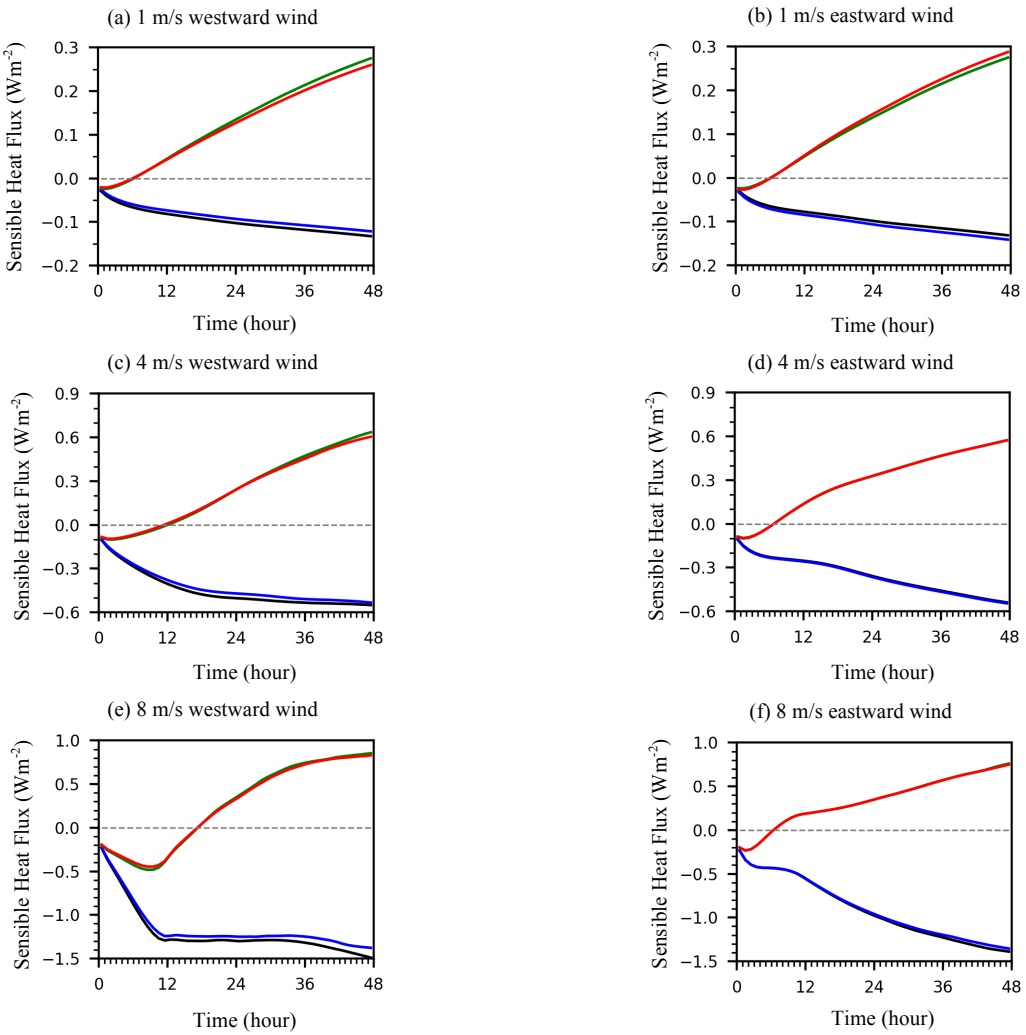

Figure 4.36: Time series of averaged sensible heat fluxes for wind forcing experiments. Black: neither thermodynamic coupling nor surface current coupling is activated. Blue: thermodynamically uncoupled but surface current coupling is switched on. Green: thermodynamically coupled but surface current coupling is switched off. Red: both thermodynamic coupling and surface current coupling are switched on.

On the other hand, when wind blows again the surface current flow, relative wind speed, which is greater than absolute wind speed, leads to larger latent heat flux in cases with surface current coupling activated. As a result Fig. 4.37b shows how latent heat fluxes in cases with surface current coupling switched on are greater than those in cases with surface current coupling switched off. Similarly, a comparison between Figs. 4.37c and 4.37d also reveals that latent heat fluxes in cases with surface current coupling activated are of greater values when wind blows against the surface current flow, and of smaller values when wind blows along the surface current flow.

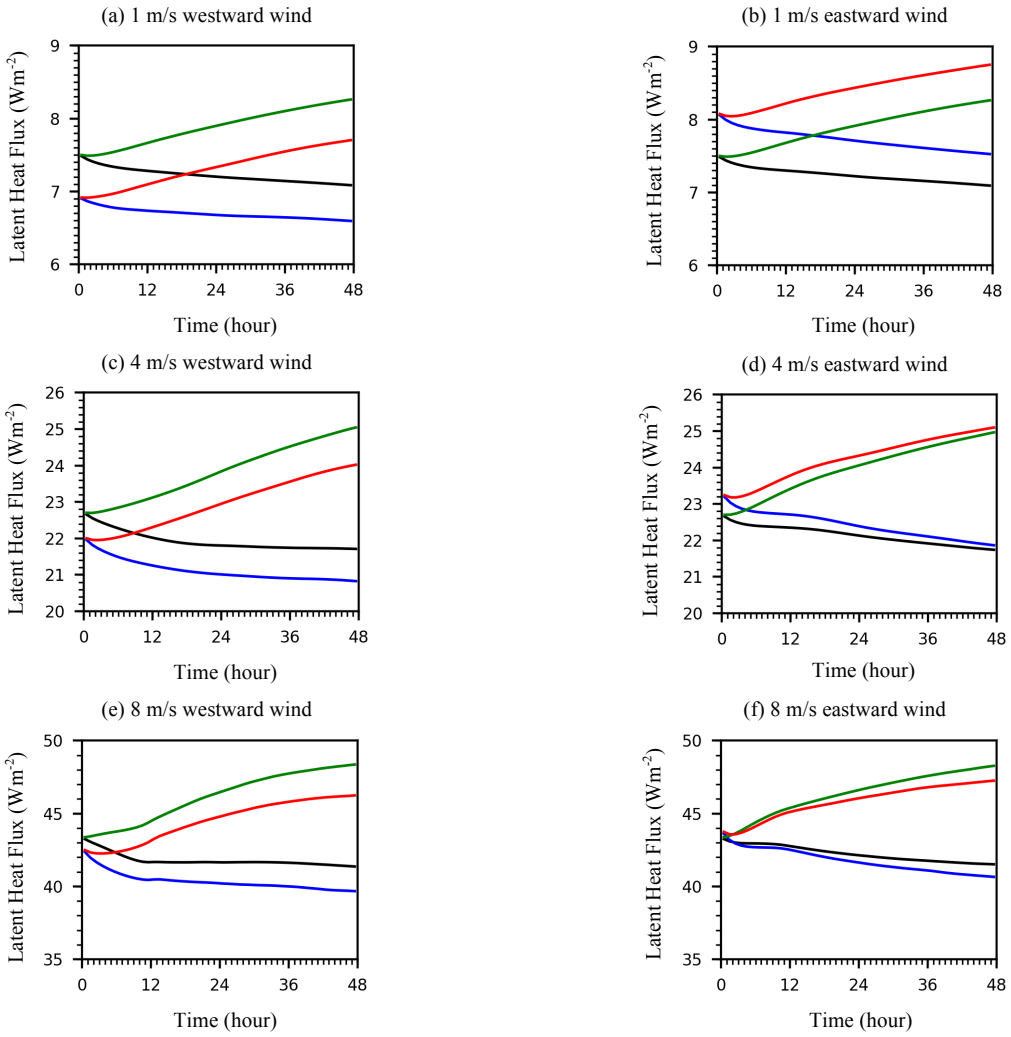

Figure 4.37: Time series of averaged latent heat fluxes for wind forcing experiments. Black: neither thermodynamic coupling nor surface current coupling is activated. Blue: thermodynamically uncoupled but surface current coupling is switched on. Green: thermodynamically coupled but surface current coupling is switched off. Red: both thermodynamic coupling and surface current coupling are switched on.

For cases forced by $8ms^{-1}$ westward winds (shown in Fig. 4.37e), the latent heat fluxes in cases with surface current coupling activated are at least 1 Wm^2 less than those in cases with surface current coupling deactivated. However, Fig. 4.37f shows that latent heat fluxes are still smaller in cases with surface current coupling switched on when wind blows eastward. It seems possible that these smaller latent heat fluxes are due to a forcing wind that is strong enough to change the direction of the surface flow from westward to eastward. After the surface current turns eastward, the latent heat fluxes in case with surface current coupling activated will have smaller latent heat flux comparing to those in cases with surface current coupling switched off

(Fig. 4.37f); and the growth of the latent heat fluxes difference between cases with surface current coupling switched on and off may be due to the surface flow acceleration by the eastward wind.

CHAPTER 5

INFLUENCE OF SUBMESOSCALE-MODIFIED WIND STRESS AND HEAT FLUXES ON THE EVOLUTION OF SUBMESOSCALE PROCESSES

5.1 Evolution of Submesoscale Processes

Results of the wind forcing experiments discussed in Chapter 3 show the submesoscale processes characterized with O (1) and greater Ro values evolve distinctly with different air-sea schemes. Implementing the same air-sea scheme, a more prominent diversity is revealed in the evolution of submesoscale processes forced by winds of various strengths and directions. The shape of the submesoscale front in the Control-, Exp1W-, and Exp1E- experiments is kept smooth as shown in Figs. 3.3, 3.4 and 3.7. However, in the Exp4W- experiments, the fronts are intensified and finally break into several segments (Fig. 3.5), while in the Exp4E- experiments, the tail of the original front weakens and a new strong front is formed on the upwind side of the eddy. The surface Ro fields in the Exp8W- and Exp8E- experiments at the 48^{th} hour only reveal a richness of symmetric instability surface bands; the original submesoscale fronts in the initial ocean fields no longer exist.

This chapter focuses on determining the influence of the submesoscale-modified air-sea fluxes on the evolution of submesoscale processes through a two-step exercise. First, because PV is a conservative and dynamically active tracer for ocean dynamics (Rhines, 1986; Thomas, 2005), the PV field is diagnosed to determine its association with the submesoscale evolution. Then, the PV injections contributed by different submesoscale-modified air-sea fluxes are assessed to quantitatively determine the effects of submesoscale-resolving air-sea interactions on the submesoscale dynamics.

5.1.1 Submesoscale Front Intensification

Submesoscale front intensifications on the upwind side of submesoscale eddy appear in the Exp4W- and Exp4E- experiments. Results presented in Chapter 4 demonstrate that both surface current coupling and thermodynamic coupling are important for modeling the submesoscale-modified air-sea fluxes. Therefore, the evolution of submesoscale fronts in

Exp4W-CC and Exp4E-CC is examined to investigate the front intensification processes on the upwind side of the eddy.

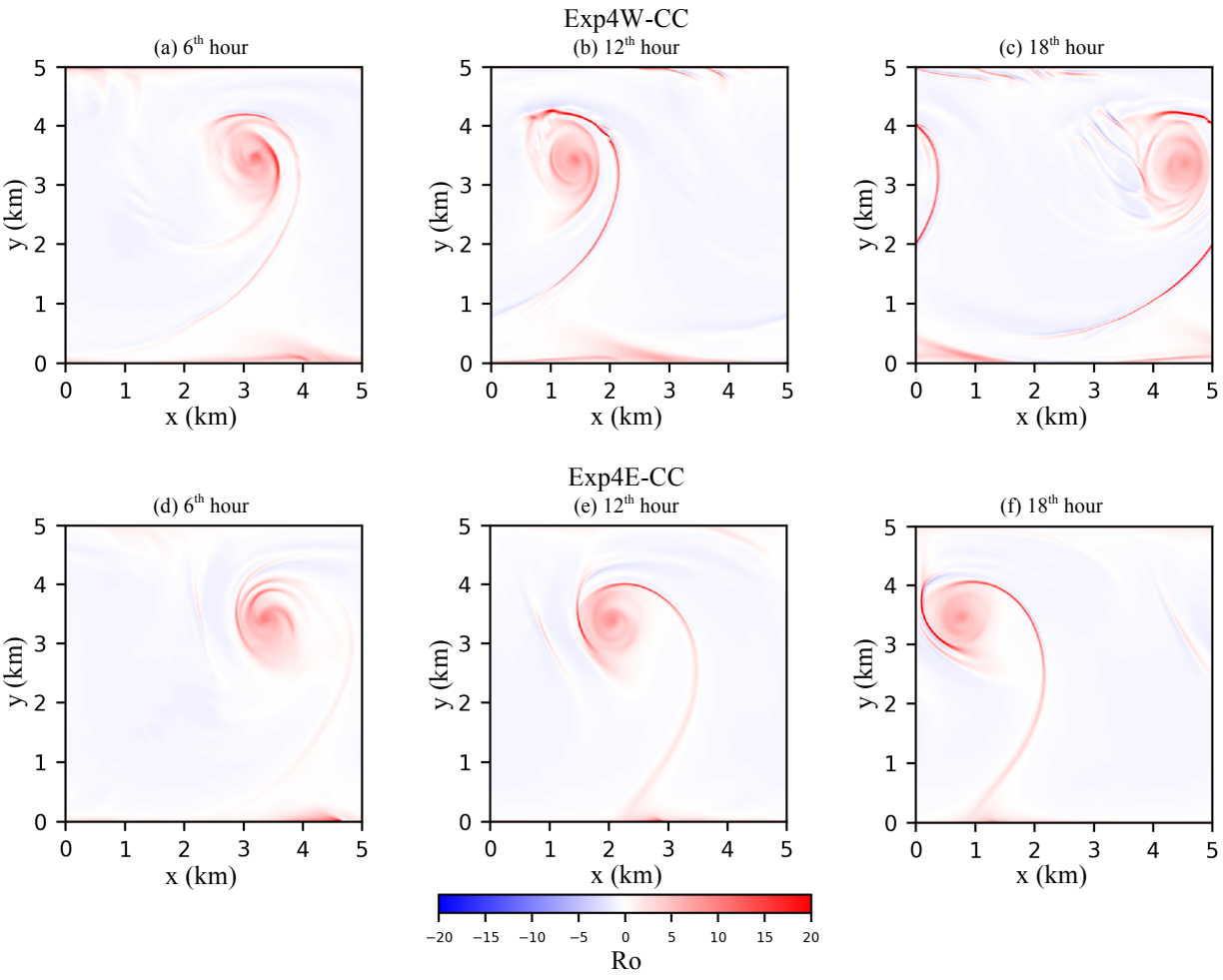

Figure 5.1: Surface Ro field of Exp4W-CC at the (a) 6th hour, (b) 12th hour, and (c) 18th hour and of Exp4E-CC at the (d) 6th hour, (e) 12th hour, and (f) 18th hour.

Fig. 5.1 reveals the surface fields of Ro in Exp4W-CC and Exp4E-CC at the 6th hour, 12th hour and 18th hour. The Ro values along the long submesoscale front on the upwind side of the eddy at the 6th hour in the Exp4W-CC experiments (Fig. 5.1a) strengthen at the 12th hour (Fig. 5.1b) and the 18th hour (Fig. 5.1c), and a shorter front is formed and intensified on the upwind side of the eddy in Exp4W-CC, as shown in Figs. 5.1d-f. To evaluate this front intensification at the surface, Hovmoller plots of averaged net PV, positive PV, and negative PV in each vertical layer for Exp4W-CC and Exp4E-CC are created (Figs. 5.2 and 5.3).

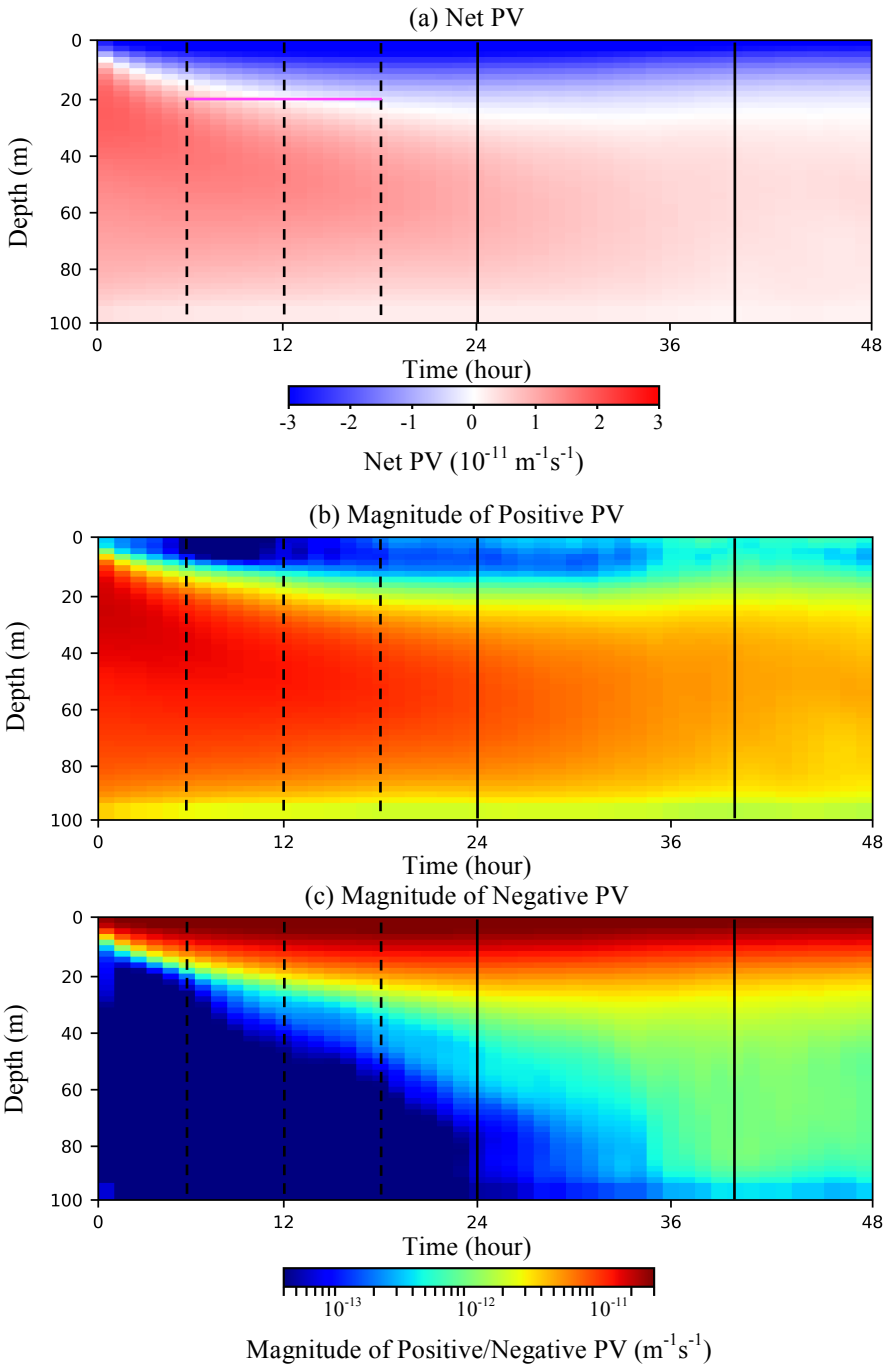

Figure 5.2: Hovmoller plots of mean net PV (a), positive PV (b), and negative PV (c) with respect to depth in Exp4W-CC.

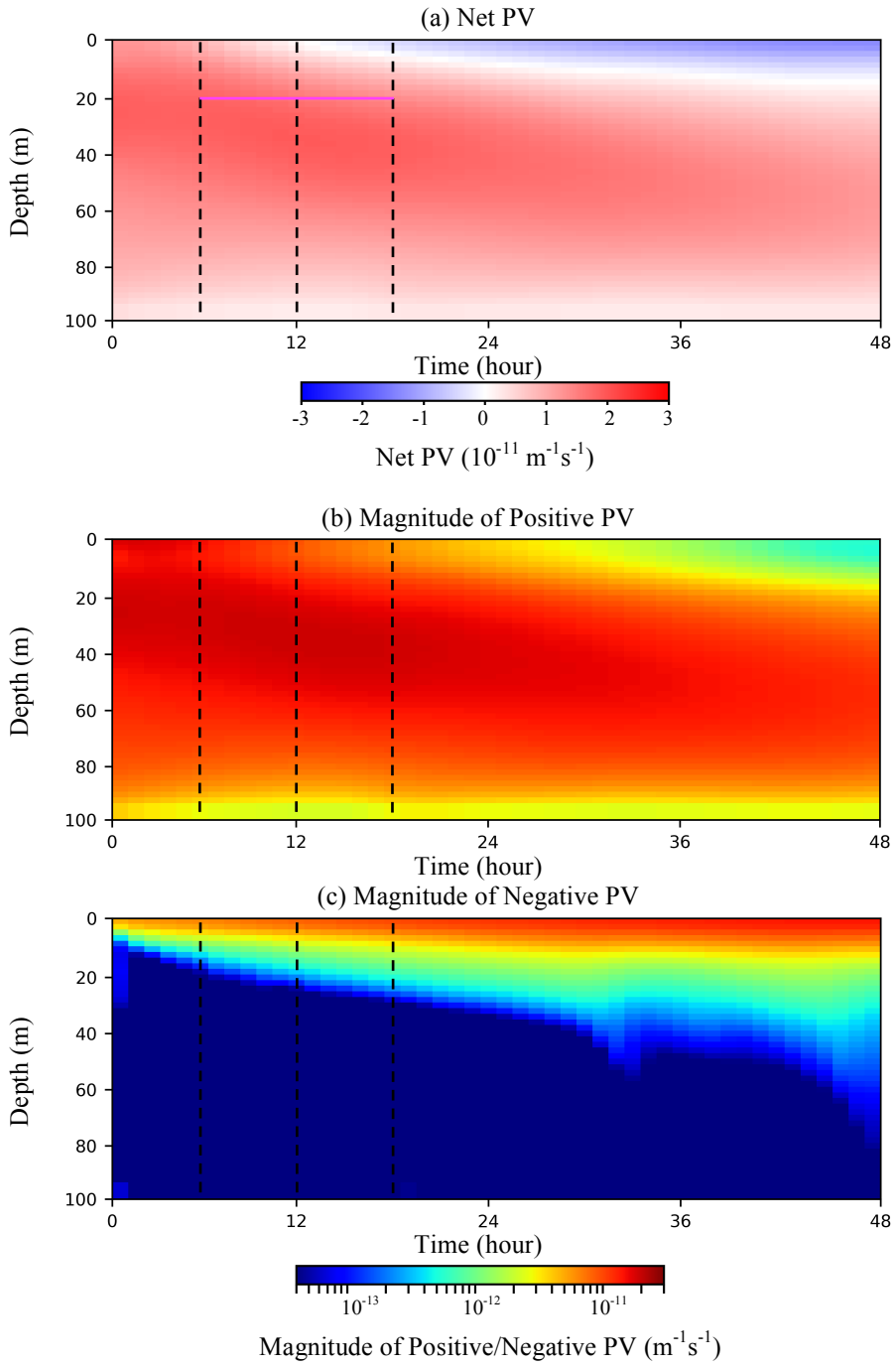

Figure 5.3: Hovmoller plots of mean net PV (a), positive PV (b), and negative PV (c) with respect to depth in Exp4E-CC.

The vertical profiles of averaged net PV at the 6th hour, 12th hour, and 18th hour in Exp4W-CC (shown as the three dashed lines in Fig. 5.2a) reveal negative PV is accumulated at the surface and is extended to a deeper layer during the period of front intensification. Averaged

positive and negative PV profiles illustrated by the dashed lines in Figs. 5.2b and 5.2c confirmed the negative PV accumulation near the surface and a penetration of negative PV to a deeper layer with time. The initial strong positive PV in depths of 10-50 m decreases as the negative PV penetrates to deeper layers. The vertical PV profiles for the three front intensification snapshots in Exp4E-CC, marked by the dashed lines in Fig. 5.3, reveal a near-surface weaker negative PV accumulation and its extension to deeper layers to compensate for positive PV there after the 12th hour. During the first 12 hours, the surface and near-surface layers filled with net positive PV, implying that the negative PV is too weak to compensate for strong positive PV there.

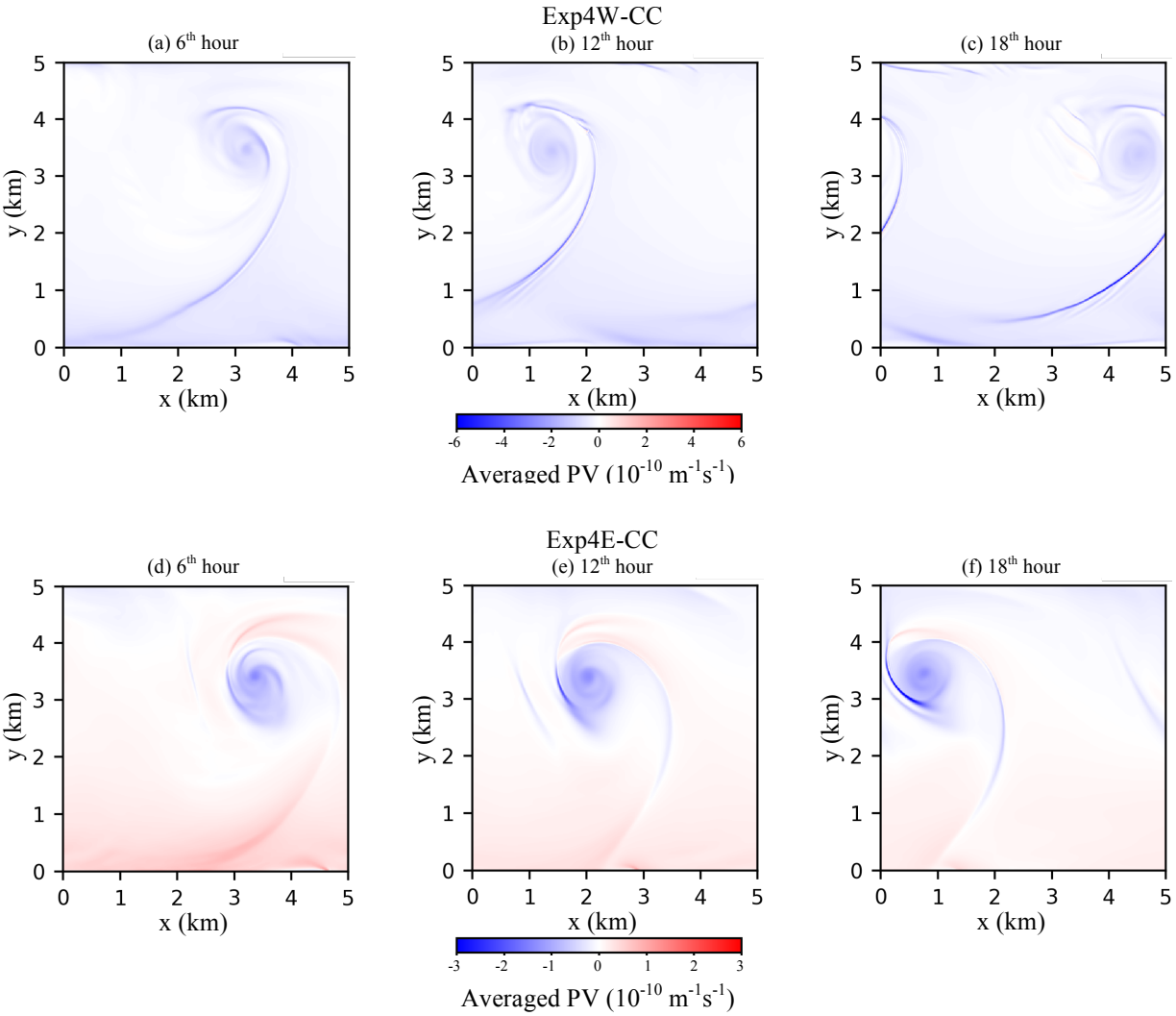

Figure 5.4: Averaged PV for the upper ocean layer from the surface to 10m deep for Exp4W-CC at (a) 6th hour, (b) 12th hour, and (c) 18th hour; and of Exp4E-CC at the (d) 6th hour, (e) 12th hour, and (f) 18th hour.

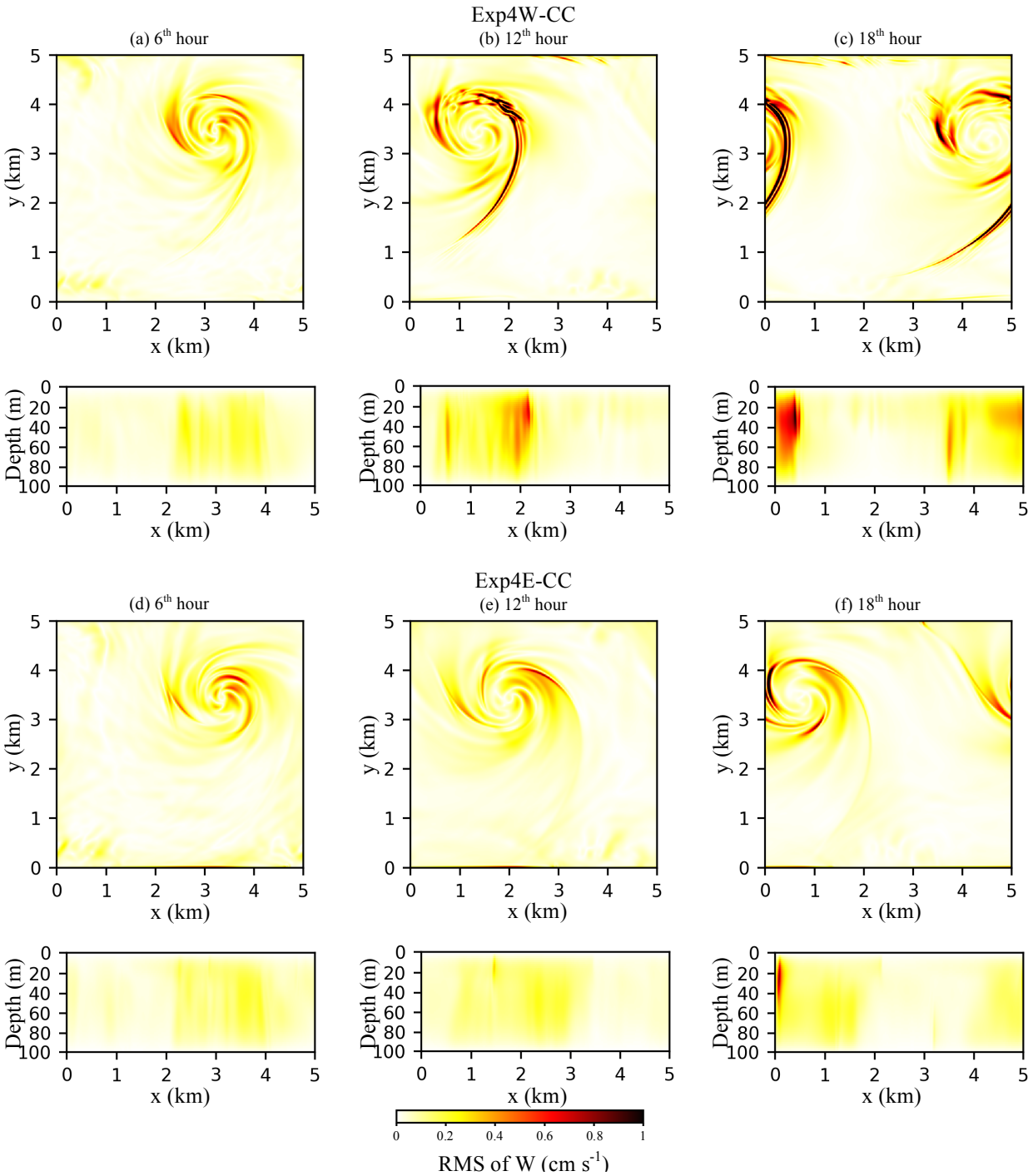

Figure 5.5: Averaged root mean square of w along depth and along y direction for Exp4W-CC at (a) 6th hour, (b) 12th hour, and (c) 18th hour and for Exp4E-CC at the (d) 6th hour, (e) 12th hour, and (f) 18th hour.

Vertically averaged PV from the surface to 10 m deep in Fig. 5.4 clearly shows a horizontal distribution of PV near the surface. For regions free of submesoscale processes in the domain, the near-surface PV is negative when forced by westward wind (Figs. 5.4a, 5.4b, and 5.4c) and positive when forced by eastward wind (Figs. 5.4d-f). For the eddy field, the near-surface PV is negative no matter what direction the wind blows. In contrast to Fig 5.1, Fig. 5.4 shows that the near-surface PV in submesoscale front regions are negative and of much greater magnitudes than those in the rest of the domain area. Front intensifications take place in regions where negative PV is accumulated on the upwind side of the eddy.

Furthermore, vertical velocity enhancements are found in conjunction with the front intensifications. Root mean square (RMS) of vertical velocity along the vertical direction and the south-north direction for Exp4W-CC and Exp4E-CC at the 6^{th} hour, 12^{th} hour, and 18^{th} hour are shown in Fig 5.5. At the 6^{th} hour, no RMS of vertical velocity greater than 0.01 ms^{-1} is found in the domain for both Exp4W-CC and Exp4E-CC (Fig. 5.5a and 5.5d). Six hours later, the vertical velocity beneath the strengthened surface front is significantly enhanced in Exp4W-CC, while the vertical velocity in Exp4E-CC is still weak and the front intensification is just beginning to occur. The vertical velocity in Exp4E-CC eventually strengthens at the 18^{th} hour as shown in Fig. 5.5f, and the strongest vertical velocity in the domain is recognized beneath the intensified front on the upwind side of the eddy. The vertical velocities in Exp4W-CC are always stronger than those in Exp4E-CC at the 18^{th} hour, but the most strengthened vertical velocity is in conjunction with the intensified front on the upwind side of eddy. Because Fig. 5.4 shows negative PV is mostly accumulated at the intensified front, it is expected that the enhanced vertical velocity beneath the strong negative PV regions has some influence on the vertically redistribution of the negative PV.

Figs. 5.1, 5.4, and 5.5 reveal that negative PV is accumulated at the front on the upwind side of the eddy. Front intensification and vertical velocity enhancement are also recognized at the same locations. Therefore, we speculated that these strong vertical velocities tend to transport the negative PV from the near-surface layer to a deeper interior. As previously mentioned, Fig 5.2a shows the penetration of negative PV from near-surface layers to greater depth between the 6^{th} hour and the 18^{th} hour. In order to verify the speculation on the vertical transport of negative PV, a layer at 20 m, shown as the magenta lines in Figs. 5.2a and 5.3a, is chosen to view the PV

field during this period. As seen in Fig 5.2a, the averaged PV at 20 m is positive at the 6th hour, but is attenuates to zero at the 12th hour, and becomes negative at the 18th hour.

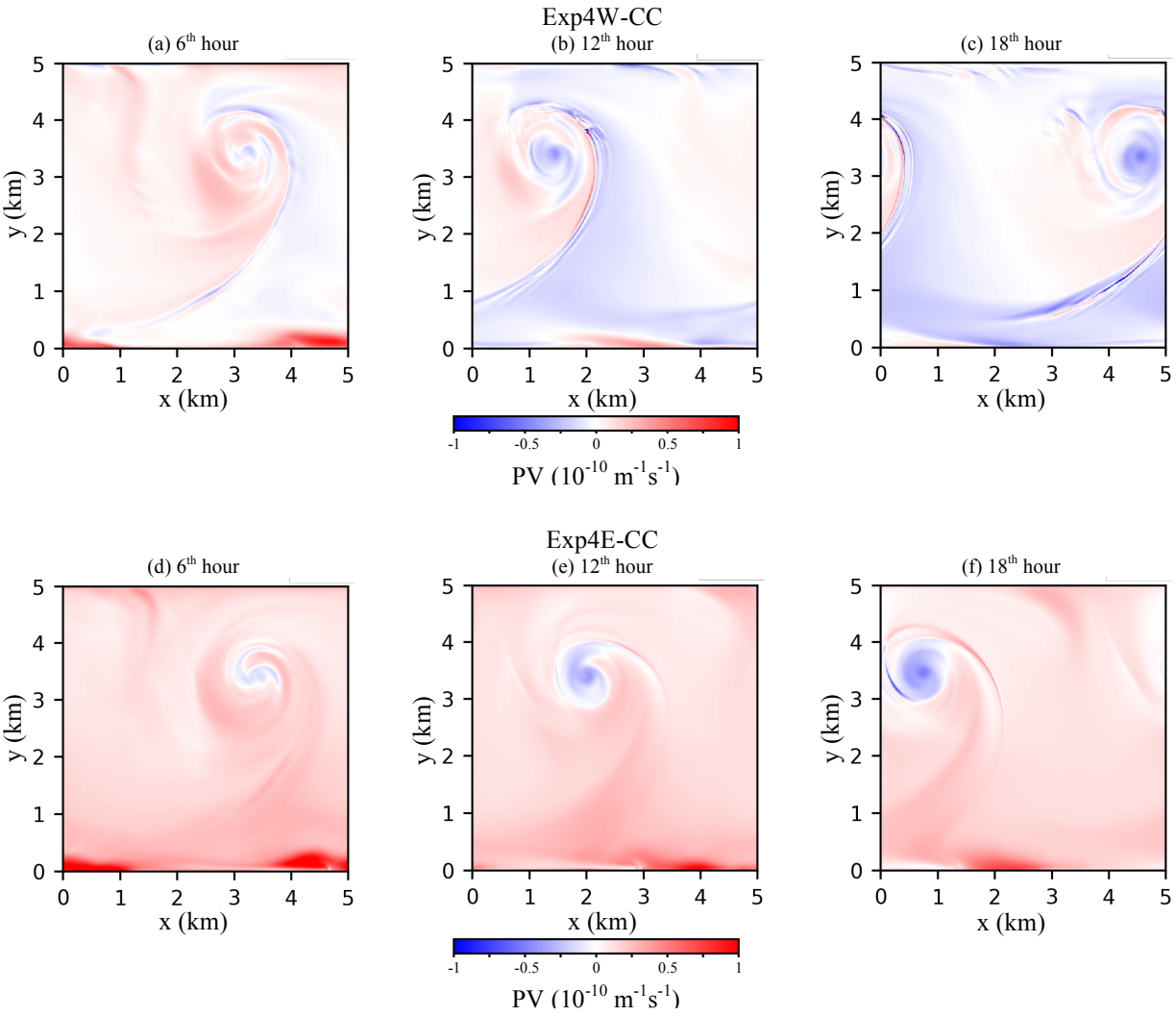

Figure 5.6: PV at 20 m for Exp4W-CC at the (a) 6th hour, (b) 12th hour, and (c) 18th hour; and of Exp4E-CC at the (d) 6th hour, (e) 12th hour, and (f) 18th hour.

The PV fields at 20 m in Exp4W-CC at the 6th hour, 12th hour and 18th hour are shown in Figs. 5.6a-c, revealing an increase in negative PV. The strongest negative PV appears at the regions of the front, while moderate increases arises at the eddy's center and areas adjacent to the front. There is also an increase of negative PV at the 20-m depth in Exp4E-CC as shown in Figs. 5.6d-f. However, the strength of negative PV in Exp4E-CC is much weaker than in Exp4W-CC (Figs. 5.6a-c). Because no significant front intensification or vertical velocity enhancement takes

place at the 6th hour and 12th hour, no prominent area filled with strong negative PV is observed at these two fields. Fig 5.6f shows an intense structure of negative PV appearing on the upwind side of the eddy at the 18th hour. This is consistent with our speculation that negative PV is transported from the near-surface layers to the layer at 20-m depth by a strong vertical velocity in conjunction with an intensified front. In other words, the front intensification is considered as a result of negative PV accumulation at the near-surface layers. Vertical velocity enhancement appears to accompany the front intensification and transport negative PV to deeper layers.

Since PV is a conservative tracer, it is important to consider where the negative PV comes from. The initial averaged PV vertical profile shown in Fig 5.2 indicates that the ocean interior is fulfilled with positive PV at larger magnitudes. Therefore, the air-sea interface is the only possible source of negative PV. In order to quantitatively assess the PV source at the air-sea interface, PV flux at the ocean surface at the 12th hour is diagnosed for Exp4W-CC and Exp4E-CC in Fig. 5.7 According to Marshall et al. (2001), the total PV flux described in Eq. (9), and its components shown in Eq. (10) are diagnosed.

$$\frac{\partial(\rho Q)}{\partial t} + \nabla \bullet J = 0 \tag{9}$$

$$\vec{J} = \rho Q \vec{V} + \vec{\omega}\frac{D\sigma}{Dt} + \vec{F} \times \nabla\sigma + \left(\frac{\Phi}{\rho_0}\nabla\rho'\right) \times \nabla\sigma \tag{10}$$

In Eqs. (9) and (10), ρ and Q are in situ density and PV, t represents time, ρ_0 is constant density, σ is the anomaly in the potential density, Φ is the geo-potential, vectors of $\vec{J}$, $\vec{V}$, $\vec{F}$, and $\vec{\omega}$ are PV flux, velocity, frictional force per unit mass, and absolute vorticity, respectively.

The fourth term on the right side of Eq. (10) is PV flux, which is introduced by *in situ* density variance along surfaces due to thermobaric effects (McDougall, 1988). Because the linear equation of state shown in Eq. (2) is implemented in this study, *in situ* density surfaces completely overlap potential density surfaces; thus, the PV flux contributed by the fourth term on the right side of Eq. (10) is zero. The first term, $\rho Q\vec{V}$, is the PV advection term. The $\vec{\omega}\frac{D\sigma}{Dt}$ term is considered to be diffusive term, because it is closely related to the variance of potential density, which is closely related to heat diffusion at the ocean surface. The third term, $\vec{F} \times \nabla\sigma$,

determined by the magnitudes and directions of frictional force and potential density gradient, is called the “frictional term” here.

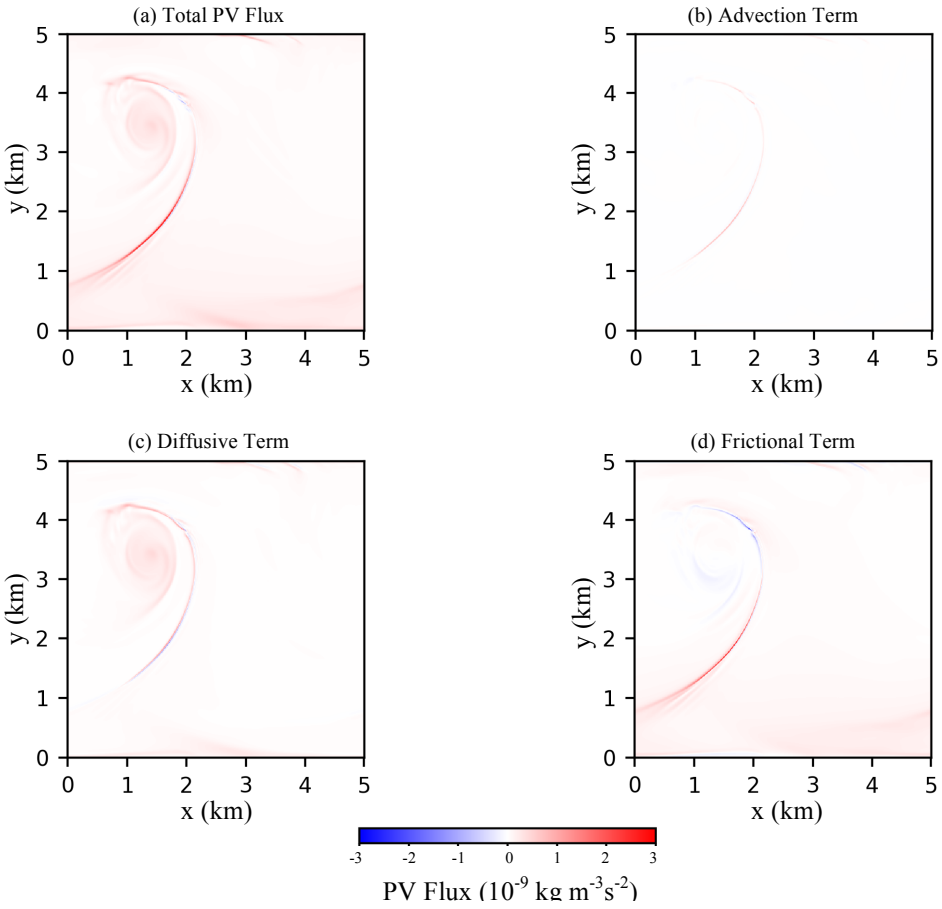

Figure 5.7: Total PV flux at the surface for Exp4W-CC at the (a) 12th hour and its components contributed to the (b) advection term, (c) diffusional term, and (d) frictional term.

The total PV surface flux in Fig. 5.7a reveals a positive PV flux over the ocean surface. The upward positive PV flux represents an injection of negative PV into the ocean. Intense negative PV flux concentrates along the submesoscale front structure on the south side of the east-west turning point. The front portion on the north side of the east-west turning point shows a less intense negative PV flux. And the pattern of the surface PV flux is consistent with the averaged PV field of near-surface layers shown in Fig. 5.4b. Fig 5.7b reveals a weak negative PV flux advection that only appears along the submesoscale front. Negative PV flux over the eddy and along the submesoscale front is introduced by the diffusive term in Fig. 5.7c. The frictional term contributes positive and negative PV flux along the front portions on the north and south

sides of the east-west turning point (Fig. 5.7d). Therefore, the intense negative PV flux on the front portion on the south side of the east-west turning point in Fig. 5.7a is a result of the superimposition of negative PV fluxes of the three terms. On the front portion on the north side of the east-west turning point, the negative PV flux introduced by advection term and diffusive term is compensated for by the positive PV flux attributed to the frictional term.

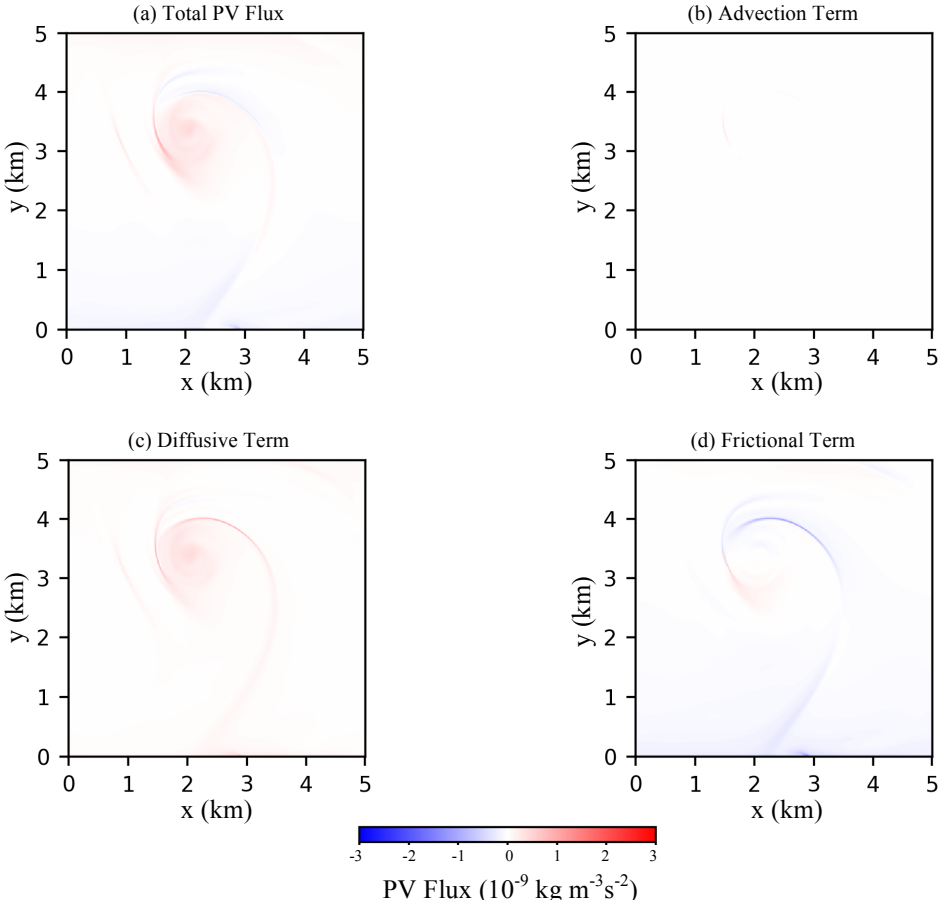

Figure 5.8: Total PV flux at the surface for Exp4E-CC at the (a) 12th hour, and its components contributed to the (b) advection term, (c) diffusional term, and (d) frictional term.

Similar to Fig 5.7a and Fig 5.4d, the total PV flux shown in Fig 5.8a is also consistent with the averaged PV field of near-surface layers in Fig. 5.4e. Fig 5.8 shows that the intense negative PV flux only appears at the front on the upwind side of the eddy, because all the three terms introduce negative PV flux over it. The PV flux along the front on the north side of the east-west turning point is weak due to the compensation of the positive PV flux and negative PV flux introduced by the frictional term (Fig. 5.8c) and diffusive term (Fig. 5.8d), respectively. The

negative PV flux over the eddy in both Figs. 5.7a and 5.8a are primarily introduced by the diffusive term.

In short, the negative injection at the air-sea interface is shown to be the cause of negative accumulation in the near-surface layers. Diagnosis of the PV flux shows that the superimposition and compensation of PV flux fields contributed by the advection term, diffusive term and frictional term result in an intense negative PV injection over the region where front intensification occurs. The strong vertical velocity associated with the intensified front transports the accumulated negative PV to deeper layers.

5.1.2 Submesoscale Front Breaking

Although the submesoscale front intensification has been diagnosed in the last section resulting from negative PV accumulation at the near-surface layers, it is not the only manner of evolution for a submesoscale front during the negative PV accumulation. Fig. 5.9 shows the surface Ro fields at the 24th hour and the 40th hour in Exp4W-CC. The submesoscale front intensification revealed in Figs. 5.1a-c continues to make a stronger front in Fig. 5.9a at the 24th hour. However, the front is broken up into several segments at the 40th hour, shown in Fig. 5.9b.

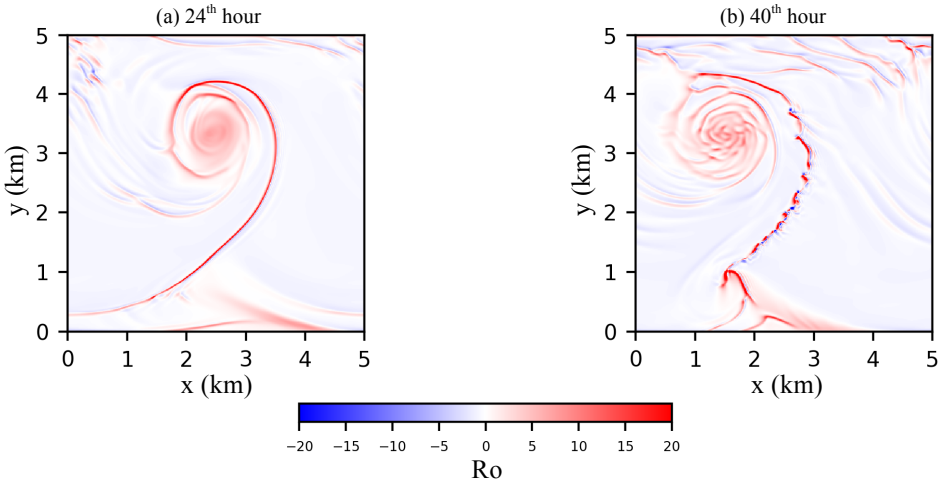

Figure 5.9: Surface Ro field of Exp4W-CC at the (a) 24th hour and (b) 40th hour.

Comparing the averaged net vertical PV profiles of Exp4W-CC at the 24th hour and 40th hour (indicated by the solid black lines in Fig. 5.2a), no significant increase of negative PV is recognized in the near-surface layers between the surface and a 26-m depth. However, the

positive PV beneath 26 m at the 40th hour is smaller than at the 24th hour. The vertical profiles of averaged positive PV in Fig. 5.2b reveal that near-surface positive PV is very weak at the 24th hour, but strengthens at the 40th hour when positive PV is pumped up to the surface around the 36th hour. Meanwhile, the vertical profiles of averaged negative PV in Fig. 5.2b shows that a significant amount of negative PV is transported to the near-bottom layers around the 36th hour. These remarkable differences in averaged PV profiles at the 24th hour and the 40th hour might be attributed to the different PV transports associated with the intensified and broken fronts. To further explore the relationship between the front breaking and the PV fields, the PV flux at the ocean surface is diagnosed for Exp4W-CC at the 24th hour and 40th hour.

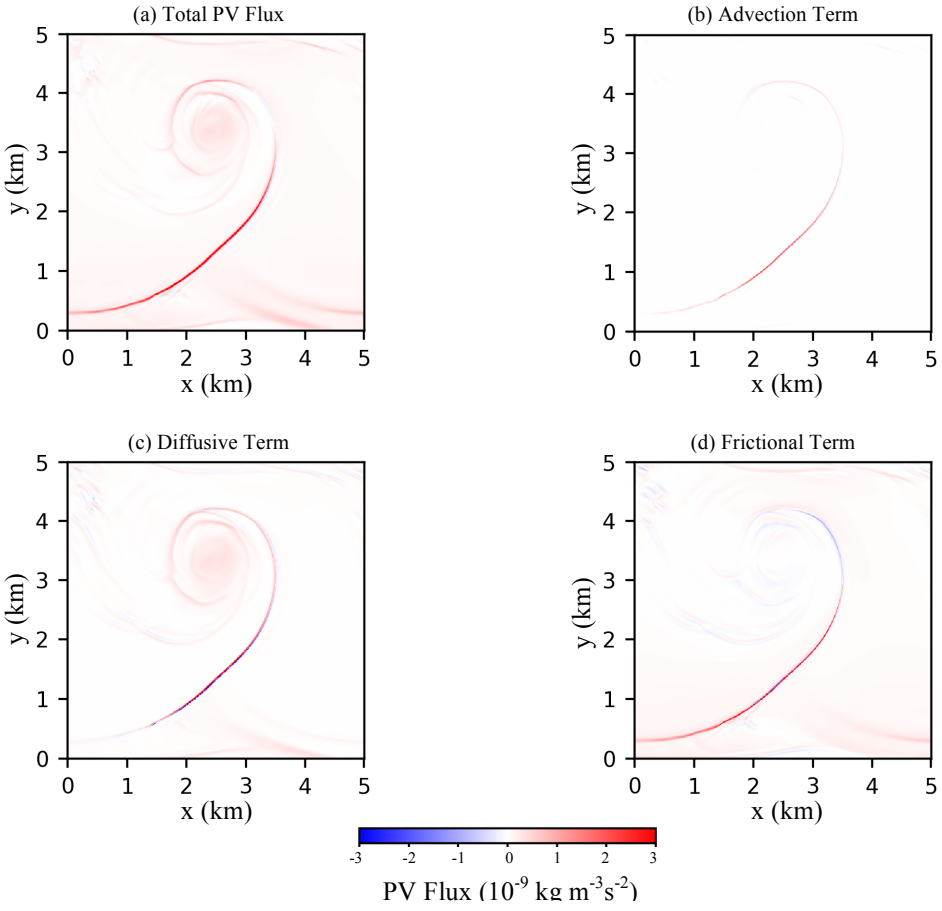

Figure 5.10: Total PV flux at surface for Exp4W-CC at the (a) 24th hour, and its components contributed to the (b) advection term, (c) diffusional term, and (d) frictional term.

The total PV flux and its three components for Exp4W-CC at the 24th hour are shown in Fig. 5.10. Although a positive PV injection on the edges of the south portion of the front is

introduced by the diffusive term (Fig. 5.10c) and the frictional term (Figs. 5.10d), the intense total negative PV injection into the ocean represented by a strong positive PV flux appears along the submesoscale front portion to the south of the east-west turning point. Similar to what is seen in Fig. 5.7, the weak PV flux on the front portion to the north of the east-west turning point is caused by the compensation of positive and negative PV fluxes introduced by the diffusive term and the frictional term, respectively. The surface PV flux shown in Fig. 5.10a indicates that a significant amount of negative PV is injected into the ocean at the 24th hour in Exp4W-CC.

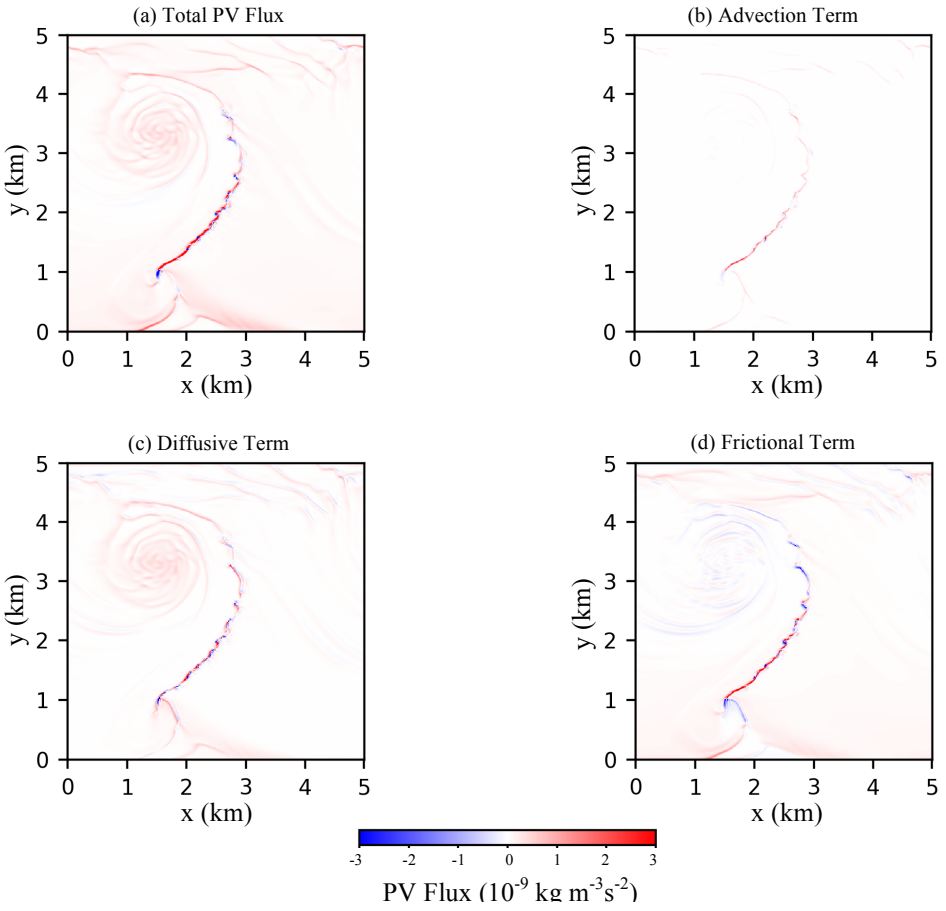

Figure 5.11: Total PV flux at the surface for Exp4W-CC at the (a) 40th hour, and its components contributed to the (b) advection term, (c) diffusional term, and (d) frictional term.

The total surface PV flux for Exp4W-CC at the 40th hour is shown in Fig. 5.11a, in which significant amount of positive PV injection is recognized around the west-east front turning points while the rest of the domain is still injected with negative PV. Since the front is already broken into several segments, the magnitude and sign of PV flux along these segments attributed

to the advection term, diffusive term, and frictional term become complicated as well (Fig. 5.11b-d). A comparison of Figs. 5.10a and 5.11a, shows that the difference in surface PV flux at the 24th hour and 40th hour in Exp4W-CC is not only reflected on the discrepancy in their structure, it is also embodied in the appearance of intense negative surface PV flux (positive PV injection to the ocean) on the ocean surface at the 40th hour, which is not present on the ocean surface at the 24th hour. Additionally, both Figs. 5.10a and 5.11a reveal a negative PV injection to the ocean, while Fig. 5.2a shows that the averaged negative PV in the near-surface layers between the surface and 26 m depth is not significantly increased between the 24th hour and 40th hour. Fig. 5.2c also shows that more negative PV is transported to the near-bottom layers during this timeframe. This leads to the question of how the negative PV injected from the air-sea interface is transported to the bottom layers.

Figs. 5.12a and 5.12b show the vertical velocity averaged along the vertical direction at the 24th hour and 40th hour in Exp4W-CC. A positive (upward) vertical velocity band is paralleled with a negative vertical velocity band along the front in Fig. 5.12a, while the regions of averaged positive and negative vertical velocity in Fig. 5.12b are co-mingled. To further probe the fields of vertical velocity beneath the intensified and broken front, transect views of vertical velocity averaged along x direction are pictured in Fig. 5.12c-f. Only the vertical velocities within the magenta box in Figs. 5.12a and 5.12b are averaged in order to highlight the front domain. In addition, positive velocity and negative vertical velocity are independently averaged to avoid compensation between them. Both the averaged positive velocity (Fig. 5.12c) and averaged negative velocity (Fig. 5.12e) beneath the intensified front at the 24th hour are uniformly distributed in the y direction, and the strong vertical velocities close to 0.01 ms^{-1} are mostly found in the upper ocean layers above 60 m. However, Figs. 5.12d and 5.12f show intense vertical velocities beneath the broken front at the 40th hour are constraint in narrow bands (symmetric instability cells) vertically penetrating through the entire layer. Therefore, it can be speculated that negative PV at the near-surface layers can be transported through the bottom by the symmetric cells under the broken front, and it can only be transported to layers above 60 m by the frontal secondary circulation under the intensified front at the 24th hour. To verify this, the PV fields vertically averaged from the surface to 10 m for Exp4W-CC at the 24th hour and 40th hour are plotted in Figs. 5.13a and 5.13b. They indicate that intense negative PV appears beneath the intensified and broken fronts in the near-surface layers. The PV fields vertically averaged

from 60 m to 80 m at the 24th hour and 40th hour are shown in Figs. 5.13c and 5.13d, respectively. The distributions of negative PV in Figs. 5.13c and 5.13d confirms that much more negative PV is transported into the deep layers by the symmetric cells beneath the broken front at the 40th hour than is transported by the frontal secondary circulation at the 24th hour.

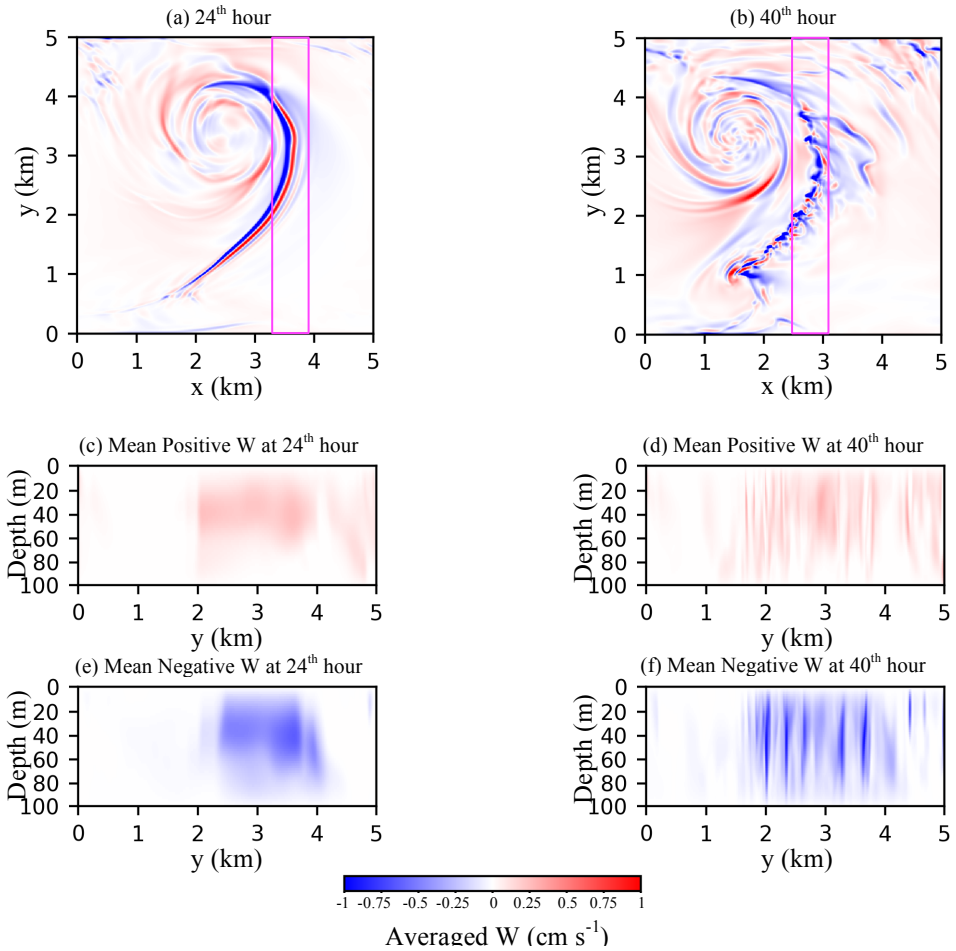

Figure 5.12: Averaged vertical velocity of Exp4W-CC at the (a) 24th hour and (b) 40th hour along vertical direction. Averaged positive vertical velocity (shown in c and d), and averaged negative vertical velocity (shown in e and f), for the subdomain in the magenta box along x direction in (a) and (b).

Hence, the negative PV accumulation at the near-surface layers not only can introduce front intensification to propagate negative PV to deeper layers; when the front is intensified to a degree, it can also break into several segments and initiate symmetric instability. The much stronger vertical velocity associated with the symmetric cells can penetrate the entire vertical layer and transport negative PV from upper layers to the bottom of the mixed layer.

When forced by westward and eastward 8 ms-1 winds in Exp8W-CC and Exp8E-CC, the negative PV injections on the submesoscale front are greater than those in Exp4W-CC and Exp4E-CC. Therefore, as shown in Fig. 5.14, the front intensifications and breakings also take place on the upwind side of the eddy, but at a faster rate.

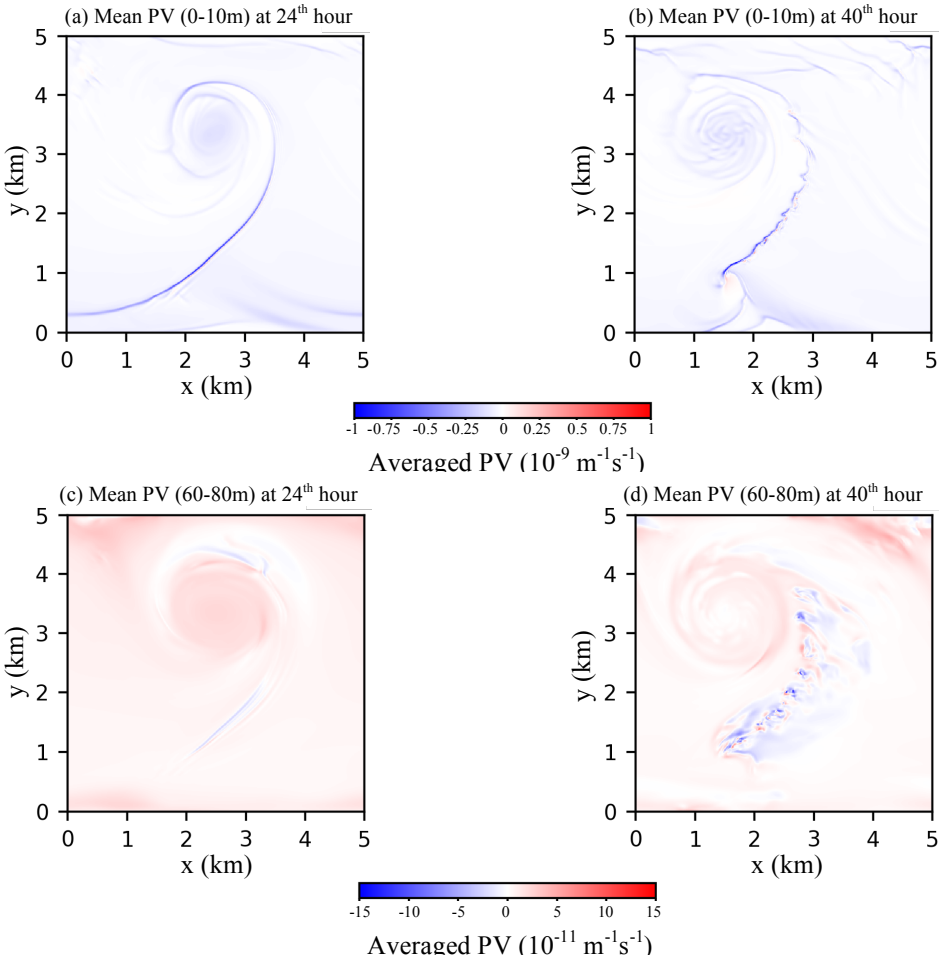

Figure 5.13: Averaged PV of Exp4W-CC at the 24th hour and 40th hour along vertical direction for layer between (a) surface and (b) 10-m depth, and for layer between (c) 60-m depth and (d) 80-m depths.

5.2 Effects of Submesoscale-modified Air-sea Turbulent Fluxes

Since submesoscale evolution is closely related to the PV flux at the air-sea interface, the influence of air-sea turbulent fluxes on submesoscale evolution are often reflected in the effect of air-sea turbulent fluxes on the surface PV flux. Findings in Chapter 4 reveal that both heat and momentum exchanges at the air-sea interface are significantly dependent on the choice of air-sea

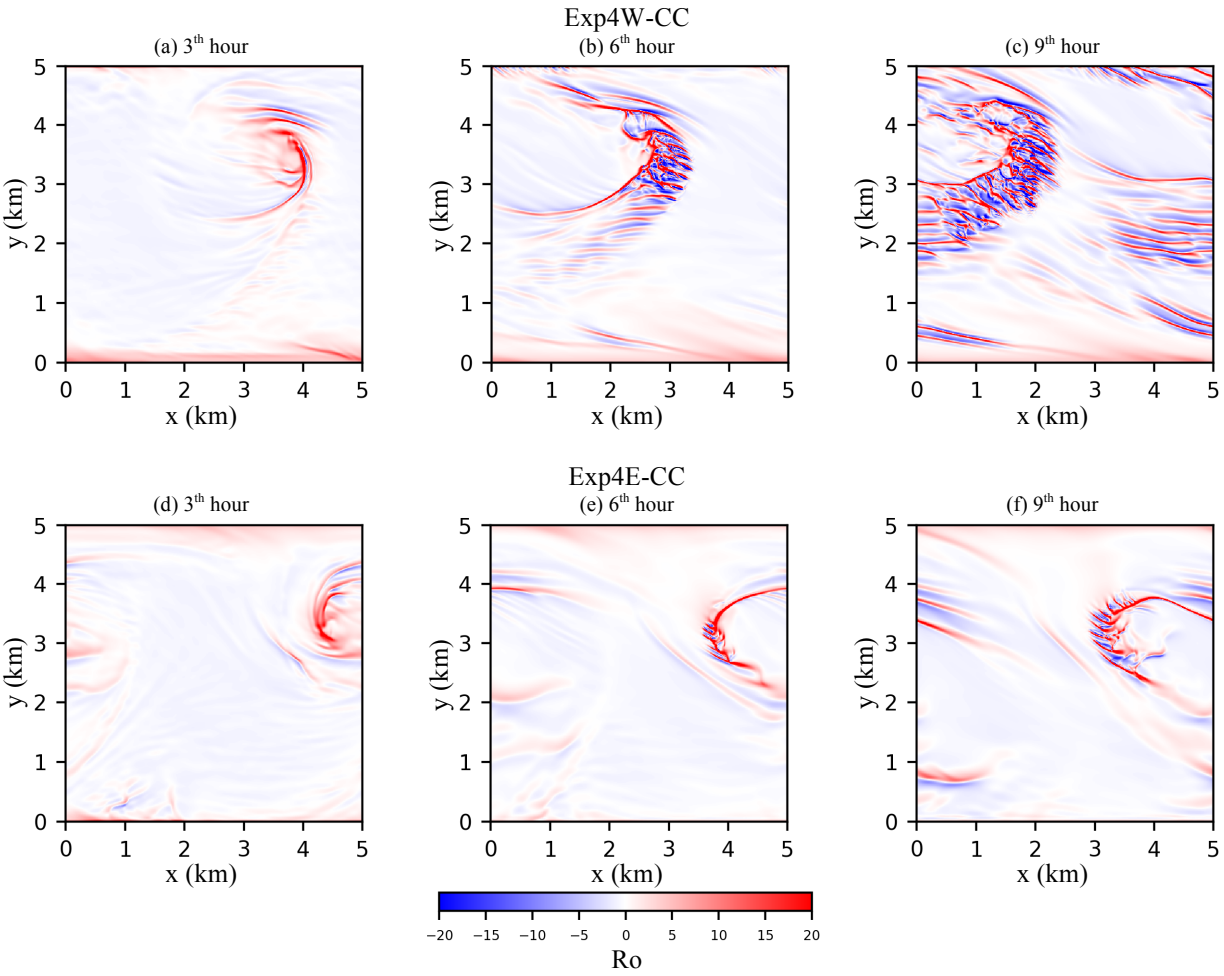

Figure 5.14: Surface Ro field of Exp8W-CC at the (a) 3rd hour, (b) 6th hour, and (c) 9th hour; and of Exp8E-CC at the (d) 3rd hour, (e) 6th hour, and (f) 9th hour).

interface are significantly dependent on the choice of air-sea scheme, which decides if the surface current coupling and/or the two-way thermodynamic coupling are switched on. In this section, the differences in surface PV flux introduced by different air-sea schemes are quantitatively assessed. In addition, other dynamical indicators, such as the RMS of vertical velocity and vertical transport of buoyancy, are diagnosed to examine the responses of the ocean to different air-sea turbulent fluxes.

5.2.1 Variance of PV Flux at the Surface

Fig. 5.15a shows a time series of averaged total PV fluxes at the ocean surface in the Exp4W experiments. At the start of the experiments, the PV flux difference between Exp4W-UN

and Exp4W-CN, as well as the difference between Exp4W-UC and Exp4W-CC, is zero. This means that only the surface current coupling introduces PV flux differences among the Exp4W-experiments when it is initially forced by wind. Also, the initial PV flux differences are generated by both the diffusive term (Fig. 5.15c) and the frictional term (Fig. 5.15d). As time elapses, the averaged PV flux difference between Exp4W-UN and Exp4W-CN increases, and a similar increase can be seen between Exp4W-UC and Exp4W-CC. Thus, the two-way thermodynamic coupling is shown to be an important factor influencing the surface PV flux. After the 36th hour, the thermodynamically coupled Exp4W-CN and Exp4W-CC have greater positive PV fluxes at the surface than the thermodynamically uncoupled Exp4W-UN and Exp4W-UC. This implies that the difference in averaged surface PV flux can be primarily attributed to thermodynamic coupling rather than surface current coupling.

Figs. 5.15c reveals that the two-way thermodynamic coupling dominates the surface PV flux introduced by the diffusive term, and the diffusive-introduced PV flux difference between thermodynamically coupled and uncoupled experiments increases with time. In Fig. 5.15d, the surface PV flux introduced by the frictional term is more dependent on surface current coupling. The frictional-introduced surface PV flux difference between experiments that consider and do not considered surface current effects decreases with time.

Based on Figs. 5.15, it can be concluded that since the surface PV flux introduced by advection term is small, the total surface PV flux is primarily contributed by the diffusive term and the frictional term. The PV flux contribution of the diffusive term is more dependent on two-way thermodynamic coupling, while the PV flux contribution of the frictional term is more reliant on the inclusion of surface current in the air-sea turbulent flux bulk algorithm. It confirms that the total PV flux at the ocean surface varies according to the choice of different air-sea schemes.

5.2.2 Variance of Vertical Velocity and Transports

Since differences in PV flux on the ocean surface are recognized in the experiments forced by the same wind but with different air-sea schemes, the next step is to inject different amount of PV into the ocean fields of these experiments. Section 5.1 summarizes how the evolution of submesoscale processes, such as front intensification, front breaking, and development of symmetric instability, are closely related to the PV budget of the ocean and that

submesoscale processes are also associated with strong vertical velocity fields. Therefore, the evolution of a vertical velocity field can be considered as an indicator for the oceanic submesoscale dynamics to exam how the ocean respond to the different fields of air-sea turbulent fluxes.

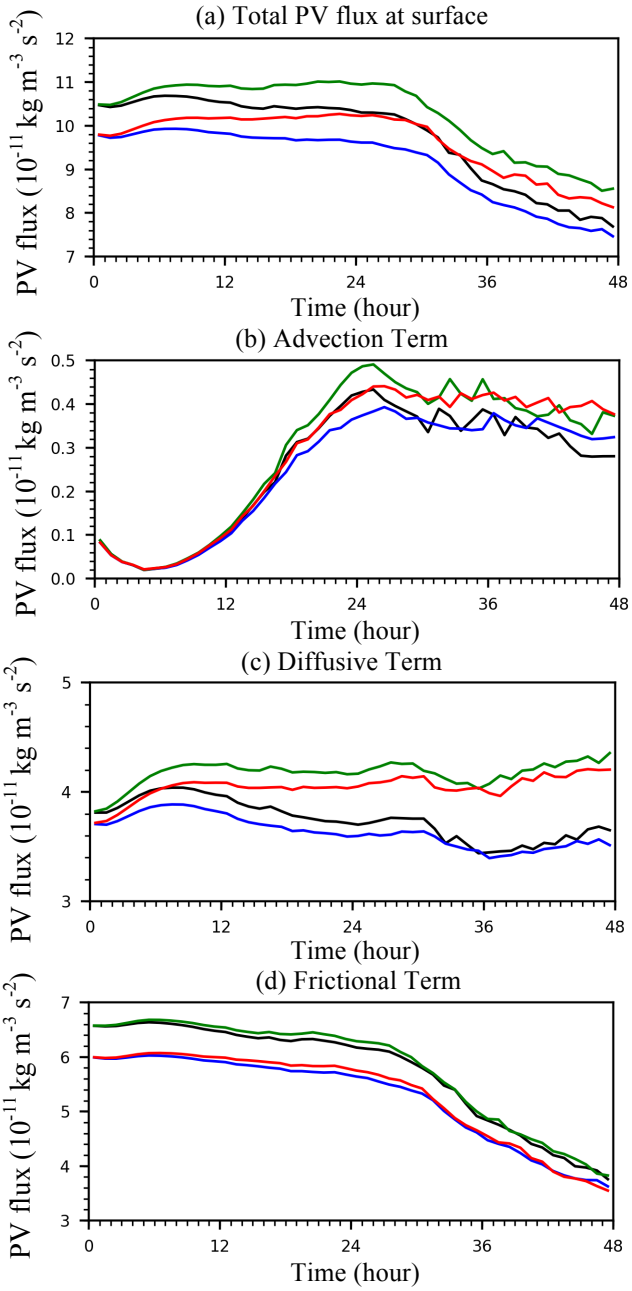

Figure 5.15: Time series of an (a) averaged total PV flux and its (b) advection term, (c) diffusional term, and (d) frictional term for the surface layer in Exp4W experiments. Black: Exp4W-UN, Blue: Exp4W-UC, Green: Exp4W-CN, Red: Exp4W-CC.

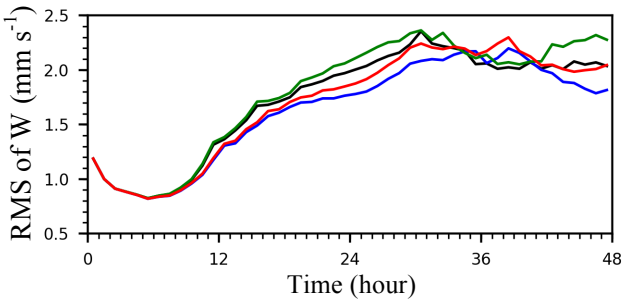

Figure 5.16: Time series of RMS of w in Exp4W experiments. Black: Exp4W-UN, Blue: Exp4W-UC, Green: Exp4W-CN. Red: Exp4W-CC.

The RMS time series of vertical velocity in the Exp4W- experiments are shown in Fig. 5.16. A significant increase in vertical velocity between the 6th hour and the 34th hour is consistent with the front intensification during this period. When the front breaking takes place after the 34th hour, the RMSs of vertical velocity are maintained at a large value while the symmetric instability is initiated. While the general patterns of the evolution of RMS of vertical velocity are similar among all of the Exp4W experiments, a prominent discrepancy is also apparent. At the 24th hour, the largest value of the RMS of vertical velocity appears in Exp4W-CN, and the second and third largest values appear in Exp4W-UN and Exp4W-CC; the smallest RMS of vertical velocity is seen in Exp4W-UC. The discrepancy in the RMSs of vertical velocity among the experiments of different air-sea schemes is speculated to be associated with different vertical transport of tracers. Therefore, the vertical transport of buoyancy is also examined in this study also as it affects the stratification of the ocean field.

The vertical transports of buoyancy in the Exp4W- experiments are shown in Fig. 5.17b. Similar to Fig. 5.16, Fig. 5.17b reveals that the general patterns of the evolution of vertical transport of buoyancy in the Exp4W- experiments are similar to each other, but a significant discrepancy is also recognized among the evolution. The vertical transports of buoyancy for other wind forcing experiments are also shown in Fig. 5.17. Prominent discrepancies of buoyancy vertical transport among the experiments with different air-sea schemes are also found in Figs. 5.17c and 5.17f. On the other hand, no significant discrepancy of buoyancy vertical transport among experiments with different air-sea schemes is shown in Figs. 5.17a, 5.17d, and 5.17e. The discrepancies of buoyancy vertical transport revealed in Figs. 5.17b, 5.17c, and 5.17f are also reflected by the differences in the surface Ro evolution of the Exp4W, Exp8W, and Exp8E experiments, respectively.

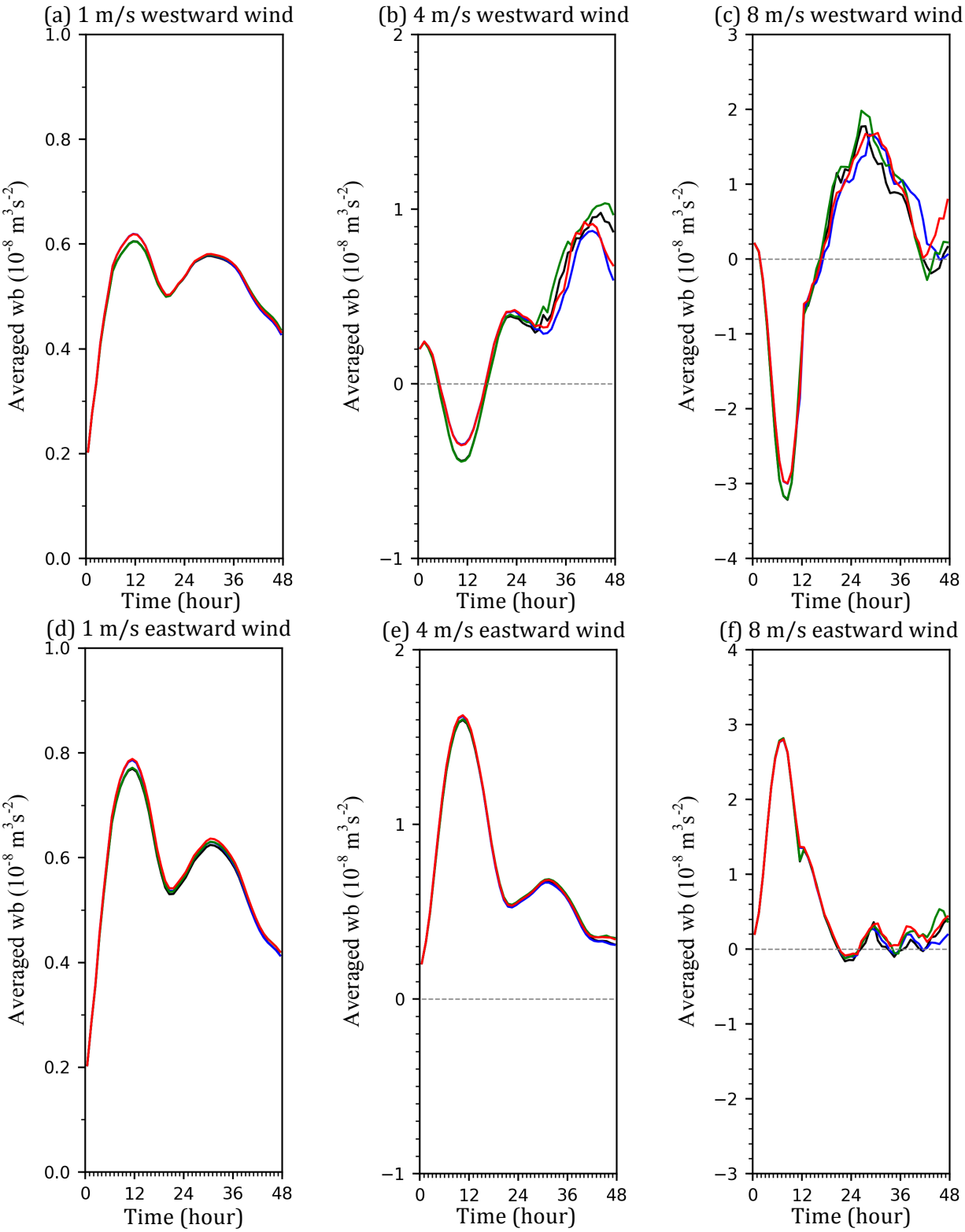

Figure 5.17: Time series of averaged vertical buoyancy transport for all wind forcing cases. Model with air-sea schemes of thermodynamically uncoupled, surface current coupling switched on (black) and off (blue). Model with air-sea scheme of thermodynamically coupled, surface current coupling switched on (green) and off (red).

In summary, oceanic submesoscale processes can modify the wind stress and turbulent heat fluxes at the air-sea interface, and different fields of air-sea momentum and heat fluxes can be generated in experiments with different air-sea schemes. These different air-sea turbulent fluxes can also interact with the submesoscale surface processes to produce a discrepancy of surface PV flux in these experiments. As a result, the submesoscale processes in these experiments with different air-sea schemes evolve differently from each other. Dynamical indicators of the RMS of vertical velocity and vertical transport of buoyancy also confirm that the ocean field evolves differently when forced by different air-sea turbulent fluxes.

CHAPTER 6

SUMMARY AND DISCUSSION

Wind stress and turbulent heat flux at the air-sea interface play a crucial role in driving ocean circulations on spatial scales ranging from global to mesoscale. The significance of surface current coupling and atmosphere-ocean coupling to air-sea interaction in the oceanic mesoscale regime have been recognized in previous works and are areas of current investigation. The richness of submesoscale processes in the ocean that has been revealed in high-resolution numerical models and observations in recent years motivates the focus of this dissertation on the two-way feedback between the air-sea turbulent fluxes and the submesoscale processes. It is argued that both wind stress field and turbulent heat fluxes are significantly influenced by submesoscale structures at the ocean surface. In addition, the submesoscale-modified air-sea turbulent fluxes can interact with the ocean surface to affect the evolution of the submesoscale processes.

Returning to the questions addressed in the first chapter of this study, the results presented in Chapters 3-5 provide answers to understand the two-way feedback mechanisms between the wind stress field and the submesoscale processes. The general description of the model results discussed in Chapter 3 confirm that the magnitude and direction of wind are important factors influencing the evolution of submesoscale eddies, fronts, and symmetric instability surface bands. Symmetric instabilities are generated in the oceanic mixed layer by both uniformly distributed westward wind and eastward wind forcing at 8 ms^{-1}. Submesoscale front intensification and breaking are revealed in experiments forced by 4 ms^{-1} westward winds, and the submesoscale front breaking initiates the symmetric instability. In each wind experiment, four air-sea schemes are implemented to examine the consequences of surface current coupling and thermodynamic coupling in an atmospheric boundary layer model. The distinct differences in submesoscale processes among the same high-speed wind (i.e., 4 ms^{-1} and 8 ms^{-1}) experiments of different air-sea schemes argue for significant influences of surface current coupling and thermodynamic coupling on submesoscale air-sea interaction and upper ocean dynamics.

In Chapter 4, the positive linear relationship between wind stress curl/divergence and crosswind/downwind SST gradient valid in mesoscale regime (Chelton et al., 2004) is examined over ocean fields of submesoscale frontal, eddy, and symmetric instability surface bands. When

the surface current coupling is switched off, positive linear relationships between wind stress curl and crosswind SST gradient are found over the submesoscale eddy and symmetric instability surface bands. There is also a positive correlation between the wind stress curl and crosswind SST gradient over submesoscale fronts, but it appears to be a two-branch-shape positive correlation instead of a simple linear relationship. The large SST variance across the submesoscale front making different wind stress adjustments on the two sides of the front is considered to be the cause for the two-branch shape.

When the surface current coupling is activated, the wind stress curl varies significantly corresponding to the strong submesoscale surface current vorticity. The crosswind SST gradient effect on wind stress curl becomes secondary to the influence of surface current curl on wind stress curl, consistent with the mesoscale study of Chelton et al. (2004). Because the crosswind SST gradient introduces a wind stress curl of the same sign, while the surface current curl generates a wind stress curl with the opposite sign (Gaube et al., 2015), the relationship between the crosswind SST gradient and the surface current curl determines whether the wind stress curl introduced by crosswind SST gradient to compensates or reinforces the wind stress produced by the surface current curl. Over the submesoscale front, the surface current curl is linearly and positively correlated with the crosswind SST gradient. Thus, the wind stress curl is negatively correlated with the crosswind SST gradient and the wind stress curl purely introduced by the crosswind SST gradient compensates the wind stress curl purely generated by the surface current curl. Over the submesoscale eddy, there is no clear linear relationship between the surface current curl and the crosswind SST gradient. Therefore, the correlation between the wind stress curl and crosswind SST gradient is not prominent. In the subdomain filled with symmetric instability surface bands, the surface current curl is negatively correlated with the crosswind SST gradient, which leads to a positive relationship between wind stress curl and crosswind SST gradient. In such cases, the wind stress curl purely introduced by the crosswind SST gradient is superimposed on the wind stress curl generated by the surface current curl. Compared with the positive relationship between the wind stress curl and the crosswind SST gradient in mesoscale regime (Chelton et al., 2004), the wind stress curl field in the submesoscale regime primarily depends on the surface current curl field, which is much stronger than the surface current curl field in mesoscale regime.

In this study, the relationship between wind stress divergence and downwind SST gradient over the submesoscale structures also confirms that the surface current divergence, which is much greater than what is seen in the mesoscale regime, is the primarily dictator of the wind stress divergence. Similar to the relationship between wind stress curl and crosswind SST gradient, the relationship between wind stress divergence and downwind SST gradient is depends most on the relationship between surface current divergence and the downwind SST gradient.

In experiments with surface current coupling deactivated, the two-way thermodynamic coupling helps to attenuate the magnitudes of coupling coefficients, which is the rate of wind stress curl/divergence changing with respect to the crosswind/downwind SST gradient. The average wind stress curl over the model domain is of the same magnitude as those in the mesoscale field. However, the magnitudes of positive and negative wind stress curl are much greater than the magnitude of the averaged wind stress curl. This result implies that a richness of positive and negative wind stress curl revealed in the submesoscale-resolved model can be ignored in a coarser mesoscale-resolved model. Since, according to Ekman theory, wind stress curl is closely associated with vertical, further research is needed to determine the influence of the strong wind stress curl on Ekman pumping in the submesoscale regime.

When both thermodynamic coupling and surface current coupling are switched off, the coupling coefficients describing the relationships between wind stress curl/divergence and the crosswind/downwind SST gradient are related to the strength of the forcing wind. The coupling coefficient is greater with increasing wind magnitude, but it is neither a linear nor a quadratic relationship, as is found in the mesoscale regime (Spall, 2007). At wind speeds between 2-6 ms^{-1}, the rate measuring coupling coefficient change with increasing wind is greater than for the wind speed range beyond 8 ms^{-1}. Direction of the wind does not appear to be a factor affecting the coupling coefficient magnitude.

The time series of averaged sensible and latent heat flux over the domain shows that thermodynamic coupling plays a primary role influencing the sensible/latent heat flux in the submesoscale regime. This suggest that the magnitudes of sensible and latent heat flux are more closely related to the atmospheric temperature sensitivity to the thermodynamic coupling rather than the surface current coupling. The influences of surface current on both sensible and latent

heat flux are noticeable, but the influence on sensible heat flux is much weaker than the influence on latent heat flux.

To investigate the influence of submesoscale-modified wind stress on the evolution of submesoscale processes, the Chapter 5 diagnoses the ocean's dynamical evolution from the perspective of PV. The results indicate that submesoscale front intensification is a result of negative PV accumulation at the surface and upper ocean layer. The source of negative PV is provided by interactions between the submesoscale features and air-sea fluxes of heat and momentum, consistent with the work of Wenegrat et al. (2018), and the intensified front associated with enhanced vertical velocity can transport the negative PV from the surface to deeper layers. Eventually, the intensified front breaks and initiates symmetric instabilities, in which the vertical velocity gets even stronger and penetrates the entire vertical layer. Therefore, the PV exchanges between the ocean surface and deeper layers are strengthened. It is also found that stronger wind forcing accelerates the evolution for symmetric instability along the submesoscale front.

When forced by the same wind, it is argued that both surface current coupling and thermodynamic coupling can influence the PV flux at the surface. Therefore, experiments with different air-sea schemes can introduce different PV injections to make the submesoscale processes evolve differently. The differences in submesoscale evolution are associated with varied vertical velocity and vertical transports (e.g. vertical buoyancy transport), which are more pronounced when frontal breaking (symmetric instability initialization) or symmetric instabilities are activated.

In summary, the following conclusions can be drawn from the present study:

1. The linear relationship between wind stress curl/divergence and crosswind/downwind SST gradients in the mesoscale is no longer valid in the submesoscale regime because strong surface current curl/divergence is the primary influence.
2. When the surface current coupling is switched off, the positive linear relationship between wind stress curl/divergence and crosswind/downwind SST gradients is still valid in the submesoscale regime, and their coupling coefficient is positively correlated with the strength of wind forcing.
3. The turbulent heat fluxes in the submesoscale regime are significantly influenced by both the surface current coupling and the thermodynamic coupling in the model.

4. Submesoscale processes (i.e., eddy, front, and symmetric instability surface bands) evolve differently under wind forces of different magnitudes and directions.
5. Although forced by the same wind, different settings of surface current coupling and thermodynamic coupling can change the PV flux at the ocean surface to make the submesoscale surface Ro field and its associated processes, such as vertical velocity and vertical buoyancy transport, evolve differently.

This research extends our knowledge of air-sea interaction over the submesoscale regime. It provides, for the first time, insight into how the wind stress and turbulent heat fluxes respond to specific submesoscale processes, and how these submesoscale processes evolve corresponding to changing wind stress and heat fluxes. The significance of surface current coupling and thermodynamic coupling are argued in the modeling of submesoscale air-sea interactions. One limitation of this study is that the wind-SST interaction (O'Neill et al., 2010; Small et al., 2008) is not resolved in the atmospheric boundary layer model. Therefore, further research implementing a fully two-way coupled (dynamic and thermodynamic) model is necessary to better simulate and understand the feedbacks between the oceanic submesoscale processes and the atmosphere. This will improve the fidelity of long-term climate projection, thereby bettering the principal scientific tool used to investigate the most pressing societal issue of our time related to climate change.

REFERENCES

Bachman, S. D., Taylor, J. R., Adams, K. A., & Hosegood, P. J. (2017). Mesoscale and Submesoscale Effects on Mixed Layer Depth in the Southern Ocean. *Journal of Physical Oceanography*, *47*(9), 2173–2188. https://doi.org/10.1175/JPO-D-17-0034.1

Boccaletti, G., Ferrari, R., & Fox-Kemper, B. (2007). Mixed Layer Instabilities and Restratification. *Journal of Physical Oceanography*, *37*(9), 2228–2250. https://doi.org/10.1175/JPO3101.1

Bourassa, M. A., Gille, S. T., Bitz, C., Carlson, D., Cerovecki, I., Clayson, C. A., et al. (2013). High-Latitude Ocean and Sea Ice Surface Fluxes: Challenges for Climate Research. *Bulletin of the American Meteorological Society*, *94*(3), 403–423. https://doi.org/10.1175/BAMS-D-11-00244.1

Brannigan, L., Marshall, D. P., Naveira-Garabato, A., & George Nurser, A. J. (2015). The seasonal cycle of submesoscale flows. *Ocean Modelling*, *92*, 69–84. https://doi.org/10.1016/j.ocemod.2015.05.002

Brannigan, L., Marshall, D. P., Naveira Garabato, A. C., George Nurser, A. J., & Kaiser, J. (2017). Submesoscale instabilities in mesoscale eddies. *Journal of Physical Oceanography*. https://doi.org/10.1175/JPO-D-16-0178.1

Brunke, M. A., Fairall, C. W., Zeng, X., Eymard, L., & Curry, J. A. (2003). Which Bulk Aerodynamic Algorithms are Least Problematic in Computing Ocean Surface Turbulent Fluxes? *Journal of Climate*, *16*(4), 619–635. https://doi.org/10.1175/1520-0442(2003)016<0619:WBAAAL>2.0.CO;2

Capet, X., McWilliams, J. C., Molemaker, M. J., & Shchepetkin, A. F. (2008). Mesoscale to Submesoscale Transition in the California Current System. Part I: Flow Structure, Eddy Flux, and Observational Tests. *Journal of Physical Oceanography*, *38*(1), 29–43. https://doi.org/10.1175/2007JPO3671.1

Charney, J. G. (1971). Geostrophic turbulence. *Journal of Atmospheric Sciences*, *28*, 1087–1095.

Chelton, D. B. (2004a). Satellite Measurements Reveal Persistent Small-Scale Features in Ocean Winds. *Science*, *303*(5660), 978–983. https://doi.org/10.1126/science.1091901

Chelton, D. B. (2004b). Satellite Measurements Reveal Persistent Small-Scale Features in Ocean Winds. *Science*, *303*(5660), 978–983. https://doi.org/10.1126/science.1091901

Chelton, Dudley B., Esbensen, S. K., Schlax, M. G., Thum, N., Freilich, M. H., Wentz, F. J., et al. (2001). Observations of Coupling between Surface Wind Stress and Sea Surface Temperature in the Eastern Tropical Pacific. *Journal of Climate*, *14*(7), 1479–1498. https://doi.org/10.1175/1520-0442(2001)014<1479:OOCBSW>2.0.CO;2

Chelton, Dudley B., Schlax, M. G., Freilich, M. H., & Milliff, R. F. (2004). Satellite measurements reveal persistent small-scale features in ocean winds. *Science*, *303*(5660), 978–983.

D'Asaro, E., Lee, C., Rainville, L., Harcourt, R., & Thomas, L. (2011). Enhanced Turbulence and Energy Dissipation at Ocean Fronts. *Science*, *332*(6027), 318–322. https://doi.org/10.1126/science.1201515

D'Asaro, E., Lee, C., Rainville, L., Harcourt, R., & Thomas, L. (n.d.). Enhanced Turbulence and Energy Dissipation at Ocean Fronts. *Science*, *332*(6027), 318–322. https://doi.org/10.1126/science.1201515

Dawe, J. T., & Thompson, L. (2006). Effect of ocean surface currents on wind stress, heat flux, and wind power input to the ocean. *Geophysical Research Letters*, *33*(9). https://doi.org/10.1029/2006GL025784

Deremble, B., Wienders, N., & Dewar, W. K. (2013). CheapAML: A Simple, Atmospheric Boundary Layer Model for Use in Ocean-Only Model Calculations. *Monthly Weather Review*, *141*(2), 809–821. https://doi.org/10.1175/MWR-D-11-00254.1

Dewar, W. K., & Flierl, G. R. (1987). Some Effects of the Wind on Rings. *Journal of Physical Oceanography*, *17*, 1653–1667. https://doi.org/10.1175/1520-0485(1987)017<1653:SEOTWO>2.0.CO;2

Duhaut, T. H. A., & Straub, D. N. (2006). Wind Stress Dependence on Ocean Surface Velocity: Implications for Mechanical Energy Input to Ocean Circulation. *Journal of Physical Oceanography*, *36*(2), 202–211. https://doi.org/10.1175/JPO2842.1

Elipot, S., Frajka-Williams, E., Hughes, C. W., Olhede, S., & Lankhorst, M. (2017). Observed Basin-Scale Response of the North Atlantic Meridional Overturning Circulation to Wind Stress Forcing. *Journal of Climate*, *30*(6), 2029–2054. https://doi.org/10.1175/JCLI-D-16-0664.1

Fairall, C. W., Bradley, E. F., Hare, J. E., Grachev, A. A., & Edson, J. B. (2003). Bulk Parameterization of Air–Sea Fluxes: Updates and Verification for the COARE Algorithm. *Journal of Climate*, *16*(4), 571–591. https://doi.org/10.1175/1520-0442(2003)016<0571:BPOASF>2.0.CO;2

Fox-Kemper, B., Ferrari, R., & Hallberg, R. (2008). Parameterization of Mixed Layer Eddies. Part I: Theory and Diagnosis. *Journal of Physical Oceanography*, *38*(6), 1145–1165. https://doi.org/10.1175/2007JPO3792.1

Gaube, P., Chelton, D. B., Samelson, R. M., Schlax, M. G., & O'Neill, L. W. (2015a). Satellite Observations of Mesoscale Eddy-Induced Ekman Pumping. *Journal of Physical Oceanography*, *45*(1), 104–132. https://doi.org/10.1175/JPO-D-14-0032.1

Gaube, P., Chelton, D. B., Samelson, R. M., Schlax, M. G., & O'Neill, L. W. (2015b). Satellite Observations of Mesoscale Eddy-Induced Ekman Pumping. *Journal of Physical Oceanography*, *45*(1), 104–132. https://doi.org/10.1175/JPO-D-14-0032.1

Gill, A. E. (1982). Atmosphere-Ocean Dynamics (p. 662). Academic Press.

Hamlington, P. E., Van Roekel, L. P., Fox-Kemper, B., Julien, K., & Chini, G. P. (2014). Langmuir–Submesoscale Interactions: Descriptive Analysis of Multiscale Frontal Spindown Simulations. *Journal of Physical Oceanography*, *44*(9), 2249–2272. https://doi.org/10.1175/JPO-D-13-0139.1

Huang, R. X. (2010). Ocean Circulation Wind-Driven and Thermohaline Processes (p. 185). Cambridge University Press.

Jochum, M., Murtugudde, R., Ferrari, R., & Malanotte-Rizzoli, P. (2005). The Impact of Horizontal Resolution on the Tropical Heat Budget in an Atlantic Ocean Model. *Journal of Climate*, *18*(6), 841–851. https://doi.org/10.1175/JCLI-3288.1

Kang, D., & Curchitser, E. N. (2015). Energetics of Eddy–Mean Flow Interactions in the Gulf Stream Region. *Journal of Physical Oceanography*, *45*(4), 1103–1120. https://doi.org/10.1175/JPO-D-14-0200.1

Kanzow, T., Cunningham, S. A., Johns, W. E., Hirschi, J. J.-M., Marotzke, J., Baringer, M. O., et al. (2010). Seasonal Variability of the Atlantic Meridional Overturning Circulation at 26.5°N. *Journal of Climate*, *23*(21), 5678–5698. https://doi.org/10.1175/2010JCLI3389.1

Kelly, K. A., Dickinson, S., McPhaden, M. J., & Johnson, G. C. (2001). Ocean currents evident in satellite wind data. *Geophysical Research Letters*, *28*(12), 2469–2472. https://doi.org/10.1029/2000GL012610

Klein, P., & Lapeyre, G. (2009). The Oceanic Vertical Pump Induced by Mesoscale and Submesoscale Turbulence. *Annual Review of Marine Science*, *1*(1), 351–375. https://doi.org/10.1146/annurev.marine.010908.163704

Lee, T., Waliser, D. E., Li, J.-L. F., Landerer, F. W., & Gierach, M. M. (2013). Evaluation of CMIP3 and CMIP5 Wind Stress Climatology Using Satellite Measurements and Atmospheric Reanalysis Products. *Journal of Climate*, *26*(16), 5810–5826. https://doi.org/10.1175/JCLI-D-12-00591.1

Lévy, M., Ferrari, R., Franks, P. J. S., Martin, A. P., & Rivière, P. (2012). Bringing physics to life at the submesoscale: FRONTIER. *Geophysical Research Letters*, *39*(14), n/a-n/a. https://doi.org/10.1029/2012GL052756

Ma, X., Jing, Z., Chang, P., Liu, X., Montuoro, R., Small, R. J., et al. (2016). Western boundary currents regulated by interaction between ocean eddies and the atmosphere. *Nature*, *535*(7613), 533–537. https://doi.org/10.1038/nature18640

Mahadevan, A. (2016). The Impact of Submesoscale Physics on Primary Productivity of Plankton. *Annual Review of Marine Science*, *8*(1), 161–184. https://doi.org/10.1146/annurev-marine-010814-015912

Maloney, E. D., & Chelton, D. B. (2006). An Assessment of the Sea Surface Temperature Influence on Surface Wind Stress in Numerical Weather Prediction and Climate Models. *Journal of Climate*, *19*(12), 2743–2762. https://doi.org/10.1175/JCLI3728.1

MARSHALL, J., & Nurser, A. J. G. (1992). Fluid dynamics of oceanic thermocline ventilation. *JOURNAL OF PHYSICAL OCEANOGRAPHY*, *22*, 583–595.

Marshall, J., Hill, C., Perelman, L., & Adcroft, A. (1997). Hydrostatic, quasi-hydrostatic, and nonhydrostatic ocean modeling. *Journal of Geophysical Research: Oceans*, *102*(C3), 5733–5752. https://doi.org/10.1029/96JC02776

MARSHALL, J., JAMOUS, D., & NILSSON, J. (2001). Entry, Flux, and Exit of Potential Vorticity in Ocean Circulation. *JOURNAL OF PHYSICAL OCEANOGRAPHY*, *31*, 13.

McDougall, T. J. (1988). Neutral surface potential vorticity. *Progress in Oceanography*, *20*, 185–221.

McWilliams, J. (2003). *Diagnostic force balance and its liimits, in Nonlinear Processes in Geophysical Fluid Dynamics*. Kluwer Academic Publishers.

McWilliams, J. C. (2016a). Submesoscale currents in the ocean. *Proceedings of the Royal Society A: Mathematical, Physical and Engineering Science*, *472*(2189), 20160117. https://doi.org/10.1098/rspa.2016.0117

McWilliams, J. C. (2016b). Submesoscale currents in the ocean. *Proceedings of the Royal Society A: Mathematical, Physical and Engineering Science*, *472*(2189), 20160117. https://doi.org/10.1098/rspa.2016.0117

McWilliams, J. C., Molemaker', M. J., & Yavneh, I. (2001). From Stirring to Mixing of Momentum: Cascades from Balanced Flows to Dissipation in the Oceanic Interior. *N Proceedings of the 12th 'Aha Huliko'a Hawai- Ian Winter Workshop, University of Hawaii*, 59–66.

Moore, G. W. K., & Renfrew, I. A. (2002). An Assessment of the Surface Turbulent Heat Fluxes from the NCEP–NCAR Reanalysis over the Western Boundary Currents. *Journal of Climate*, *15*(15), 2020–2037. https://doi.org/10.1175/1520-0442(2002)015<2020:AAOTST>2.0.CO;2

Oerder, V., Colas, F., Echevin, V., Masson, S., & Lemarié, F. (2018). Impacts of the Mesoscale Ocean-Atmosphere Coupling on the Peru-Chile Ocean Dynamics: The Current-Induced Wind Stress Modulation. *Journal of Geophysical Research: Oceans*, *123*(2), 812–833. https://doi.org/10.1002/2017JC013294

O'Neill, L. W., Esbensen, S. K., Thum, N., Samelson, R. M., & Chelton, D. B. (2010a). Dynamical Analysis of the Boundary Layer and Surface Wind Responses to Mesoscale SST Perturbations. *Journal of Climate*, *23*(3), 559–581. https://doi.org/10.1175/2009JCLI2662.1

O'Neill, L. W., Esbensen, S. K., Thum, N., Samelson, R. M., & Chelton, D. B. (2010b). Dynamical Analysis of the Boundary Layer and Surface Wind Responses to Mesoscale SST Perturbations. *Journal of Climate*, *23*(3), 559–581. https://doi.org/10.1175/2009JCLI2662.1

Parfitt, R., Czaja, A., Minobe, S., & Kuwano-Yoshida, A. (2016). The atmospheric frontal response to SST perturbations in the Gulf Stream region: FRONTAL RESPONSE TO SST PERTURBATIONS. *Geophysical Research Letters*, *43*(5), 2299–2306. https://doi.org/10.1002/2016GL067723

Parfitt, R., Czaja, A., & Kwon, Y.-O. (2017a). The impact of SST resolution change in the ERA-Interim reanalysis on wintertime Gulf Stream frontal air-sea interaction: SST Resolution Change in ERA-Interim. *Geophysical Research Letters*, *44*(7), 3246–3254. https://doi.org/10.1002/2017GL073028

Parfitt, R., Czaja, A., & Kwon, Y.-O. (2017b). The impact of SST resolution change in the ERA-Interim reanalysis on wintertime Gulf Stream frontal air-sea interaction: SST Resolution

Change in ERA-Interim. *Geophysical Research Letters*, *44*(7), 3246–3254. https://doi.org/10.1002/2017GL073028

Park, K.-A., Cornillon, P., & Codiga, D. L. (2006). Modification of surface winds near ocean fronts: Effects of Gulf Stream rings on scatterometer (QuikSCAT, NSCAT) wind observations. *Journal of Geophysical Research*, *111*(C3). https://doi.org/10.1029/2005JC003016

Qiu, B., & Chen, S. (2010). Eddy-mean flow interaction in the decadally modulating Kuroshio Extension system. *Deep Sea Research Part II: Topical Studies in Oceanography*, *57*(13–14), 1098–1110. https://doi.org/10.1016/j.dsr2.2008.11.036

Renault, L., McWilliams, J. C., & Penven, P. (2017). Modulation of the Agulhas Current Retroflection and Leakage by Oceanic Current Interaction with the Atmosphere in Coupled Simulations. *Journal of Physical Oceanography*, *47*(8), 2077–2100. https://doi.org/10.1175/JPO-D-16-0168.1

Rhines, P. B. (1986). Vorticity Dynamics of the Oceanic General Circulation. *Annual Review of Fluid Mechanics*, *18*, 433–497.

Risien, C. M., & Chelton, D. B. (2008). A Global Climatology of Surface Wind and Wind Stress Fields from Eight Years of QuikSCAT Scatterometer Data. *Journal of Physical Oceanography*, *38*(11), 2379–2413. https://doi.org/10.1175/2008JPO3881.1

Roberts, J. B., Robertson, F. R., Clayson, C. A., & Bosilovich, M. G. (2012). Characterization of Turbulent Latent and Sensible Heat Flux Exchange between the Atmosphere and Ocean in MERRA. *Journal of Climate*, *25*(3), 821–838. https://doi.org/10.1175/JCLI-D-11-00029.1

Rogers, D. P. (1995). Air-sea interaction: Connecting the ocean and atmosphere. *Reviews of Geophysics*, *33*(S2), 1377–1383. https://doi.org/10.1029/95RG00255

Rosso, I., Hogg, A. M., Kiss, A. E., & Gayen, B. (2015). Topographic influence on submesoscale dynamics in the Southern Ocean. *Geophysical Research Letters*, *42*(4), 1139–1147. https://doi.org/10.1002/2014GL062720

Scott, R. B., & Arbic, B. K. (2007). Spectral Energy Fluxes in Geostrophic Turbulence: Implications for Ocean Energetics. *Journal of Physical Oceanography*, *37*(3), 673–688. https://doi.org/10.1175/JPO3027.1

Seager, R., Blumenthal, B., & Kushnir, Y. (1995). An Advective Atmospheric Mixed Layer Model for Ocean Modeling Purposes: Global Simulation of Surface Hear FLuxes. *JOURNAL OF CLIMATE*, *8*, 1951–1964.

Small, R. Justin, Xie, S.-P., Wang, Y., Esbensen, S. K., & Vickers, D. (2005). Numerical Simulation of Boundary Layer Structure and Cross-Equatorial Flow in the Eastern Pacific*. *Journal of the Atmospheric Sciences*, *62*(6), 1812–1830. https://doi.org/10.1175/JAS3433.1

Small, R.J., deSzoeke, S. P., Xie, S. P., O'Neill, L., Seo, H., Song, Q., et al. (2008a). Air–sea interaction over ocean fronts and eddies. *Dynamics of Atmospheres and Oceans*, *45*(3–4), 274–319. https://doi.org/10.1016/j.dynatmoce.2008.01.001

Small, R.J., deSzoeke, S. P., Xie, S. P., O'Neill, L., Seo, H., Song, Q., et al. (2008b). Air–sea interaction over ocean fronts and eddies. *Dynamics of Atmospheres and Oceans*, *45*(3–4), 274–319. https://doi.org/10.1016/j.dynatmoce.2008.01.001

Spall, M. A. (2007a). Midlatitude Wind Stress–Sea Surface Temperature Coupling in the Vicinity of Oceanic Fronts. *Journal of Climate*, *20*(15), 3785–3801. https://doi.org/10.1175/JCLI4234.1

Spall, M. A. (2007b). Midlatitude Wind Stress–Sea Surface Temperature Coupling in the Vicinity of Oceanic Fronts. *Journal of Climate*, *20*(15), 3785–3801. https://doi.org/10.1175/JCLI4234.1

Stamper, M. A., & Taylor, J. R. (2017). The transition from symmetric to baroclinic instability in the Eady model. *Ocean Dynamics*, *67*(1), 65–80. https://doi.org/10.1007/s10236-016-1011-6

Stone, P. (1966). On non-geostrophic baroclinic stability, *23*, 390–400.

Swallow, J. C. (1971). The Aries Current Measurements in the Western North Atlantic. *Philosophical Transactions of the Royal Society A: Mathematical, Physical and Engineering Sciences*, *270*(1206), 451–460. https://doi.org/10.1098/rsta.1971.0084

Thomas, L., & Ferrari, R. (2008). Friction, Frontogenesis, and the Stratification of the Surface Mixed Layer. *Journal of Physical Oceanography*, *38*(11), 2501–2518. https://doi.org/10.1175/2008JPO3797.1

Thomas, L. N. (2005). Destruction of Potential Vorticity by Winds. *Journal of Physical Oceanography*, *35*(12), 2457–2466. https://doi.org/10.1175/JPO2830.1

Thomas, L. N., & Lee, C. M. (2005). Intensification of ocean fronts by down-front winds. *Journal of Physical Oceanography*, *35*(6), 1086–1102.

Thomas, L. N., Tandon, A., & Mahadevan, A. (2007). Submesoscale processes and dynamics. In M. W. Hecht & H. Hasumi (Eds.), *Geophysical Monograph Series* (Vol. 177, pp. 17–38). Washington, D. C.: American Geophysical Union. https://doi.org/10.1029/177GM04

Thomas, L. N., Taylor, J. R., Ferrari, R., & Joyce, T. M. (2013). Symmetric instability in the Gulf Stream. *Deep Sea Research Part II: Topical Studies in Oceanography*, *91*, 96–110. https://doi.org/10.1016/j.dsr2.2013.02.025

Townsend, T. L., Hurlburt, H. E., & Hogan, P. J. (2000). Modeled Sverdrup flow in the North Atlantic from 11 different wind stress climatologies. *Dynamics of Atmospheres and Oceans*, *32*(3–4), 373–417. https://doi.org/10.1016/S0377-0265(00)00052-X

Wallace, J. M., Mitchell, T. P., & Deser, C. (1989). The Influence of Sea-Surface Temperature on Surface Wind in the Eastern Equatorial Pacific: Seasonal and Interannual Variability. *Journal of Climate*, *2*(12), 1492–1499. https://doi.org/10.1175/1520-0442(1989)002<1492:TIOSST>2.0.CO;2.

Wallace, J. M., Mitchell, T. P., & Deser, C. (n.d.). The Influence of Sea-Surface Temperature on Surface Wind in the Eastern Equatorial Pacific: Seasonal and Interannual Variability. *JOURNAL OF CLIMATE*, *1*(12), 1492–1499. https://doi.org/10.1175/1520-0442(1989)002<1492:TIOSST>2.0.CO;2

Walsh, K. J. E., Camargo, S. J., Vecchi, G. A., Daloz, A. S., Elsner, J., Emanuel, K., et al. (2015). Hurricanes and Climate: The U.S. CLIVAR Working Group on Hurricanes. *Bulletin of the American Meteorological Society*, *96*(6), 997–1017. https://doi.org/10.1175/BAMS-D-13-00242.1

Wenegrat, J. O., Thomas, L. N., Gula, J., & McWilliams, J. C. (2018a). Effects of the Submesoscale on the Potential Vorticity Budget of Ocean Mode Waters. *Journal of Physical Oceanography*, *48*(9), 2141–2165. https://doi.org/10.1175/JPO-D-17-0219.1

Wenegrat, J. O., Thomas, L. N., Gula, J., & McWilliams, J. C. (2018b). Effects of the Submesoscale on the Potential Vorticity Budget of Ocean Mode Waters. *Journal of Physical Oceanography*, *48*(9), 2141–2165. https://doi.org/10.1175/JPO-D-17-0219.1

Wu, J. (1975). Wind-induced drift currents. *Journal of Fluid Mechanics*, *68*(1), 49–70. https://doi.org/10.1017/S0022112075000687

Wu, Y., Zhai, X., & Wang, Z. (2017). Decadal-Mean Impact of Including Ocean Surface Currents in Bulk Formulas on Surface Air–Sea Fluxes and Ocean General Circulation. *Journal of Climate*, *30*(23), 9511–9525. https://doi.org/10.1175/JCLI-D-17-0001.1

Yu, L. (2007). Global Variations in Oceanic Evaporation (1958–2005): The Role of the Changing Wind Speed. *Journal of Climate*, *20*(21), 5376–5390. https://doi.org/10.1175/2007JCLI1714.1

Zhai, X., & Greatbatch, R. J. (2007). Wind work in a model of the northwest Atlantic Ocean. *Geophysical Research Letters*, *34*(4). https://doi.org/10.1029/2006GL028907

Zhang, D., Cronin, M. F., Wen, C., Xue, Y., Kumar, A., & McClurg, D. (2016). Assessing surface heat fluxes in atmospheric reanalyses with a decade of data from the NOAA Kuroshio Extension Observatory: REANALYSIS HEAT FLUX AND KEO OBSERVATION. *Journal of Geophysical Research: Oceans*, *121*(9), 6874–6890. https://doi.org/10.1002/2016JC011905

BIOGRAPHICAL SKETCH

Xu Chen was born in Yueyang city, Hunan province of China in 1989. He finished high school at The First High School of Yueyang, and moved to Nanjing in 2007 to obtain a Bachelor degree of Science in Atmospheric Science (Atmospheric Physics and Environment) from Nanjing University of Information Science and Technology. After earned the Bachelor's degree in 2011, he went to Florida State University to pursue his graduate degree. He has earned a Master's degree in Meteorology in the Spring of 2014. During the Summer of 2014, he began the Ph.D. program in Physical Oceanography which he later finished in the Fall of 2018.